Interface effects in solid electrolytes for Li-ion batteries

Zur Erlangung des akademischen Grades eines

DOKTORS DER INGENIEURWISSENSCHAFTEN (Dr.-Ing.)

von der KIT-Fakultät für Maschinenbau des

Karlsruher Instituts für Technologie (KIT)

angenommene

DISSERTATION

von

M. Sc. Xianlin Luo

Tag der mündlichen Prüfung: 15.02.2022

Hauptreferent: Prof. Dr. Helmut Ehrenberg

Korreferent: Prof. Dr. Michael J. Hoffmann

Korreferentin: TT-Prof. Dr. Julia Maibach

Declaration

I hereby declare that I wrote the present work independently. All sources and tools used in this work are specified and all citations are labeled as references. This thesis was not presented to an other examination board and it has not been published before.

Karlsruhe, 15.11.2021

Xianlin Luo

Abstract

The current thesis focuses on the study of heterogeneous oxysulfides (100-x)Li_3PS_4-xLi_3PO_4 (10 ≤ x ≤ 40) and multilayer thin-film LiON-Al_2O_3 solid electrolytes (SEs) for Li-ion batteries (LIBs). Particularly, heterostructured bulk-type oxysulfides and multilayer thin-film LiON-Al_2O_3 SEs were synthesized by a two-step mechanical milling and atomic layer deposition (ALD), respectively. Their physicochemical and electrochemical properties were studied by various techniques and the work on SEs is organized in two sections as described below:

(I) Heterogeneous oxysulfides (100-x)Li_3PS_4-xLi_3PO_4 (10 ≤ x ≤ 40) SEs. A series of (100-x)Li_3PS_4-xLi_3PO_4 with glass-ceramic structure were successfully prepared by the introduction of Li_3PO_4 into Li_3PS_4. Meanwhile, oxysulfide units $[PS_3O]^{3-}$, $[PS_2O_2]^{3-}$, and $[PSO_3]^{3-}$ were found in the mixtures by ^{31}P MAS NMR (magic-angle spinning nuclear magnetic resonance spectroscopy). According to impedance spectroscopy, oxysulfides (100-x)Li_3PS_4-xLi_3PO_4 with x = 20 and 15 exhibit higher ionic conductivity (1.6 x 10^{-4} S/cm) than the pure Li_3PS_4 (1.2 x 10^{-4} S/cm) at room temperature (RT). This phenomenon is attributed to the opposite influences of the space charge effect vs. the blocking effect. After stabilization by Li plating and stripping, direct-current (DC) conductivities of Li/80Li_3PS_4-20Li_3PO_4/Li and Li/85Li_3PS_4-15Li_3PO_4/Li increase to 2.4 x 10^{-3} S/cm and 9.5 x 10^{-4} S/cm at RT, respectively. The introduction of Li_3PO_4 into Li_3PS_4 results in superior interface stability between Li and our oxysulfides uncovered by time-resolved impedance spectroscopy and Li plating and striping. Strong side reactions were observed for Li_3PS_4 through a cyclic voltammetry (CV) test of a symmetric Li/Li_3PS_4/Li cell. Moreover, a $LiCoO_2$ cathode has been studied as a proof of concept together with the heterogeneous oxysulfides SEs with x = 20 and x = 15, exhibiting improved capacity and cyclic stability compared with pure Li_3PS_4. The excellent SEs/Li interface stability of these two oxysulfides was again proved in the full cell by their stable resistance after over 60 charge-discharge cycles. Despite its improvements, the $LiCoO_2$ positive electrode still suffers from capacity loss during the first several cycles due to the huge resistance of the interface between SE and $LiCoO_2$.

(II) Multilayer thin-film LiON-Al_2O_3 SEs. A series of flat and pinhole-free multilayer thin-film LiON-Al_2O_3 electrolytes were successfully prepared. The amorphous structure of LiON-Al_2O_3

deposited at 200 °C was proved by grazing incidence X-ray diffraction (GIXRD) and magic-angle spinning nuclear magnetic resonance spectroscopy (MAS NMR). The layer-by-layer structure and composition of thin-film LiON-Al_2O_3 were confirmed using cross-sectional HRTEM (high-resolution transmission electron microspectroscopy) and XPS (X-ray photoelectron spectroscopy) sputter depth profiling, where the LiON layers mainly consist of LiOH, Li_2CO_3, Li-N, and Li_2O and are separated by Al_2O_3 layers. These multilayered heterostructures exhibit an improved ionic conductivity due to the introduction of nitrogen and Al_2O_3, compared with pure 600LiON film, since Al_2O_3 introduces heterointerfaces with accelerated conduction along these interfaces. Remarkably, the overall concentration of Li^+ ions is lower in these heterostructures compared to the pure LiON film, but the overall conductivity is enhanced with the increase of the activation energy. The space charge effect at the heterointerface is deemed to be the mechanism behind this enhancement, and the origin of increased activation energy could be local structural distortions. The combination of 3.2 nm of LiON sublayer and 1 nm Al_2O_3 sublayer shows the highest conductivity (6.2×10^{-4} S/cm at 160 °C) and the lowest activation energy (0.57±0.02 eV) among all the multilayer heterostructures. This work provides a new approach to design heterostructured multilayer thin-film SEs with highly conducting interfaces via ALD for ionic devices.

Zusammenfassung

Diese Arbeit konzentriert sich auf die Untersuchung von heterogenen Oxysulfiden (100-x) Li_3PS_4-xLi_3PO_4 ($10 \leq x \leq 40$) und mehrschichtigen Dünnschicht-LiON-Al_2O_3-Festkörperelektrolyten (SEs) für Lithium-Ionen-Batterien (LIBs). Insbesondere wurden heterostrukturierte Oxysulfide vom Bulk-Typ und mehrschichtige Dünnschicht LiON-Al_2O_3 SEs durch zweistufiges mechanisches Mahlen bzw. Atomlagenabscheidung (ALD) synthetisiert. Ihre physikochemischen und elektrochemischen Eigenschaften wurden mit verschiedenen Techniken untersucht und die Arbeit an SEs ist in zwei Abschnitte unterteilt, wie nachstehend beschrieben:

(I) Heterogene Oxysulfide (100-x)Li_3PS_4-xLi_3PO_4 ($10 \leq x \leq 40$) SEs. Eine Reihe von (100-x)Li_3PS_4-xLi_3PO_4 mit glaskeramischen Eigenschaften wurde erfolgreich durch Beimischung von Li_3PO_4 in Li_3PS_4 hergestellt. Dabei wurden die Oxysulfideinheiten $[PS_3O]^{3-}$, $[PS_2O_2]^{3-}$ und $[PSO_3]^{3-}$ in den Gemischen durch ^{31}P MAS NMR (Magic-Angle-Spinning Kernspinresonanz) nachgewiesen. In der Impedanzspektroskopie zeigen Oxysulfide (100-x)Li_3PS_4-xLi_3PO_4 mit x = 20 und 15 eine höhere Wechselstrom-Ionenleitfähigkeit ($1,6 \times 10^{-4}$ S/cm) als reines Li_3PS_4 ($1,6 \times 10^{-4}$ S/cm) bei Zimmertemperatur (RT). Dieses Phänomen wird auf die gegensätzlichen Einflüsse des Raumladungseffekts gegenüber dem Blockierungseffekt zurückgeführt. Nach der Stabilisierung durch Li-Plating und -Stripping steigen die Gleichstrom-Ionenleitfähigkeiten von Li/80Li_3PS_4-20Li_3PO_4/Li und Li/85Li_3PS_4-15Li_3PO_4/Li bei RT auf $2,4 \times 10^{-3}$ S/cm bzw. $9,5 \times 10^{-4}$ S/cm. Die Einführung von Li_3PO_4 in Li_3PS_4 führt zu einer verbesserten Grenzflächenstabilität zwischen Li und den Oxysulfiden, was mittels zeitaufgelöster Impedanzspektroskopie und Li-Plating und -Stripping festgestellt wurde. Für Li_3PS_4 wurden dagegen durch Cyclovoltammetrie an symmetrischen Zellen Li/Li_3PS_4/Li starke Nebenreaktionen beobachtet. Darüber hinaus wurde eine $LiCoO_2$-Kathode in einer Machbarkeitsstudie zusammen mit den heterogenen Oxysulfid-SEs für x = 20 und x = 15 untersucht, die im Vergleich zu reinem Li_3PS_4 eine verbesserte Kapazität und Zyklen-Stabilität aufweisen. Die ausgezeichnete Stabilität der SEs/Li-Grenzfläche dieser beiden Oxysulfide wurde in der Vollzelle ebenfalls durch ihren stabilen Widerstand nach über 60 Lade-Entlade-Zyklen bewiesen. Trotz ihrer Verbesserungen

leidet die positive $LiCoO_2$-Elektrode in den ersten Zyklen aufgrund des enormen Widerstands der Grenzfläche zwischen SE und $LiCoO_2$ immer noch unter Kapazitätsverlust.

(II) Mehrschichtige Dünnschicht-LiON-Al_2O_3 SEs. Eine Reihe von flachen und defektfreien mehrschichtigen Dünnschicht-LiON-Al_2O_3 wurde erfolgreich hergestellt. Die amorphe Struktur von bei 200 °C abgeschiedenem LiON-Al_2O_3 wurde durch Röntgenbeugung unter streifendem Anfall (GIXRD) und Magic-Angle-Spinning Kernspinresonanzspektroskopie (MAS-NMR) nachgewiesen. Die schichtweise Struktur und Zusammensetzung von dünnschichtigem LiON-Al_2O_3 wurde unter Verwendung von Querschnitt-HRTEM und XPS Tiefenprofilen bestätigt, wobei die LiON-Lagen hauptsächlich aus LiOH, Li_2CO_3, Li-N und Li_2O bestehen und durch Al_2O_3-Lagen getrennt sind. LiON-Al_2O_3-Dünnschichten zeigen aufgrund der Einführung von Stickstoff und Al_2O_3 eine verbesserte Ionenleitfähigkeit im Vergleich zur reinen 600LiON-Dünnschicht, da Al_2O_3 Hetero-Grenzflächen eingebracht werden, wobei die Ionenleitung entlang dieser Grenzflächen beschleunigt ist. Bemerkenswerterweise ist die Gesamtkonzentration an Li^+-Ionen in diesen Heterostrukturen im Vergleich zum reinen LiON-Dünnschicht geringer, aber die Gesamtionenleitfähigkeit wird trotz zunehmender Aktivierungsenergie erhöht. Raumladungseffekte an der Hetero-Grenzfläche werden als der Mechanismus für diese Verbesserung angesehen, wobei lokale strukturelle Unordnung, induziert durch die isolierenden Al_2O_3-Zwischenschichten die Ursache der erhöhten Aktivierungsenergien sein können. Die Kombination von einer 3,2 nm dicken LiON-Zwischenschicht und einer 1 nm dicken Al_2O_3-Zwischenschicht zeigt die höchste Ionenleitfähigkeit (6,2 x 10^{-4} S/cm at 160 °C) und die niedrigste Aktivierungsenergie (0,57±0.02 eV) unter allen eingesetzen mehrschichtigen Heterostrukturen. Diese Arbeit bietet einen neuen Ansatz für das Design heterostrukturierter mehrschichtiger Dünnschicht-Festkörperelektrolyte mit hochionenleitenden Grenzflächen über ALD für ionische Bauteile.

Contents

1 Motivation

The ever-rising global population and energy consumption per capita significantly increase the demands for energy resources (*1*). Currently, limited fossil fuels are still our main energy resources, which results in climate change and environmental pollution (*2*). The development of alternative clean and sustainable energy resources such as solar, biomass, geothermal, water, and wind power is promoted to solve these problems. But these resources are not that reliable due to their nature of immovability and discontinuity. Rechargeable batteries, which can be charged with renewable energy and discharged to provide clean electric energy, are essential energy storage systems to make the best use of renewable energy resources (*3*). Compared to other rechargeable batteries, such as lead-acid, nickel-cadmium, or nickel-metal hybrid batteries, lithium-ion batteries (LIBs) are the most promising candidate owing to their high power density, high energy density, and long cycle life (*4*, *5*).

30 years ago (1991), LIB consisting of a graphite negative electrode, organic electrolyte, and a $LiCoO_2$ positive electrode was first commercialized by Sony Corporation. Since then, LIBs dominate the market of portable electronic devices including cell phones, tablets, laptops, etc., and gradually penetrate other technologies like electric vehicles and stationary energy storage systems (*6–10*). However, today's lithium-ion technology does not yet meet the entire requirements for a perfect energy storage system. The liquid electrolytes (LEs) used in LIBs, which normally consist of Li salts dissolved in organic solvents, cause serious safety problems regarding flammability and possible leakages (*11*, *12*). Furthermore, repeated cycling of LIBs with LEs leads to the formation and growth of dendrites, especially when Li metal is applied as a negative electrode. Dendrites can short-circuit the cell and consequently result in a thermal runaway of the cell (*13*). All-solid-state batteries (ASSBs) using solid electrolytes (SEs) are proposed to address the safety issues of LIBs. Thanks to the intrinsic solid character of the SEs, the formation of dendrites could be suppressed, which enables the safe application of Li metal as the negative electrode and thus improves the energy density owing to its high theoretical capacity of 3860 mAh/g (*14*). Moreover, SEs can offer a wide electrochemical stability window and high thermal stability, and enable a simple battery design (*15*). The associated weight and volume reduction of the electrolyte enables a further increase in energy

density (*16*–*18*). Great attention has been paid to sulfide SEs because of their high conductivity, which is comparable to or greater than those of most LEs (*19*). Furthermore, sulfide SEs can be deformed simply by cold-pressing of electrolyte powders, which is beneficial for the fabrication of ASSBS.

However, conventional ASSBs with bulk-type SEs cannot meet the requirements of increasingly smaller microelectronic devices such as implantable devices and wireless sensors, in the so-called internet of things (IoT) era (*20*). To power these miniaturized microelectronic devices, a smaller energy storage system with high volumetric energy density is necessary. Two-dimensional (2D) thin-film batteries (TFBs), composed of positive electrode film, negative electrode film, and SE film instead of bulk-type SE, are the potential candidate. To maximize the areal energy density of TFBs, the thicknesses of thin-film electrodes are increased. But this would give rise to structural instability like film delamination and the decrease of the areal power density due to larger Li^+ transport distances associated with thicker electrodes. Thanks to the use of the third dimension, height, three-dimensional (3D) batteries are considered to be a more effective strategy. They provide higher energy density owing to the efficient use of the volumetric space, simultaneously delivering a better power density, which results from the short Li^+ diffusion paths (*21*–*24*). Since 3D positive and negative electrodes have been already fabricated, the deposition of appropriate 3D thin-film SEs is a key challenge in fabricating 3D batteries (*25*). Atomic layer deposition (ALD), based on sequential and self-limiting surface reactions, is ideal for the deposition of pinhole-free, conformal, and homogeneous films on complex 3D architectures in 3D batteries (*26*, *27*). Furthermore, the ALD is the only deposition technique that enables the precise control of the composition and thickness of the film at the atomic scale, which is crucial to design a preferred thin-film SE (*28*, *29*).

In some cases, it is reported that the heterointerfaces between ion conductor and insulator enhance the ionic conductivity of both bulk-type and thin-film electrolytes owing to the space charge effect and strains on the heterointerfaces (*30*–*36*). In this work, both heterogeneous composites and ALD thin films were synthesized to investigate this enhancement of ionic conductivity in both systems.

2 Fundamentals

In this chapter, the structures and principles of a common organic liquid LIB and various SSBs are outlined in sections 2.1 and 2.2, respectively. Some important electrochemical parameters and concepts for batteries are then explained in section 2.3. Section 2.4 gives a brief overview of inorganic SEs including bulk-type and thin-film type SEs. In the last section of this chapter, the aim of the thesis is presented.

2.1 Lithium-ion batteries

Generally, a conventional lithium-ion battery (LIB) contains a positive electrode and a negative electrode immersed in a liquid electrolyte separated by a polymer membrane (separator). The terms “anode” and “cathode” refer to “negative electrode” and “positive electrode”, respectively, during the discharge process while the reverse is the case during the charge process. In this thesis, positive and negative electrodes will be used to avoid confusion. The electrolyte should be highly ionic conductive to transport Li^+ ions between the two electrodes, while the separator serves as an electronic insulator to prevent the short circuit. Figure 2.1 shows the most widely commercialized LIB system that uses graphite as the anode and $LiCoO_2$ as the cathode. During the charging process, Li^+ ions are extracted from the $LiCoO_2$ cathode (Equation 2.1) and intercalated into the graphite anode (Equation 2.2) through the electrolyte driven by an external voltage (Equation 2.3). In this way, the electric energy is converted to chemical energy stored in the battery by the oxidation of the cathode the reduction of the anode. During the discharging process, Li^+ ions and electrons move reversely (Equation 2.4, Equation 2.5, and Equation 2.6). The chemical energy is thus transformed back to electric energy to power electronic devices. The principle of such LIB can be illustrated by the following electrochemical reactions:

Charge: $LiCoO_2 \rightarrow Li_{1-x}CoO_2 + xLi^+ + xe^-$ Equation 2.1

$C + xLi^+ + xe^- \rightarrow Li_xC$ Equation 2.2

Total reaction: $LiCoO_2 + C \rightarrow Li_{1-x}CoO_2 + Li_xC$ Equation 2.3

Discharge: $Li_{1-x}CoO_2 + xLi^+ + xe^- \rightarrow LiCoO_2$ Equation 2.4

$Li_xC \rightarrow C + xLi^+ + xe^-$ Equation 2.5

Total reaction: $Li_{1-x}CoO_2 + Li_xC \rightarrow LiCoO_2 + C$ Equation 2.6

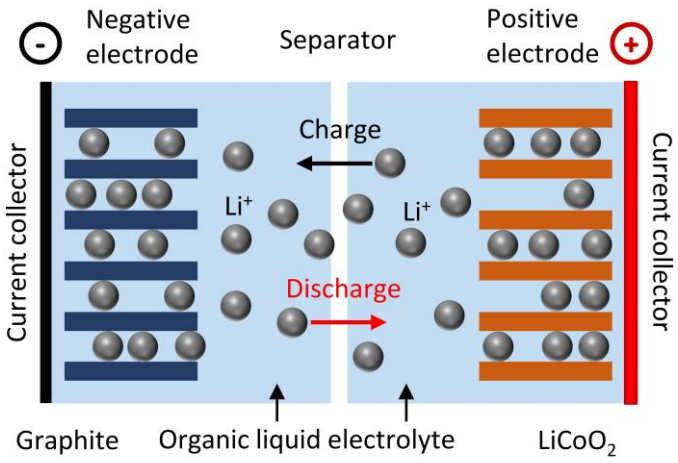

Figure 2.1: Scheme of the LIBs using liquid electrolytes.

2.2 All-solid-state batteries

In an ASSB, not only the positive and negative electrodes are solid but also the electrolyte, which works as both liquid electrolyte and separator. The positive electrode and the negative electrode are attached to both sides of the SE. Since the contact between solid and solid is not comparable with that of solid and liquid, the solid interface between electrode and SE plays a key role in the performance of an ASSB (*37*). The structure of ASSBs is simpler than LIBs and can therefore eliminate the restrictions of packaging and safety. ASSBs share a similar working principle with conventional LIBs: Li^+ ions move back and forth between the positive electrode and the negative electrode via the SE during charge and discharge processes, while electrons transfer reversibly via the external circuit.

A schematic diagram of three different ASSBs including bulk ASSBs, two-dimensional thin-film batteries (TFBs), and 3D batteries are presented in Figure 2.2. The positive electrode of a bulk ASSB consists of a composite of active material and SE (and conductive additives) and the negative electrode can be made up of a composite or lithium metal (*38*). ASSBs are normally constructed by hot or cold pressing, while TFBs adopting 2D planar design are prepared by stacking dense electrodes and electrolyte films via various deposition techniques, such as chemical vapor deposition (CVD), electrostatic coating, or pulsed laser deposition (PLD) (*25*). Unlike the composite electrodes in bulk ASSBs, only active materials are used in thin-film electrodes. The thickness of thin-film electrodes is limited to a few microns because of kinetic and structural problems brought by thickened electrodes. TFBs fabricated by vapor deposition

have been commercialized, however, they still suffer from their restriction of limited areal specific capacity (*39*). In a 3D battery, electrode and electrolyte thin films are deposited in a 3D architecture. These conformal 3D layers significantly increase the effective surface area and consequently improve the energy and power densities. Although 3D batteries share a similar local battery structure with TFBs, the demand for an appropriate electrolyte film with complex contours still stands in the way of their commercialization.

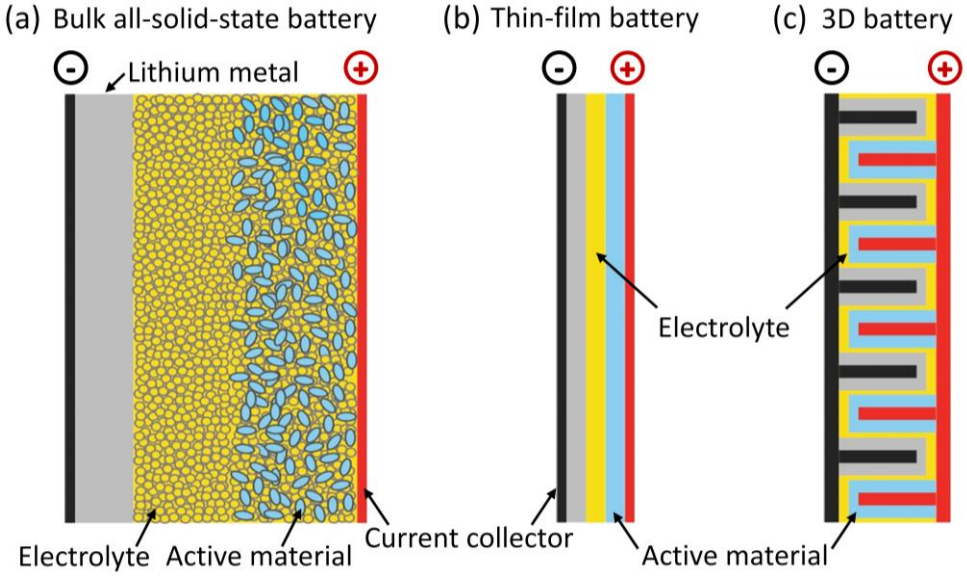

Figure 2.2: Schemes of three typical ASSBs configurations: (a) bulk all-solid-state battery, (b) thin-film battery, and (c) 3D battery.

2.3 Basic battery parameters

1) Cell voltage

The cell voltage E (V) corresponds to the potential difference of the positive electrode and the negative electrode in units of volts. If the electrical work or free energy ΔG (kJ/mol) is known, the cell voltage can be calculated by the following thermodynamic function:

$$\Delta G = -zFE \text{ or } \Delta G^{\ominus} = -zFE^{\ominus} \qquad \text{Equation 2.7}$$

where z is the number of electrons transferred in the cell reaction or half-reaction, F (96485 C/mol) is Faraday's constant, $\Delta G^{\ominus}$ (kJ/mol) is the standard free energy, and $E^{\ominus}$ (V) is the standard electromotive force. ΔG is given by Nernst equation:

$$\Delta G = \Delta G^{\ominus} + RT \cdot \ln(K) \qquad \text{Equation 2.8}$$

here R (8.314 J/mol·K) is the ideal gas constant, T is the absolute temperature in Kelvin and K is the thermodynamic equilibrium constant of the electrochemical reaction given by:

$$K = \ln(a_{ox}/a_{re}) \quad \text{Equation 2.9}$$

where a_{ox} and a_{re} are the activities of oxidized and reduced species, respectively. Then the theoretical cell voltage can be calculated by combining Equation 2.7 and 2.8 in the Nernst equation:

$$E = E^{\ominus} + (RT/zF)\ln(K) \quad \text{Equation 2.10}$$

2) Capacity and specific capacity

The capacity Q describes the amount of electric charge that a battery can deliver at a rated voltage in units of Ah or mAh. The specific capacity C refers to the capacity per unit mass, which is expressed in mAh/g. The theoretical specific capacity C_{th} is given by:

$$C_{th} = NF/3600M \quad \text{Equation 2.11}$$

where N is the number of moles of charge carrier and M (g/mol) is the molecular weight of the active material used in the electrode.

3) C-rate

A C-rate is used to measure the rate of discharge of a battery relative to its maximum capacity. It is defined as the capacity divided by the discharge time. For instance, a 1C rate means that the battery is fully discharged within 1h, while 10C refers to fully discharging within 1/10 h.

4) Coulombic efficiency

The Coulombic efficiency η_c is defined as the ratio of the total charge extracted from the battery $Q_{discharge}$ to the total charge injected into the battery Q_{charge} over a full charge/discharge cycle.

$$\eta_c = Q_{discharge}/Q_{charge} \quad \text{Equation 2.12}$$

5) Energy, specific energy, and energy density

The energy ε (Wh) of a battery corresponds to the product of the cell capacity Q and the average cell voltage E_{av}:

$$\varepsilon = QE_{av} \quad \text{Equation 2.13}$$

The energy values per unit mass and per unit volume are expressed as the specific energy (Wh/kg) and the energy density (Wh/L), respectively.

6) Ionic conductivity

The ionic conductivity σ (S/cm) is used to describe the tendency of material towards ionic conduction, which arises from the movement of positive (or negative) charged ions under an external electric field. The ionic conductivity can be defined by the following equation:

$$\sigma = nq\mu \qquad \text{Equation 2.14}$$

where n (cm^{-3}) is the number of ions per unit volume, q (C) is the carrier charge, and μ ($m^2V^{-1}s^{-1}$) is the mobility, the average velocity of an ion due to an applied electric field of unit strength.

7) The Arrhenius model

The Arrhenius model describes the relationship between the temperature and the rate of chemical or physical reactions via the Arrhenius equation below:

$$k = k_0 \exp(E_a/RT) \qquad \text{Equation 2.15}$$

where k is the kinetic reaction rate, k_0 is the rate constant, E_a (eV or J/mol) is the activation energy defined as the minimum amount of energy that is required to result in a chemical reaction or physical transport, R (8.314 J/mol·K) is the ideal gas constant, and T (K) is the absolute temperature.

The ionic conduction is also considered to be an activated process, which has contributions from both ionic mobility and defect formation. Therefore, the temperature dependence of ionic conductivity is given by:

$$\sigma = (\sigma_0/T) \exp(E_a/RT) \qquad \text{Equation 2.16}$$

where σ_0 is a constant. Converting this relationship to natural logarithm form, the following equation is obtained:

$$\ln(\sigma T) = \ln\sigma_0 - E_a/RT \qquad \text{Equation 2.17}$$

A graph of ln(σT) against 1/T is called an Arrhenius plot, which theoretically should be a straight line for thermally activated conduction. The activation energy can be then calculated based on the slope of this line.

2.4 Inorganic solid electrolytes

Solid electrolytes (SEs) are classified into inorganic and organic electrolytes. Inorganic SEs with better thermal stability and mechanical stability have been widely investigated. This short

overview of SEs will focus on inorganic SEs with regard to this thesis concerning both bulk and thin-film.

2.4.1 Bulk solid electrolytes

Inorganic bulk solid electrolytes mainly comprise sulfides and oxides, which are remarkable due to their high thermal stability and ionic conductivity. Oxide SEs with different structures such as garnet, perovskite, lithium superionic conductor (LISICON), and sodium superionic conductors (NASICON) have been intensively studied. Oxide SEs have high conductivity (10^{-6}-10^{-3} S/cm at room temperature (RT)) and high stability at high voltage as well as in the air (*40*). Sulfide SEs systems including binary systems and ternary systems have drawn more and more attention recently due to their extremely high ionic conductivity (10^{-4}-10^{-2} S/cm at RT) and cold deformable nature. Compared with oxide SEs, sulfide SEs have a weaker attraction between the sulfide framework and the Li^+ ions because of the higher polarizability of sulfide ions. Therefore, the mobility of Li^+ ions in sulfide SEs is higher than in oxide SEs (*17*, *41*).

1) Oxide solid electrolytes

Garnet-type SEs share a chemical formula of $AB(CO_4)_3$ where A (Ca, Mg, La, Y, or rare earth metals), B (Al, Fe, Ga, Ge, Mn, Ni, V), and C (Si, Ge, or Al) are located in eight, six, and four oxygen-coordinated cation sites, respectively. They are one of the most promising candidates for ASSBs owing to their high conductivity and exceptional stability against Li metal (*42*, *43*). The first garnet-type SE $Li_5La_3M_2O_{12}$ (M = Nb and Ta) was found by Thangadurai et al., where $Li_5La_3Ta_2O_{12}$ showed an ionic conductivity of $3.4x10^{-6}$ S/cm at RT (*44*). By partial substitution of La with Ba, the ionic conductivity of $Li_6BaLa_2Ta_2O_{12}$ was increased to $4x10^{-5}$ S/cm at RT (*45*). In 2007, Murugan et al. reported cubic structured $Li_7La_3Zr_2O_{12}$ (LLZO) with an ionic conductivity of $3x10^{-4}$ S/cm at RT, which is higher than the tetragonal LLZO due to the different degree of Li-vacancy order on the tetrahedral and octahedral sites (*46*, *47*). The conductivity of cubic LLZO could be further enhanced by doping with other ions such as Y^{3+}, Al^{3+}, Ta^{5+}, Nb^{5+}, Si^{4+}, Ga^{3+}, and Te^{6+} (*48*–*54*). $La_3Zr_{1.75}Te_{0.25}O_{12}$ was obtained by partial replacement of Zr^{4+} with Te^{6+}, which reaches a superior conductivity of 1.02×10^{-3} S/cm at RT (*53*). Lu et al. achieved an even higher ionic conductivity of 1.28×10^{-3} S/cm at RT with $Li_{6.25}Ga_{0.25}La_3Zr_2O_{12}$ (*54*).

The Perovskite structure family exhibits a general formula of ABO_3 with alkaline ions (Li^+, Na^+, K^+) or rare-earth ions (La^{2+}, Sr^{2+}, Ca^{2+}, Ba^{2+}) in the A sites and transition metal ions (Ti^{4+}, Al^{3+}, Zr^{4+}) in the B sites. The A ions and B ions are 12-fold and 6-fold coordinated with oxygen ions, respectively. $Li_{3x}La_{2/3-x}TiO_3$ (LLTO) is one of the most representative perovskite-type SEs, in which A sites are occupied by Li and La. It is reported that the conductivity of LLTO depends on the concentration of Li and vacancies in A sites (*55*). The LLTO synthesized by Inaguma et al. exhibited a conductivity exceeding 10^{-3} S/cm at RT (*56*). However, Ti^{4+} in LLTO is easily reduced to Ti^{3+} by Li metal or intercalated electrodes with a cathodic potential above 2.8 V (*57*). Furthermore, the ionic conductivity of LLTO is limited by its high grain boundary resistance (*58*).

Li^+ ion conductive oxides with a crystalline structure similar to that of γ-Li_3PO_4 are called LISICON in which all cations are tetrahedrally coordinated. The composition of $Li_{3+x}(P_{1-x}M_x)O_4$ within a given LISICON structure obtained by partially substituting P^{5+} with tetravalent ions such as Si^{4+}, Ge^{4+} can improve the ionic conductivity (*59–61*). Ivanov-Shitz and Kireev synthesized the single-crystal $Li_{3.34}P_{0.66}Ge_{0.34}O_4$ with a conductivity of 3.7×10^{-2} S/cm at 400 °C (*62*). Recently, Zhao et al. reported the co-doped $Li_{3.53}(Ge_{0.75}P_{0.25})_{0.7}V_{0.3}O_4$ showing an ionic conductivity of 5.1×10^{-5} S/cm at RT (*63*). LISICON SEs show high stability even in moist air, however, they have low ionic conductivity at RT (10^{-5} S/cm) and low stability against lithium metal.

NASICON with the general structure of $AB_2(PO_4)_3$, where the A site is occupied by alkali ions (Li^+, Na^+, K^+) and the B site is occupied by tetra-valent ions (Ge^{4+}, Ti^{4+}, Zr^{4+}), was early reported by J. Goodenough and H. Hong et al. based on their work on $Na_{1+x}Zr_2P_{3-x}Si_xO_{12}$ in 1976 (*64*). The 3D framework of NASICON structures consists of corner-sharing BO_6 octahedra and PO_4 tetrahedra. Li-containing NASICON-type SEs are obtained by replacing Na^+ with Li^+ in the A sites and the high Li^+ ionic conductivity can be achieved only when the size of interconnected channels in the framework matches the Li^+ ion size (*65*). It has been widely reported that the conductivity of $LiTi_2(PO_4)_3$ and $LiGe_2(PO_4)_3$ can be significantly improved by Al substitution, named $Li_{1+x}Al_xTi_{2-x}(PO_4)_3$ (LATP) and $Li_{1+x}Al_xGe_{2-x}(PO_4)_3$ (LAGP), respectively (*66–69*). $Li_{1.4}Al_{0.4}Ti_{1.6}(PO_4)_3$ with a very high conductivity of 1.12×10^{-3} S/cm at RT was prepared by Xu et al. (*70*). However, LATP suffers from the same Ti^{4+} reduction issue as LLTO, which is rather

challenging for its application. Cr-doped LAGP $Li_{1.5}Al_{0.4}Cr_{0.1}Ge_{1.5}(PO_4)_3$ shows the highest reported ionic conductivity of 6.65×10^{-3} S/cm at RT to date among NASICON-type SEs (*71*). Ge^{4+} is more stable against Li metal than Ti^{4+}, but the high cost of Ge restrict the application field of LAGP (*72*).

2) Sulfide solid electrolytes

Li_2S-P_2S_5 binary system lithium-ion conductors have been widely studied due to their low cost, high ionic conductivities, and wide electrochemical windows vs. Li/Li^+. Among these binary sulfides, $75Li_2S$-$25P_2S_5$ (Li_3PS_4) with good compatibility with lithium metal and $30Li_2S$-$70P_2S_5$ ($Li_7P_3S_{11}$) with high RT conductivity over 10^{-3} S/cm gained more and more attention. Tatsumisago successfully synthesized amorphous Li_3PS_4 by mechanical ball milling, which exhibited a conductivity of 2×10^{-4} S/cm at RT (*73*). Crystalline Li_3PS_4 has three different phases: the low-temperature γ phase, the medium-temperature β phase, and the high-temperature α phase. γ-Li_3PS_4 has the lowest ionic conductivity of $3x10^{-7}$ S/cm at RT while β-Li_3PS_4 is the highest ionic conductive phase (about 10^{-4} S/cm) due to the different arrangements of PS_4^{3-} tetrahedrons in crystal Li_3PS_4 (*74*, *75*). The glass-ceramic $Li_7P_3S_{11}$ prepared by melting, quenching and then hot pressing exhibits an extremely high RT conductivity of 1.7×10^{-2} S/cm owing to its low grain boundary resistance (*76*). Other binary systems such as Li_2S-B_2S_3 and Li_2S-SiS_2 exhibit ionic conductivities of around 10^{-4} S/cm at RT, and Li_2S-GeS_2 has lower ionic conductivity in the range of 10^{-5}-10^{-7} S/cm at RT (*77*–*79*). Their ionic conductivity could be improved by increasing the concentration or mobility of Li^+ via doping of lithium salts or lithium halides. The conductivity of the Li_2S–SiS_2 binary system was increased to higher than 10^{-3} S/cm at RT by adding Li_xMO_y (M = Si, Ge, P) (*80*). With the addition of LiX (X = Cl, Br, I), the ionic conductivities of both Li_2S-B_2S_3 and Li_2S-SiS_2 can be significantly improved (*81*–*83*).

Similarly, in order to improve the ionic conduction in the Li_2S-P_2S_5 binary system, a third component such as a sulfide (GeS_2, SiS_2, SnS_2 Al_2S_3, P_2S_3, MoS_2), a lithium halide (LiF, LiCl, LiBr, LiI) or an oxide (P_2O_5, Li_2O) is added into the binary sulfide SEs forming ternary system sulfide SEs (*84*–*91*). In 2011, a lithium superionic conductor $Li_{10}GeP_2S_{12}$ (LGPS) was prepared by doping with GeS_2, which provides an extremely high conductivity of $1.2x10^{-2}$ S/cm at RT (*84*). To reduce the cost brought by Ge, SiS_2 and SnS_2 were used for doping resulting in $Li_{10}SiP_2S_{12}$ ($2.3x10^{-3}$ S/cm at RT) and $Li_{10}SnP_2S_{12}$ ($4x10^{-3}$ S/cm at RT) compounds (*85*, *86*). It is believed

that the enhancement of the conductivity arises from the lithium vacancies caused by the aliovalent substitution (*92*). The partial replacement of S^{2-} by halogen ions in the Li_2S-P_2S_5 binary system, namely, Li_6PS_5X (X = Cl, Br, and I), could enhance the ionic conductivity because of the highly disordered cation arrangement (*93*, *94*). It is reported that the conductivity of the crystalline Li_6PS_5Cl is more than 10^{-3} S/cm at RT (*95*, *96*). The main drawback of the sulfide SEs is their poor chemical stability against moisture in the air. They easily react with steam in the air and consequently produce toxic H_2S and destroy the structure (*97*). To stabilize the Li_2S-P_2S_5 binary system, various oxide dopings such as P_2O_5, Li_2O, Fe_2O_3, ZnO, Bi_2O_3, Li_3PO_4 are introduced into the system (*88*, *91*, *98*, *99*).

2.4.2 Thin-film solid electrolytes

Since bulk-type SEs can not meet the demand on ever-reduced package size, a lot of thin-film SEs for TFBs in the conductivity range of 10^{-9}-10^{-4} S/cm have been developed by various deposition techniques such as pulsed laser deposition (PLD), radiofrequency (RF) sputtering, atomic layer deposition (ALD), sol-gel, etc. These thin films are divided into 6 groups here: LiPON, NASICON, perovskite, garnet, other oxides, sulfides.

Owing to its high conductivity of 10^{-6} S/cm at RT and a wide electrochemical window of 5.5 V versus lithium, amorphous lithium phosphorous oxynitride (LiPON) thin films have been commercialized in many TFBs (*39*). Various techniques such as PLD, RF sputtering, and ALD are utilized for the deposition of LiPON thin films (*100*–*105*). In LiPON, double or triple coordinated nitrogen atoms replace oxygen atoms that are bonded to phosphorous. The length of links between the phosphate chains is thus decreased and consequently enhances Li^+ ions transport (*106*, *107*). A RT conductivity close to 10^{-3} S/cm is achieved by substrate biasing on the LiPON films deposited via RF sputtering (*108*). Recently, 3D conformal LiPON thin films via ALD were prepared for potential application in 3D batteries. Kozen et al. synthesized LiPON ALD films with different nitrogen concentrations by changing the N_2 plasma pulse duration (*103*). In their report, the maximum RT ionic conductivity of approximately 5 x 10^{-7} S/cm was reached in the film with the highest N concentration of 17 atomic %. Nisula et al.reported LiPON film with RT conductivity of 6.6 × 10^{-7} S/cm via ALD using two precursors instead of three (*104*).

LAGP and LATP are typical NASICON bulk SEs with high ionic conductivity as mentioned in 2.4.1. RF sputtering is one of the most common techniques to deposit their thin-film formats. LAGP thin film with a conductivity of 1.29×10^{-6} S/cm was prepared via RF sputtering at 200 °C by Sun et al. (*109*). Chen et al. reported a high ionic conductivity of 2.46×10^{-5} S/cm for LATP films using RF sputtering deposited at 300 °C (*110*). They indicated that the increased substrate temperature can enhance Li^+ transport due to the formation of a denser film. Similar to their bulk format, LAGP suffers from the high cost of Ga, while LATP is limited due to the reaction between Ti^{4+} and Li metal leading to the formation of a highly resistive interface.

Perovskite-type LLTO thin films have been extensively studied due to the high conductivity of bulk-type LLTO. Ohta et al. grew single-crystalline LLTO film on (001) $SrTiO_3$ by PLD, which showed an ionic conductivity of 2.5×10^{-2} S/cm at 190 °C and 1.5×10^{-4} S/cm at RT by extrapolation with respect to a constant activation energy of 0.37 eV (*111*). Ahn et al. prepared amorphous LLTO films by PLD with RT ionic conductivities of 1.1×10^{-5} S/cm for 400 nm film and 2.0×10^{-5} S/cm for 360 nm film (*112*, *113*). A very impressive ionic conductivity of 1×10^{-3} S/cm of PLD-deposited amorphous LLTO thin films was reported by Furusawa et al., which may originate from both superior electronic and ionic conductivity (*114*). ALD was also used to grow LLTO thin films as reported by Aaltonen et al. (*115*). Unfortunately, the value of ionic conductivity is not presented in their work.

LLZO is one of the most important bulk garnet-type SEs with high ionic conductivity. With this in mind, LLZO thin films have been widely studied and successfully synthesized by PLD, RF sputtering, sol-gel, and CVD (*116*–*119*). Park et al. deposited crystalline LLZO thin films at 600 °C by PLD, which exhibited an ionic conductivity of 1.61×10^{-6} S/cm at RT (*120*). Al- and Ta-doped LLZO thin films generated by PLD were also investigated to improve the ionic conduction performance, which shows RT conductivities of 1×10^{-5} S/cm and 4.4×10^{-6} S/cm by extrapolation, respectively (*121*, *122*). Lobe et al. grew cubic Al- and Ta-doped LLZO films via RF sputtering at 700 °C, which had an impressive conductivity of 1.2×10^{-4} S/cm (*123*).

In addition to the oxides mentioned above, some other oxide films have been also extensively explored. By doping nitrogen via N_2 plasma, amorphous nitrogen-incorporated lithium silicophosphate (LiSiPON) thin films were fabricated by RF sputtering, which show an RT

conductivity above 1×10^{-5} S/cm and high stability against lithium metal (*124–126*). Varying non-conventional oxide films such as Li_xAl_yO, $Li_xAl_ySi_yO$, Li_xSi_yO, Li_xNb_yO, Li_3PO_4, Li_xTa_yO, Li_3BO_3-Li_2CO_3 via ALD have been investigated as thin-film electrolytes in 3D batteries in the past decade (*127–133*). Among these ALD films, Li_3BO_3-Li_2CO_3 with an ionic conductivity of 2.2×10^{-6} S/cm at RT was the highest reported value for ALD thin-film electrolytes (*133*).

Motivated by high conductivity and high electrochemical stability, sulfidic thin films have been investigated as SEs in TFBs. Cao et al. synthesized Li_xAl_yS thin films by ALD providing an extrapolated RT conductivity of 2.5×10^{-7} S/cm, which served as a protecting coating on the lithium metal anode (*134*). Ohta et al. demonstrated a high RT conductivity of 1.7×10^{-4} S/cm of LGPS films produced by PLD, which was about an order of magnitude lower than the bulk conductivity of the target (*135*). It is reported that PLD-deposited amorphous Li_3PS_4 films using Li_2S-excess target ($Li_{3.42}PS_{4.21}$) exhibited a conductivity of 5.3×10^{-4} S/cm at RT (*136*). Seo and Martin reported nLi_2S-GeS_2 (n = 1-4) amorphous thin films via RF sputtering, in which the composition of Li_6GeS_5 revealed the highest RT conductivity exceeding 1×10^{-3} S/cm (*137*).

2.5 Aim and objectives of this thesis

Recently, inorganic SEs gained more and more attention in both bulk and thin-film formats due to their high safety profile and better mechanical properties than those of liquid electrolytes. Heterostructures are a promising way to enhance the ionic conductivity of an SE owing to their high concentration of interfaces. The aim of this thesis is basically to explore heterostructured SEs in both bulk-type and thin-film systems.

1) Bulk-type solid electrolyte: (100-x)Li_3PS_4-xLi_3PO_4

A two-step mechanical milling will be used to prepare the raw heterogeneous composites of (100-x)Li_3PS_4-xLi_3PO_4 with a molar fraction of Li_3PO_4 in the range of 0-40 mol %. The structural evolution of the heterogeneous oxysulfides (100-x)Li_3PS_4-xLi_3PO_4 with various compositions will be then investigated. The desired compositions will be examined using X-ray photoelectron spectroscopy (XPS). To explore the enhancement brought by heterogeneous doping of Li_3PO_4, the ionic conductivity and electrochemical stability of these heterogeneous composites in Li symmetric cells will be studied by various electrochemical techniques. Li-

In/(100-x)Li_3PS_4-xLi_3PO_4/$LiCoO_2$ cells with commercial electrode materials will be assembled to probe their ability to serve as SEEs in a full cell.

2) Thin-film solid electrolyte: LiON-Al_2O_3

Novel heterostructured LiON-Al_2O_3 thin films with symmetric varied sublayer thicknesses will be deposited using atomic layer deposition (ALD). Exemplarily ALD films will be chosen to conduct typical characterizations. As an important property for thin-film SEs, the surface morphology of the heterogeneous films will be characterized at first. Various characterization techniques will be employed to probe the layer-by-layer structure of these multilayered films. In order to obtain in-depth chemical information, both qualitative and quantitative analyses will be carried out by XPS and ToF-SIMS sputter depth profiles. In-plane conductivity of all multilayered thin films and pure LiON film will be tested by impedance spectroscopy to explore the influence of heterostructure and sublayer thickness on the ALD thin films.

3 Characterization Method

This chapter introduces various methods that are used to characterize the bulk-type and thin-film SEs in this work.

3.1 X-ray photoelectron spectroscopy

X-ray photoelectron spectroscopy (XPS) is one of the most commonly used surface-sensitive techniques to assess the chemical and electronic state of the elements (except for hydrogen and helium) within the topmost surfaces. It is based on the photoelectric effect, namely, when the light beam irradiates a material, photoelectrons are emitted with excess kinetic energy if the absorbed energy of light quanta (photon) is larger than the binding energy or the ionization potential of electrons. In the case of XPS measurements, core and valence electrons of the surface atoms are emitted by illumination of an X-ray source as illustrated in Figure 3.1. The emitted photoelectrons are then measured by the spectrometer. When the sample and the spectrometer have good electric contact, they will share the same Fermi energy E_F. With this in mind, the relationship between kinetic energy E_k and binding energy E_b of the photoelectron could be described by:

$$E_k = h\nu - E_b - \phi_{sp} \qquad \text{Equation 3.1}$$

where E_k is the measured kinetic energy (eV) in the spectrometer, hν is the energy of the X-ray source (h (6.63×10^{-34} m^2kg/s): the Planck constant, ν (Hz): the frequency of the photon), E_b is the binding energy (eV) with respect to the Fermi level, and ϕ_{sp} is the work function of the spectrometer, which can be determined experimentally. When the sample is insulating, there will be a local charge build-up resulting from the loss of electrons by the photoelectronic effect. This build-up of electrons raises the Fermi level of the spectrometer relative to the sample. An energy reference (e.g. to adventitious carbon) is required to compensate for the energy shift. It is worth noting that the calculated binding energy E_b based on Equation 2.9 is not a quantity for a single photoelectron, but the energy difference between the initial state with N electrons and the final state with N-1 electrons. This energy difference mainly arises from the chemical shift induced by the chemical environment and the binding energy determined by the electron configuration. Hence, based on the measurement of the number

of photoelectrons and the corresponding binding energy, XPS is able to perform elemental identification, chemical environment analysis, and quantitative calculation.

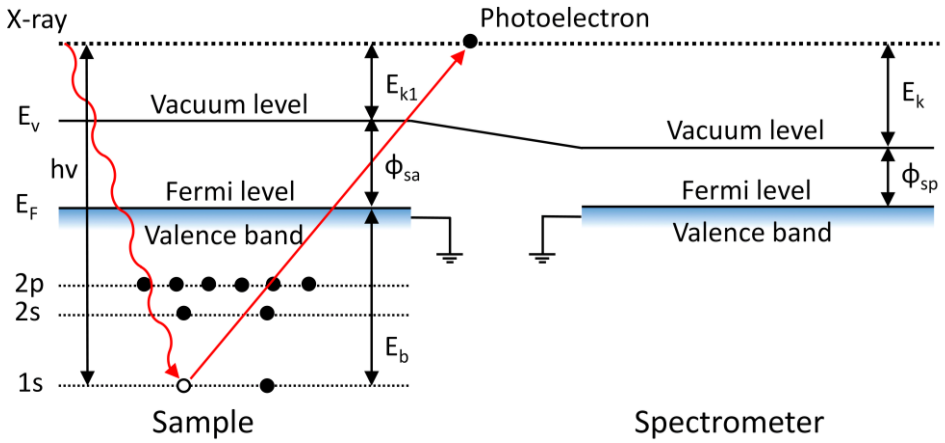

Figure 3.1: Scheme of the photoemission process involved in XPS for a conducting sample. ϕ_{sp} is the work function of the sample and E_{k1} is the kinetic energy of the emitted photoelectrons.

Soft X-ray sources used in XPS can penetrate several micrometers into the sample, but only the photoelectrons within less than 10 nm of the surface can be detected by the spectrometer. The reason is, that the photoelectrons excited in a deep region in the sample lose their energies due to scattering during their penetration to the surface. The escaped photoelectron intensity I_d for an emitted photoelectron intensity I_0 at a depth d below the surface could be calculated according to the Lambert-Beer law:

$$I_d = I_0 \exp(-d/\lambda) \qquad \text{Equation 3.2}$$

where λ refers to the photoelectron inelastic mean free path (IMFP), which means the average distance of an electron between two inelastic collisions. The value of IMFP depends on both the energy of the electron and the material properties. Sampling depth (around 3λ) is defined as the depth from which 95 % of all photoelectrons are able to escape from the surface. Most IMFP values are in the range of 0.5-3.5 nm. As a result, the sampling depth for XPS is in the range of 1.5-10 nm (*138*).

In a typical XPS measurement, the take-off angle between the sample surface and the detection center is commonly fixed to 90°, which provides the deepest chemical information (3λ) of the sample, as presented in Figure 3.2 (a). Additionally, for an angle-resolved XPS (ARXPS) measurement, the sampling depth is decreased to 3λsinφ when decreasing the take-off angle to φ by tilting the sample, as illustrated in Figure 3.2 (b). Compared with XPS, ARXPS

is a more surface-sensitive technique, and it provides non-destructive in-depth information by probing the sample at different take-off angles.

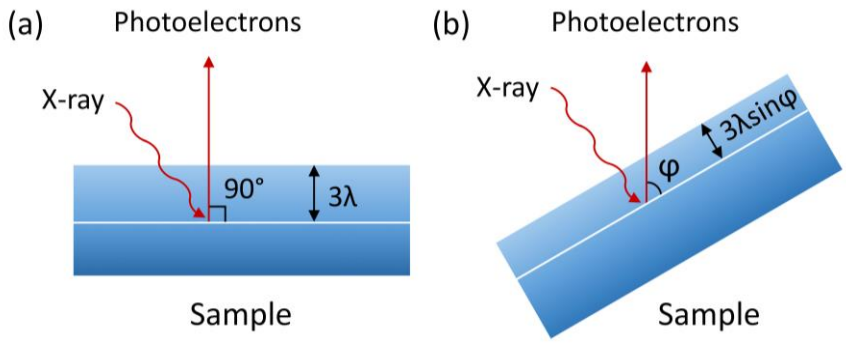

Figure 3.2: Scheme of angle-resolved XPS (ARXPS) at the maximum take-off angle of 90° (a) and decreased take-off angle of φ (b).

Figure 3.3 shows the internal geometry of an XPS instrument that is used in this work (Thermo Fisher Scientific K-Alpha and K-Alpha$^+$). The sample is placed in the ultra-high vacuum (UHV) chamber with a pressure lower than 10^{-8} mbar to minimize the inelastic scattering of photoelectrons with gas molecules and avoid sample contamination by gas absorption of the sample surface. Two cameras, two lamps, and a mirror are then used to identify the position and height of the sample for the XPS measurement. Electrons from the electron source are accelerated by an external voltage to the Al target to create the characteristic X-rays Al K_α (1486.6 eV). A monochromator is then utilized to narrow the band of the wavelength of Al K_α and to provide a spot size between 30-400 µm. The local charge build-up during the measurement can be compensated by a flood gun, which is a dual-beam source consisting of a focused low energy electron beam and the large area ion-flux. Some of the emitted photoelectrons are collected by a 180° hemispherical sector analyzer (HSA) with an acceptance angle of ± 30° and then the photoelectrons with a fixed pass energy are detected by a channel plate detector consisting of 128 channels. To obtain a spectrum over a range of binding energy, it is necessary to scan the voltages in the HAS. An ion gun is used to remove surface material for cleaning or depth profiling. Alternative raster-scanned etching and XPS measurement at the center of the etched area can give in-depth information of the sample, i.e. XPS sputter depth profiling. The most commonly used ion beam are Ar^+ ions with high energy in the range of 500 eV-5 keV in our case. Recently, an Ar cluster ion source has been introduced for sputtering to minimize the change of chemical information caused by the ion

beam. Various sizes (750-3000) and energies (1-8 keV) of the cluster are available for this ion source.

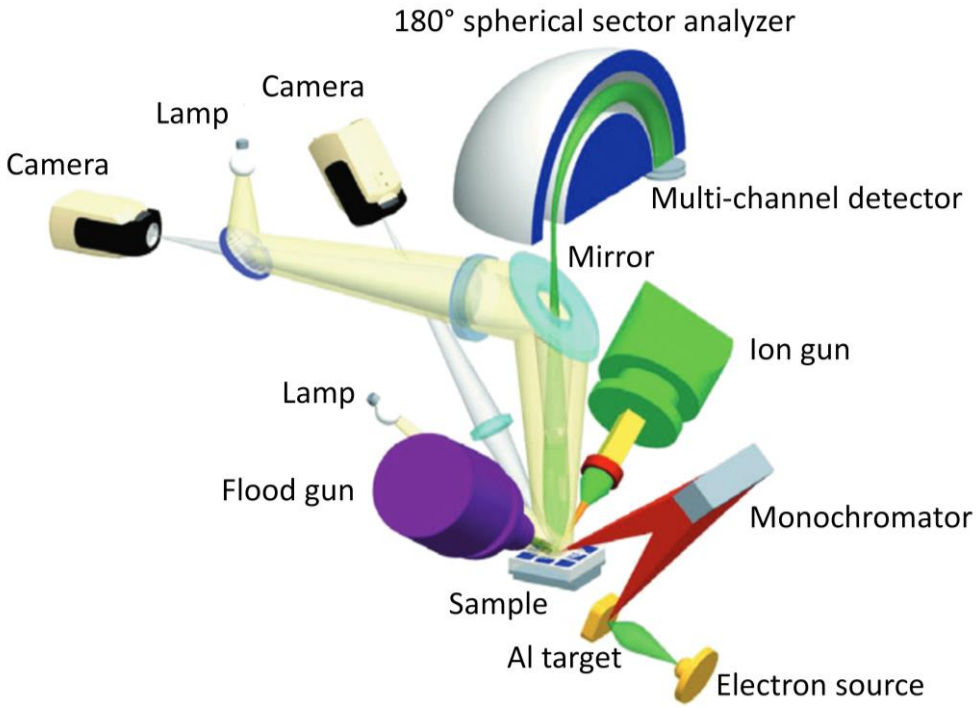

Figure 3.3: Scheme of a K-Alpha XPS instrument (*139*).

A typical XPS spectrum is a plot of the photoelectron intensity vs. binding energy. Figure 3.4 is a survey (wide-scan) spectrum of Al_2O_3 powder with annotations of peaks originating from both photoelectrons and Auger electrons. This XPS survey spectrum with elemental information is obtained using high pass energy over 120 eV and a large binding energy window over 1200 eV. The background of the survey spectrum is stronger with the increasing binding energy. Because high binding energy refers to low kinetic energy and photoelectrons with low binding energy will experience more scattering during their emission. As a result, more photoelectrons with continuous energy are observed at higher binding energy.

In order to gain more chemical information, high-resolution spectra measured at a low pass energy (10-50 eV) and a narrow binding energy window (10-40 eV) are fitted, as exemplarily presented in the upper left corner of Figure 3.4. The Al 2p spectrum is fitted with a doublet consisting of $2p_{3/2}$ (cyan peak) and $2p_{1/2}$ (orange peak) after subtracting the background with a (Shirley) function (magenta line). The first number 2 in $2p_{3/2}$ and $2p_{1/2}$ refers to the principal quantum number n, character p refers to the angular momentum quantum number l, the

subscripts 3/2 and 1/2 refer to the total angular momentum quantum number j, which is given by:

$$j = l \pm s \qquad \text{Equation 3.3}$$

where s = ±1/2 is the electron spin angular momentum quantum number. The shape of the fitted peak (red line) is determined by one or more Voigt functions as well as by the convolution of Cauchy-Lorentz and Gaussian functions. The quality of the fitting is described by the Abbe criterion and Chi-square.

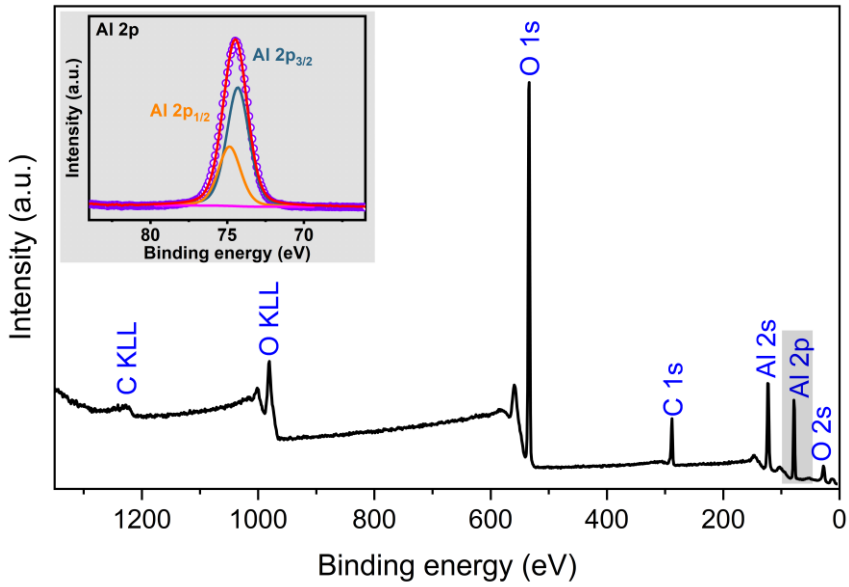

Figure 3.4: Survey spectrum of Al_2O_3 powder with an insetted diagram of fitted Al 2p.

Full width half maximum (FWHM) of the peak, determined by natural line broadening and spectrometer broadening, is a useful indicator for the changes of chemical state and physical conditions. The value of FWHM decreases with increasing angular momentum quantum number l (f < d < p < s). The binding energy for the corresponding peak will change if the chemical bonding environment of the element changes. This difference in the binding energy is called chemical shift, which includes information about the chemical composition, functional groups, and oxidation states. The quantitative chemical composition of the measured area can be calculated in atomic percent by the following equation:

$$C_x = (I_x/S_x):\Sigma(I_i/S_i) \qquad \text{Equation 3.4}$$

where C_x, I_x, and S_x refer to the atom fraction, the peak area, and relative sensitivity factor (RSF) of element x, respectively. $\Sigma(I_i/S_i)$ is the sum of the ratio of the peak area and corresponding RSF for all elements in the measuring area.

3.2 Electrochemical impedance spectroscopy

Electrochemical impedance spectroscopy (EIS) is a non-destructive technique providing time-dependent information about the system. The concept 'impedance', which describes the ability of a circuit to resist the flow of electrical current, is an analogy to resistance. Different from the resistance for an ideal resistor, impedance allows the description of a complex circuit with nonlinear current-voltage relationships. EIS is a frequency domain measurement by applying a small exciting signal to create a perturbation of an equilibrium state. A pseudo-linear system is usually used for battery systems in which the current response I_t to a sinusoidal voltage E_t is measured:

$$E_t = E_0 \sin(\omega t),\ \omega = 2\pi f \qquad \text{Equation 3.5}$$

$$I_t = I_0 \sin(\omega t + \varphi) \qquad \text{Equation 3.6}$$

where E_0 (V) is the amplitude of the signal, t (s) is the time, ω is the radial (angular) frequency (radians/s), f (Hz) is the frequency, I_0 (A) is the amplitude of the signal, and φ (°) is the phase shift between the sinusoidal voltage and current response. The current response over a range of frequencies makes it possible to separate the processes occurring on different timescales, such as electronic and ionic processes in mixed conductors. With Euler's relationship:

$$\exp(i\varphi) = \cos\varphi + i\sin\varphi,\ i = (-1)^{1/2} \qquad \text{Equation 3.7}$$

where i is the imaginary unit. The potential and response current can be expressed as:

$$I_t = I_0\exp(i(\omega t - \varphi)),\ E_t = E_0\exp(i\omega t) \qquad \text{Equation 3.8}$$

The impedance Z can then be calculated by:

$$Z = E_t/I_t = |Z|\exp(i\varphi) = |Z|\cos\varphi + i|Z|\sin\varphi \qquad \text{Equation 3.9}$$

The impedance Z can be divided in the imaginary part Z'' and the real part Z' as described by the following equation:

$$Z = Z' + jZ''\ (Z' = |Z|\cos\varphi\ \&\ Z'' = |Z|\sin\varphi) \qquad \text{Equation 3.10}$$

One of the most popular formats to present electrochemical impedance data is the Nyquist plot, as shown in Figure 3.5 (a), in which the imaginary impedance part (Z") against the real impedance part (Z') at each excitation frequency is plotted. It is easy to obtain ohmic resistance by the crosspoint of the x-axis and the extrapolated semicircle. Three crosspoints can be observed in Figure 3.5 (a) by extrapolation and they correspond to the ohmic

resistances of R_0, R_1, and R_2. The capacitance can be calculated based on resistance and frequency by:

$$C_1 = 1/2\pi f_1 R_1,\ C_2 = 1/2\pi f_2 R_2 \qquad \text{Equation 3.11}$$

where C_1 and C_2, R_1 and R_2 are capacitances (F) and ohmic resistances (Ω) corresponding to the small and large semicircles, respectively. f_1 and f_2 are frequencies (Hz) on the top of the small and the large semicircles.

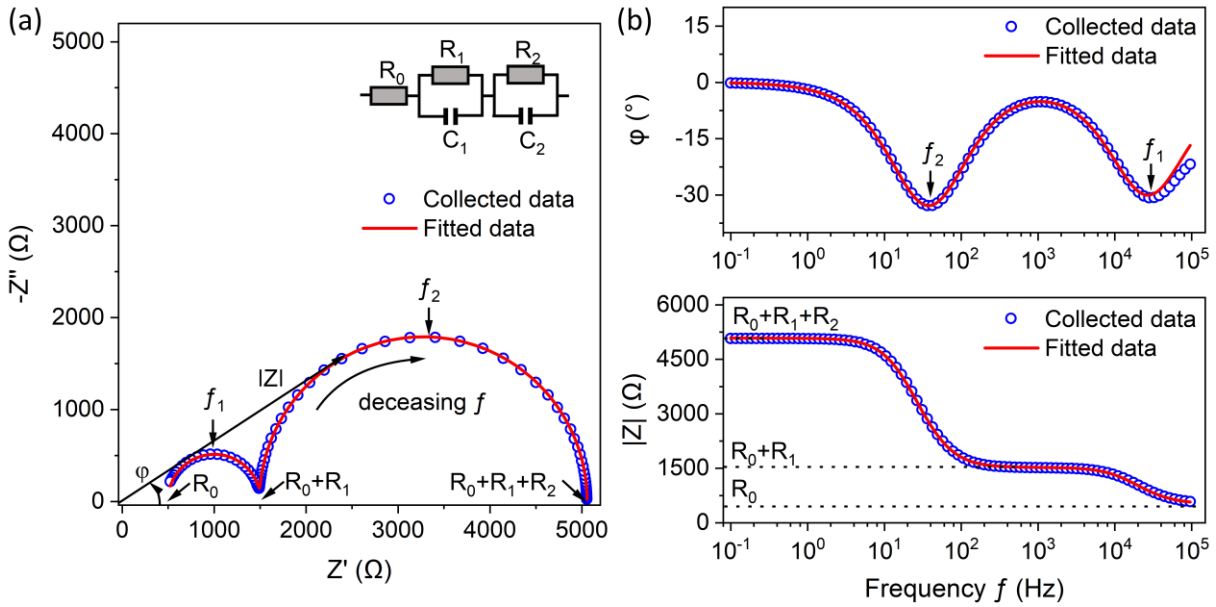

Figure 3.5: Nyquist plot inserted with an equivalent circuit (a) and Bode plot (b) of a test box.

However, a frequency does not appear explicitly in a Nyquist plot. Therefore, so-called Bode plots (Figure 3.5 (b)) consisting of two diagrams of phase angle φ vs. frequency (diagram above) and the absolute value of the impedance |Z| vs. frequency (diagram below) show a clear relationship between impedance and frequency. Three plateaus in Figure 3.5 (b) below refer to the three crosspoints in the left Nyquist plot and two valleys in Figure 3.5 (b) above refer to the two semicircles in the corresponding Nyquist plot.

The blue hollow points in Figure 3.5 are the measured data, while the red lines are the fitting results using the equivalent circuit insetted in Figure 3.5 (a). The semicircle in a Nyquist plot is characteristic of a single "time constant", which represents a parallel combination of a resistor and a capacitor. The common elements used in the equivalent circuit are listed in Table 3.1. These theoretical circuit elements are attributed to physical processes in an electrochemical system, such as double layer capacitance, polarization resistance, charge transfer resistance,

diffusion, etc. In addition to the ideal resistor (R), capacitor (C), and inductor (L), the constant phase element (CPE) is also introduced to represent the imperfect capacitor in reality, which means the center of the semicircle in the Nyquist plot is not located on the x-axis. The exponent α of a CPE is in the range of $0 < \alpha < 1$ and $Y_0 = 1/|Z|$ at $\omega = 1$ rad/s. When $\alpha = 1$, the CPE behavior corresponds to an ideal capacitor. When $\alpha = 0.5$, it is called Warburg element (W) corresponding to the diffusion-controlled electrochemical reaction. The Warburg impedance appears as a diagonal line with a slope of 45° in the Nyquist plot and it is located in the midway of a resistor (0° phase shift) and a capacitor (90° phase shift).

Table 3.1: Common equivalent circuit elements.

Equivalent Element	Resistor (R)	Capacitor (C)	Inductor (L)	CPE (Q)	Warburg (W)
Impedance	R	$1/j\omega C$	$j\omega L$	$1/Y_0(j\omega)^{\alpha}$	$1/Y_0(j\omega)^{1/2}$

Based on the resistance (R) obtained by fitting the EIS spectrum, the ionic conductivity of an SE can be given by:

$$\sigma = l/RA \qquad \text{Equation 3.12}$$

where l (cm) is the thickness of the SE pellet and A (cm^2) is the cross-sectional area of the SE pellet.

3.3 Time-of-flight secondary ion mass spectrometry

Time-of-flight secondary ion mass spectrometry (ToF-SIMS) is an extremely surface-sensitive technique that enables the detection of all elements and their isotopes with low detection limits ranging from parts per million (ppm) to parts per billion (ppb) on the 1-2 nm outmost surface. Figure 3.6 (a) illustrates the structure of a typical ToF-SIMS instrument. The primary ion gun using a liquid metal ion beam source, such as Bi^+_x, can provide a pulsed, energetic ionic probing beam (25-30 keV) that bombards the surface of the sample leading to a collision cascade and correlated atomic motion in the solid. Different particles such as secondary ions, molecular ion fragments, and neutral atoms are ejected during this process, but only about 5 % of them are positively or negatively charged ions and therefore extracted to the time-of-flight detector mass spectroscopy. The emission of these secondary ions can be described by the basic SIMS equation:

$$I_x = I_p C_x S \gamma \eta \qquad \text{Equation 3.13}$$

where I_x is the secondary ion current of species x, I_p is the primary ion beam current, C_x is the concentration of species x in the surface layer, S is the sputter ion yield of species x, γ is the ionization efficiency, and η is the transmission of the analysis system. Even if the intensity of secondary ions is proportional to the concentration, quantification by using ToF-SIMS is not straightforward. The ionization efficiency also contributes to the measured secondary ion counts and it depends on the element and electronic state of the surface. The quantification via ToF-SIMS is only possible when there is a relevant standard that is not easy to prepare accurately.

In the ToF analyzer, all the collected secondary ions are accelerated to the same kinetic energy E_k through an extraction plate held at a fixed potential U:

$$E_k = qU = mv^2/2 \qquad \text{Equation 3.14}$$

where q and m are the charge and mass of the secondary ions, respectively. The velocity of the secondary ions can be calculated based on the time, which is needed for the flight of secondary ions through the flight tube t and the length of the field-free flight tube L:

$$v = L/t \qquad \text{Equation 3.15}$$

By combination of Equation 3.14 and Equation 3.15, we can get the relationship between the mass to charge ratio (m/q) and the time-of flight:

$$m/q = (2U/L^2)t^2 \qquad \text{Equation 3.16}$$

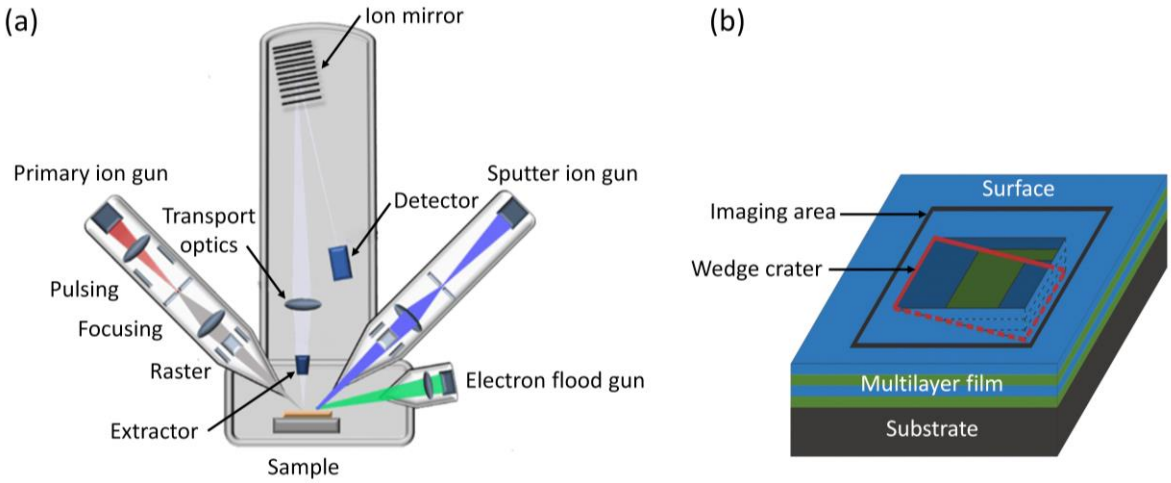

Figure 3.6: Scheme of a ToF-SIMS instrument (b) and top view of the wedge crater (b) (*140*).

A ToF-SIMS spectrum of intensity vs. mass to charge ratio (m/q) is obtained by an individual primary ion pulse. This high mass resolution spectrum gives specific chemical information

about the outmost surface layer since the secondary ions are separated according to their mass-to-charge ratio (m/q). Chemical imaging of the lateral secondary ions distribution in submicron resolution can be achieved by scanning the primary ions over the surface using the raster. Sputter depth profiling via ToF-SIMS is also possible by alternative erosion using a sputter ion gun (Cs^+, O_2^+, Ar^+, gas cluster ions) and measurement (spectrum or imaging) using the primary ion gun. An electron flood gun is used to compensate for the charges and to improve the signal intensity during the measurement. To maximize the depth resolution and minimize the material damage caused by sputtering, a wedge crater sputtering strategy is applied as shown in Figure 3.6 (b). A beveled structure (red rectangular) with a small angle with respect to the surface is cut into the multilayer film to laterally amplify the buried film. In this way, the nanoscale multilayer structure of the thin film can be better resolved using ToF-SIMS imaging (black rectangular).

3.4 X-ray diffraction

X-ray diffraction (XRD) is a non-destructive technique to characterize the atomic-scale structure of various substances, especially for crystalline materials. During the XRD measurement, a monochromatic X-ray beam is created by a cathode tube, and then collimated and directed onto the sample. The interaction between the incident X-ray and the sample can produce constructive interference when Bragg's equation is satisfied:

$$n\lambda = 2d\sin\theta \qquad \text{Equation 3.17}$$

where n is an integer, λ is the wavelength of the X-rays, d is the distance between lattice planes, and θ is the angle of incidence of the X-ray on the lattice plane. In other words, the scattered waves interfere constructively when the difference of path length of two waves ($2d\sin\theta$) is equal to an integer multiple of the wavelength ($n\lambda$), as illustrated in Figure 3.7. This diffracted X-ray is detected after interference at different angles by rotating the sample holder and the detector. The peak intensities (y-axis) of the XRD pattern are determined by atomic parameters while the peak positions 2θ (x-axis) give information on unit cell parameters.

In X-ray powder diffraction, constructive interference will occur in those crystallites that fulfill the Bragg condition. Since the powdered material is randomly orientated, all possible diffractions are attained by scanning the sample over an angle range of 2θ. By comparing with

the standard X-ray powder diffraction patterns from databases, the phase of the measured sample can be easily identified. For the characterization of a thin film, conventional XRD will produce a strong signal from the substrate of the film. By decreasing the incident X-ray angle to a low fixed grazing angle, known as grazing incidence XRD (GIXRD), the penetration depth of the X-ray can be significantly reduced and consequently eliminates the undesired diffraction from the substrate. This feature indicates that GIXRD is a suitable method to study the crystalline structures of thin films as well as surfaces.

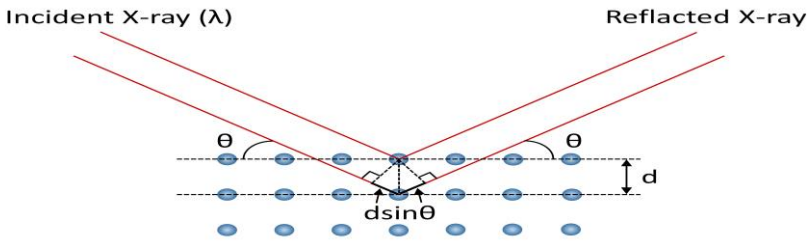

Figure 3.7: Schematic representation of Bragg's equation.

3.5 Scanning electron microscopy and energy-dispersive x-ray spectroscopy

Scanning electron microscopy (SEM) is a very common instrument to characterize the surface topography of a sample. In a typical SEM measurement, an electron beam is generated by a hot filament cathode or a field emission cathode and accelerated to a certain energy by an electric field. This electron beam is then focused by electromagnetic lenses and scanned in a raster scan pattern toward the sample to obtain an image. All these processes are run in a vacuum system ($< 10^{-5}$ mbar). During the interaction of the electron beam with the sample, three signals are generated providing the greatest amount of information in SEM and energy-dispersive x-ray spectroscopy (EDX) measurements: secondary electrons, back-scattered electrons, and characteristic X-rays.

Secondary electrons are the most widely used signal for topographical characterization. These electrons are generated by inelastic scattering of the electrons, i.e., the interaction of incident electrons with electrons or atoms of the sample resulting in a loss of electron energy. Due to their low energy (less than 50 eV), secondary electrons can only escape from a region within

a few nanometers of the material surface. Therefore, secondary electrons are principally used to provide high-resolution topographical contrast in SEM.

Back-scattered electrons are generated by elastic scattering of incident electrons with atomic nucleus or outer shell electrons without much energy loss. The intensity of deflected back-scattered electrons depends on the atomic number of the material. Hence, back-scattered electrons are primarily used to provide atomic number contrast in SEM. Nevertheless, the resolution of such an image is limited by the large penetration depth (1 µm) of back-scattered electrons due to their high electron energy (> 50 eV). When the incident electron beam strikes the sample, some vacancies will be created in the inner shell.

Characteristic x-rays are produced when the outer shell electrons fall into the vacancies in the inner shell. The energy of these characteristic X-rays is determined by the energy difference of these two orbitals in outer and inner shells, which gives elemental information of the sample. One of the most used equipments for the detection of X-rays is energy dispersive x-ray detector. The technique using characteristic X-rays to identify the element (atomic number 4-92) is called energy-dispersive x-ray spectroscopy (EDX).

3.6 Magic-angle spinning nuclear magnetic resonance spectroscopy

Magic-angle spinning nuclear magnetic resonance spectroscopy (MAS NMR) is a very useful tool for the structural characterization of solid materials. In an NMR spectrometer, the nuclei of an isotope placed in a strong constant magnetic field are excited by a radio-frequency pulse and then an electromagnetic response with frequency characteristic to this excitation, the so-called free induction decay (FID), is detected. An NMR spectrum of intensity vs. chemical shift is obtained by Fourier transformation of the FID response, in which the chemical shift is measured in frequency versus a reference. The so-called nuclear magnetic resonance occurs when the frequency of the RF pulse is consistent with the intrinsic frequency of the nuclei, which is determined by the static magnetic field, the chemical environment, and the magnetic properties of the isotope. Based on the specific magnetic properties of certain atomic nuclei, NMR delivers physical, chemical, electronic, and structural information about molecules.

In solution/gas NMR spectra, the peaks are very sharp due to the averaging of anisotropic NMR interactions by rapid random tumbling. For solid-state NMR, however, the peaks are broadened because of the anisotropic interactions of direct dipole-dipole interactions, chemical shift anisotropy (CSA), and quadrupolar interactions. The dipole-dipole interaction refers to the interaction through a space between the observed nucleus and the neighboring nuclei, which provides information on internuclear distances and angles. The CSA refers to the shielding effect of the surrounding shells of electrons, which gives information on the local chemical environment. The quadrupolar interaction refers to the interaction between the nuclear electric quadrupole moment and the surrounding electric field gradient produced at the nuclear site by a nonspherical charge distribution around the nucleus when the nuclear spin number is larger than 1/2. The information about the charge distribution and local environment can be obtained from the quadrupolar interaction. To narrow the peak broadening caused by these three interactions, magic-angle spinning (MAS) by rotating solid samples at an angle of $\theta_m = 54.74^\circ$ with respect to the direction of the magnetic field is widely applied. Both dipole-dipole interactions and the chemical shift anisotropy depending on the geometric factor ($3\cos^2\theta-1$) are then averaged to 0. The quadrupolar interaction is also partially averaged by MAS. Therefore, MAS NMR of a solid powdered material behaves similarly to conventional NMR of a solution/gas. Although the resolution of NMR spectra of solid samples is improved by applying MAS, the anisotropy and geometry information is sacrificed due to the averages of dipole-dipole interactions and CSA.

3.7 Raman spectroscopy

Raman spectroscopy is a widely used vibrational spectroscopic technique to investigate the unique “chemical fingerprints” of solid and liquid samples. A Raman spectrum is normally obtained by irradiating a sample with an intense laser beam and then collecting the electromagnetic radiation from the illuminating spot. When the monochromatic light (laser beam) irradiates the sample, a fraction of the beam is scattered either elastically or inelastically in all directions. For elastic scattering, the scattering radiation has the same frequency (wavelength) as the incident radiation, which is known as Rayleigh scattering. The inelastic scattering also called Raman scattering is composed of stokes scattering and anti-stokes scattering. During stokes scattering, the molecules are excited from the ground state

to a virtual state and then end with a vibrationally excited state after photon scattering. Different from that, the initial state of anti-Stokes scattering is the vibrationally excited state and the final state is the ground state. Hence, the scattering radiation of Stokes scattering has a lower frequency than the incident light, while the anti-Stokes scattering has a higher frequency than the incident light. Stokes and anti-Stokes contain the same frequency information but the former has an appreciably intenser signal than the latter. As a result, Stokes scattering at some angle (normally 90°) is generally used for Raman spectroscopy. A spectrum of scattering intensity vs. Raman shift is plotted after the detection of Raman scattering photons where the Raman shift in wave numbers cm^{-1} refers to the frequency difference of the incident photon and scattered photon. The scattering intensity is proportional to the polarizability and the concentration of the molecules and the Raman shift is determined by the vibrational energies associated with the bonds of the molecules. Therefore, Raman spectroscopy is a very practical tool to identify the molecules in the gas, liquid, or solid samples.

3.8 White light interferometry

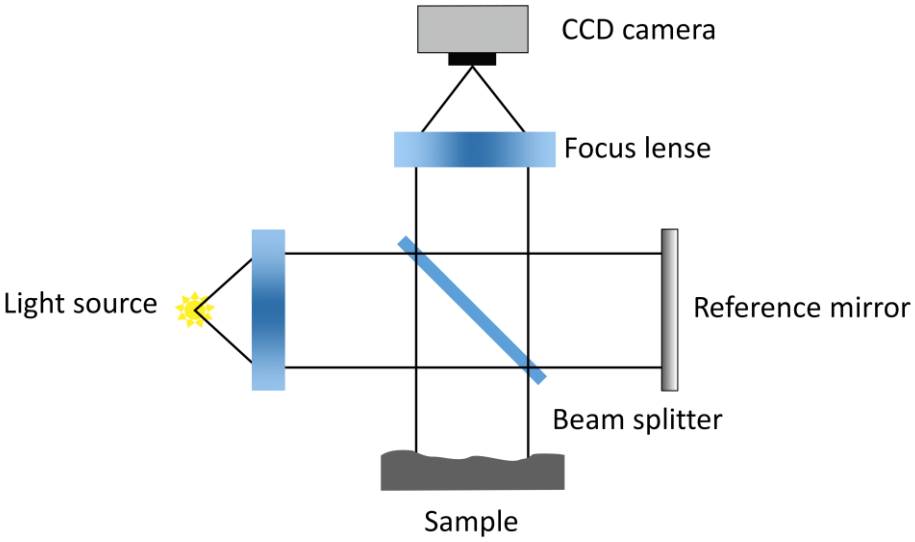

Figure 3.8: Scheme of a WLI system.

White light interferometry (WLI) is a well-known optical measurement technique to characterize surface roughness and 3D surface geometry. In a typical WLI, as shown in Figure 3.8, a broadband “white light” source is separated into reference and measurement beams by a beamsplitter. The reference beam is reflected by the mirror, while the measurement beam

is reflected or scattered by the sample surface. A phase difference between these two beams is introduced because of their different optical traveling paths. A different height of the sample surface means different measurement beam paths resulting in a phase pattern mixed with the reference light beam. Interference of these two beams occurs when the optical path difference is altered less than half the coherence length of the light source by scanning the objective. The surface is reconstructed based on the interference pattern projected on the CCD camera.

3.9 Transmission electron microscopy

Transmission electron microscopy (TEM) is one of the most advanced techniques for the analysis and visualization of samples down to atomic resolution. Almost all of the components in TEM are the same as in SEM. The electron source can be produced by thermionic emission or in a process called cold field emission. The electrons are then accelerated through a high potential of 40 to 100 kV and transferred to the sample by electromagnetic lenses. When the primary electron beam passes through the thin sample, various contrasts could be obtained, such as bright field contrast and diffraction contrast. A bright-field contrast is formed directly by the occlusion and absorption of electrons in the sample. Darker areas in the image represent regions where few electrons have been transmitted through the sample due to large thickness or high atomic number, whilst regions with less sample in the beam path will appear bright. A diffraction contrast is obtained by Bragg's scattering of the incident electrons in a crystalline sample. This pattern gives information about the orientation, atomic arrangements, and phases in the measured area.

4 Bulk-Type Solid Electrolyte (100-x)Li_3PS_4-xLi_3PO_4

This chapter concentrates on the investigation of bulk-type SEs (100-x)Li_3PS_4-xLi_3PO_4. Section 4.1 explains the motivation of the research on heterogeneous Li_3PS_4-Li_3PO_4. The preparation of oxysulfides and the descriptions of corresponding characterization methods and electrochemical tests are then presented in section 4.2. Section 4.3 shows a detailed discussion of the results concerning powder characterization, ionic conductivity, and electrochemical performance of heterogeneous oxysulfides. These results are concluded in the last section of 4.4.

4.1 Introduction

ASSBs using SEs have attracted a lot of attention because they are safer and more reliable compared to traditional LIBs with liquid electrolytes. Li_2S-P_2S_5 binary ionic conductors are one of the most promising SEs due to their high ionic conductivity over 10^{-3} S/cm at RT and a broad electrochemical stability window of more than 5 V (*141*, *142*). Furthermore, owing to their mechanical properties, the grain boundary resistance of these Li_2S-P_2S_5 binary SEs can largely be reduced by simple cold pressing and a favorable solid-solid contact at the electrode-electrolyte interface can easily be obtained. An important drawback of such sulfide SEs is their hygroscopic nature that leads to structural change and the generation of H_2S gas (*143*). It is reported that the Li_2S-P_2S_5 with the composition of 75 mol % Li_2S generated the least H_2S in the Li_2S-P_2S_5 binary system (*144*). With this in mind, 75Li_2S-25P_2S_5 (Li_3PS_4) was prepared by planetary ball milling of Li_2S and P_2S_5 as the first step of synthesis in this work.

In 1973, C.C. Liang discovered the enhancement of ionic conductivity by dispersing an insulator into a conductor in the composite system of LiI-Al_2O_3, which is called insulator dispersion effect (*145*). J. Maier explained the origin of this enhancement based on the space charge effect at the heterointerface, which leads to the redistribution of charge carriers and defects (*31–33*). Based on this background, the poor conductor Li_3PO_4 was used as a heterogeneous dopant to improve the conduction performance of sulfide SEs (*146–149*). Moreover, partial heterogeneous doping of oxygen for sulfur can also stabilize the sulfide SEs towards moisture, enhance the electrochemical stability, and improve the cyclability in ASSBs (*150–154*). Takada

et al. reported heterogeneous (100-x)Li_3PS_4-xLi_3PO_4 with enhanced conductivity obtained by adding Li_3PO_4 via a quenching method (*146*). Huang et al. prepared amorphous powders 70Li_2S-(30-x)P_2S_5·xLi_3PO_4 via high-energy ball milling, which showed the highest RT conductivity of 1.9×10^{-3} S/cm when x = 1 mol % (*147*). The authors attributed the higher discharge capacity of the $LiCoO_2$ to the enhanced conductivity of the SE and reduced interface resistance of the electrode-electrolyte interface. A similar trend was found by Mo et al. in heterogeneous 95(70Li_2S-30P_2S_5)·5Li_3PO_4 glass electrolyte, where the ionic conductivity, electrochemical stability, and cyclability were improved by doping with Li_3PO_4 (*149*). More recently, Phuc et al. prepared 100Li_3PS_4-xLi_3PO_4 by liquid-phase synthesis with enhanced conductivity compared to pure Li_3PS_4 (*148*). The sample with x = 6 shows the best stability against Li and best cycling performance in their report. Despite these studies, a systematic investigation of Li_3PO_4 doped sulfide heterogeneous composite prepared by mechanical milling is of great value. Therefore, heterogeneous (100-x)Li_3PS_4-xLi_3PO_4 ($10 \leq x \leq 40$) was prepared by ball milling of calcined Li_3PS_4 and Li_3PO_4 in this work. The structural and compositional properties of these heterostructured oxysulfides were characterized by various methods. The influences of heterogeneous Li_3PO_4 doping on the conductivity and stability against Li are investigated, and the final ASSBs were studied by corresponding electrochemical measurements.

4.2 Experimental

4.2.1 Synthesis

Heterogeneous (100-x)Li_3PS_4-xLi_3PO_4 raw powders were prepared by a two-step mechanical milling. The Li_3PS_4 glass was prepared by the first step of mechanical milling of 75 mol % Li_2S (Sigma-Aldrich, 99.98 %) and 25 mol % P_2S_5 (Sigma-Aldrich, 99.9 %). A batch of about 4 g of this sulfide mixture and 70g ZrO_2 balls with a diameter of 3 mm were placed in a 45 ml ZrO_2 bowl in an argon-filled glovebox (MBraun, Germany). The mixture was ball milled at 510 rpm for 540 cycles (5 min milling followed by a 15 min rest for cooling) using the planetary micro mill Pulverisette 7 Premium line (Fritsch, Germany). To prepare glass-ceramic β-Li_3PS_4, the glassy Li_3PS_4 was calcined at 250 °C under vacuum in a glass oven (Büchi, Germany) for 2 h and slowly cooled down to RT at a natural rate. β-Li_3PO_4 was prepared by a wet chemical reaction of 75 mol % 1 M LiOH and 25 mol % 1 M H_3PO_4. LiOH·H_2O (Sigma-Aldrich, 99 %) and H_3PO_4

(Carl Roth, 85 %) were weighed and dissolved in deionized water separately to prepare 1 M LiOH solution and 1 M H_3PO_4 solution. The LiOH solution was added to the 1M H_3PO_4 solution gradually with a molar ratio of 3:1 and the mixed solution was stirred at 80 °C for 6 h. After filtration and rinsing of Li_3PO_4 precipitation, the product was dried at 130 °C for 24 h, ground for 15 min, and then calcined at 300 °C for 16 h in a muffle furnace (P330, Nabertherm) to obtain β-Li_3PO_4. The oxygen was introduced to the sulfide by the second step of mechanical milling of the as-prepared glass-ceramic β-Li_3PS_4 and β-Li_3PO_4. Both powders were weighed with a certain molar ratio ($10 \leq x \leq 40$) and mixed in an agate mortar in a dry argon-filled glovebox. The mixture was then put into a 45 ml ZrO_2 bowl and milled with the same ball milling process as for glassy Li_3PS_4 for 80 h to obtain heterogeneous (100-x)Li_3PS_4-xLi_3PO_4.

4.2.2 Material characterization

X-ray diffraction (XRD) patterns were collected using an STOE Stadi P powder diffractometer (STOE & Cie GmbH, Germany) equipped with a Mythen1K detector and Mo $K_{\alpha1}$radiation (λ= 0.70932 Å). The powder samples for XRD measurement were sealed in quartz glass capillaries with a diameter of 0.5 mm under argon atmosphere. Raman spectra were recorded with a LabRAM HR Evolution spectrometer (HORIBA Scientific, Japan) using a 50x magnification objective, an excitation wavelength of 632.8 nm, and a 600 g/mm grating. The samples were measured in sealed glass capillaries with a diameter of 0.5 mm. All Raman spectra were baseline-corrected and normalized to sum using the Horiba LabSpec 6 software. X-ray photoelectron spectroscopy (XPS) was performed using a K-Alpha or a K-Alpha$^+$ spectrometer (ThermoFisher Scientific, UK) equipped with a microfocused, monochromated Al K_α X-ray source (*λ*=1486.6 eV) with a spot size of 400 µm. A charge compensation system was employed during the measurement, using electrons of 8 eV energy and low-energy argon ions to prevent localized charge accumulation. All samples were prepared in an argon-filled glovebox and transferred under an inert atmosphere into the spectrometer. Thermo Avantage software was used in data acquisition and processing, as described elsewhere (*155*). The analyzer transmission function, Scofield sensitivity factors, and effective attenuation lengths for photoelectrons were applied for quantification (*156*). The standard TPP-2M formalism was used for the calculation of effective attenuation lengths (*138*). All spectra were referenced to the carbonaceous C 1s peak (C–C/C–H) at 285.0 eV binding energy. ^{31}P Magic-angle spinning

(MAS) nuclear magnetic resonance (NMR) spectra were obtained at a spinning speed of 30 kHz on an Avance 500 MHz spectrometer (Bruker, Germany) at a field of 11.7 T, corresponding to a resonance frequency of 202.5 MHz. The powder samples were packed into 2.5 mm ZrO_2 MAS rotors in an argon-filled glovebox. A rotor-synchronized Hahn-echo pulse sequence was used for data acquisition. The chemical shift of ^{31}P was referenced to H_3PO_4 (85 %, 0 ppm). Scanning electron microscopy (SEM) images were recorded by a Zeiss Merlin microscope (ZEISS SMT AG, Germany) with 5 kV acceleration voltage. Energy-dispersive X-ray spectroscopy (EDX) was performed using a 60 mm^2 XFlash (Brucker, Germany) detector equipped in the SEM. The samples were transferred under Ar into the chamber of the SEM.

4.2.3 Electrochemical characterization

The SE powders of (100-x)Li_3PS_4-xLi_3PO_4 (60mg) were pre-pressed using a pressing die with a diameter of 8 mm via a manual hydraulic press (Specac, England) with a pressure of 50 MPa for 10 s at RT. For the preparation of a Li symmetric cell Li/(100-x)Li_3PS_4-xLi_3PO_4/Li, the pre-pressed pellet was placed inside an in-house cell and pressed again at 400 MPa for 2 min at RT. The thickness of the repressed pellet was about 720 µm. Two Li foils (Rockwood Lithium, 200 µm) with a diameter of 4 mm were then attached on both sides of the pellet in the cell. The structure of the in-house cell is displayed in Figure 4.1 (*157*). Li-In alloy was used as the negative electrode instead of Li metal for the preparation of an ASSB Li-In/(100-x)Li_3PS_4-xLi_3PO_4/$LiCoO_2$ due to its improved interface resistance (*158*). $LiCoO_2$ powder (Sigma-Aldrich, 99.8 %) and (100-x)Li_3PS_4-xLi_3PO_4 powder at a weight ratio of 7:3 were ground for 20 min with an agate mortar to obtain the positive electrode for the full cell. 6 mg of the mixed electrode powder was then pre-pressed with a pressure of 50 MPa for 10 s. The pre-pressed electrolyte pellet was put on the pre-pressed electrode in the cell and then pressed with 400 MPa for 2 min at RT. The same Li foil as used in the symmetric cell (1.5 mg) together with an In foil (MaTecK, 99.99 %, 125 µm) with a diameter of 7 mm was pressed on the top of the electrolyte pellet serving as the negative electrode. All processes were carried out in an argon-filled glovebox with contents of H_2O and O_2 less than 1 ppm.

All electrochemical measurements were performed using a multichannel potentiostat VMP3 (Bio-Logic, Germany). Electrochemical impedance spectroscopy (EIS) was conducted on the Li

symmetric cell Li/(100-x)Li_3PS_4-xLi_3PO_4/Li with a signal amplitude of 20 mV at frequencies from 1 MHz to 500 mHz over a temperature range of 5-75 °C controlled by a temperature chamber Model 115A (TestEquity, USA). The EIS data were analyzed using the software Relaxis 3 (rhd Instruments, Germany). Time-resolved EIS for Li symmetric cells and normal EIS for the cycled ASSBs were conducted at 15 °C. Cyclic voltammetry (CV) measurement was conducted on the Li symmetric cell in the voltage range of 0.5-10.0 V vs. Li^+/Li at a scan rate of 5 mV/s at 25 °C. For galvanostatic cycling tests, the Li symmetric cells Li/(100-x)Li_3PS_4-xLi_3PO_4/Li were subsequently charged and discharged at a current density of 100 µA/cm^2 for 1 hour at 25 °C. While the full cells Li-In/(100-x)Li_3PS_4-xLi_3PO_4/$LiCoO_2$ were cycled at a current of C/10 (1C = 120 mAh/g) within the discharge and charge cut-off voltages of 2.0 V and 4.2 V at 25 °C. The rate capability of the full cells was performed by cycling the cells with increasing C-rate (C/20, C/10, C/5, and C/2) and finally again C/20 for 5 cycles at each rate.

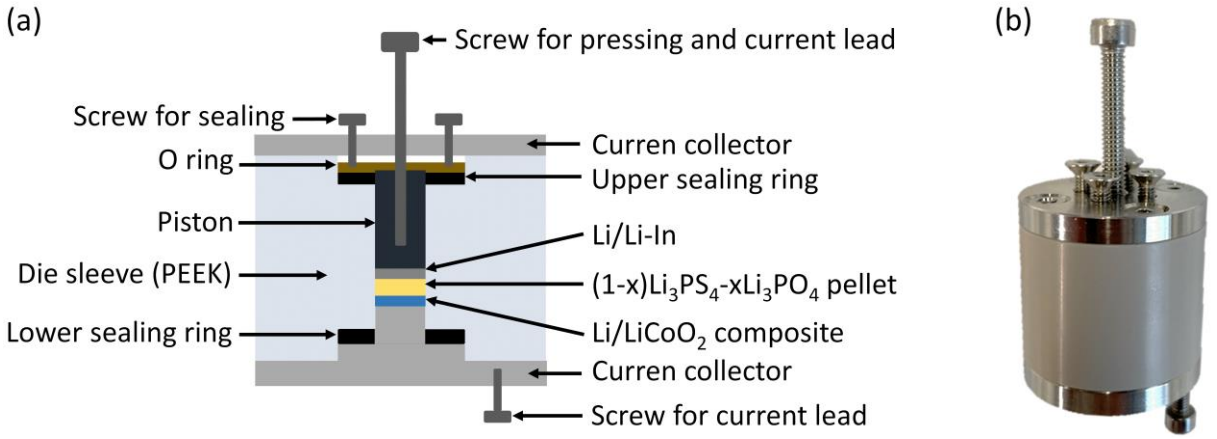

Figure 4.1: Scheme (a) and a picture (b) of the cell for SEs.

4.3 Results and discussion

4.3.1 Structural characterization

The XRD patterns of the starting materials Li_2S and P_2S_5 and of the 75Li_2S-25P_2S_5 mixture after ball milling are shown in Figure 4.2 (a). No reflections from either Li_2S or P_2S_5 can be observed in the pattern of 75Li_2S-25P_2S_5 after mechanical milling, indicating that an amorphous glass of 75Li_2S-25P_2S_5 was obtained. Rietveld refinement based on X-ray powder diffraction data of Li_2S and P_2S_5 can be seen in Figure A 1. All reflections of Li_2S can be indexed to the cubic Li_2S structure model with space group Fd-3m and high crystallinity, and the lattice parameters are

a = b = c = 5.7145 Å, in accordance with previously published works (*159*, *160*). With regard to the P_2S_5 material, all reflections can be indexed to the triclinic structure model with space group P-1 and the lattice parameters are a = 8.8658 Å, b = 9.2264 Å, c = 9.1676 Å, α = 92.33°, β = 100.37°, γ = 109.14°. This Rietveld refinement demonstrates phase-pure starting materials of Li_2S and P_2S_5.

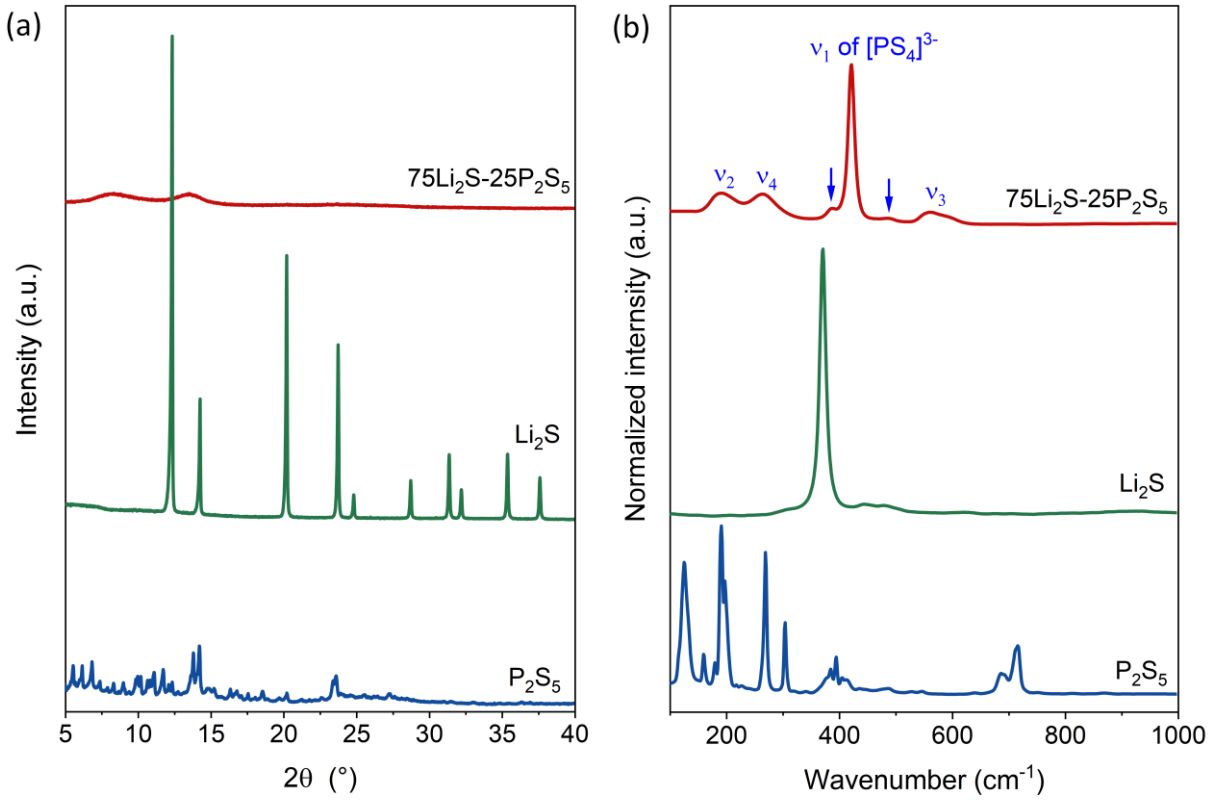

Figure 4.2: XRD patterns (a) and Raman spectra (b) of starting materials Li_2S, P_2S_5, and $75Li_2S$-$25P_2S_5$ after mechanical milling.

Figure 4.2 (b) shows the characteristic Raman spectra of the starting materials Li_2S and P_2S_5 and milled $75Li_2S$-$25P_2S_5$. The Raman spectrum of P_2S_5 is in good agreement with the literature (*161*, *162*). There is a dominant Raman band at 372 cm^{-1} for Li_2S, in accordance with the values in the literature (*160*, *163*). All main bands in the Raman spectrum of the milled mixture of $75Li_2S$-$25P_2S_5$ can be attributed to the internal vibration of the $[PS_4]^{3-}$ anion with T_d symmetry (*164*, *165*). The strongest peak located at around 422 cm^{-1} is assigned to the symmetric stretching vibration of the P-S bonds v_1 in $[PS_4]^{3-}$ units, while the broad peak in the range of 500-600 cm^{-1} corresponds to antisymmetric P-S stretching vibration v_3. Two broad peaks at around 192 cm^{-1} and 265 cm^{-1} are respectively attributable to v_2 symmetric and v_4 asymmetric

S-P-S bending vibrations of tetrahedral $[PS_4]^{3-}$. The small shoulder band at around 389 cm^{-1} is assigned to the units of $[P_2S_6]^{4-}$ (*74*, *166*). It is reported that the inhomogeneous ball milling process is a possible reason for this minor impurity (*167*). Another tiny band at around 486 cm^{-1} arises from polysulfide chain ions, which may be the offset of $[P_2S_6]^{4-}$ to $[PS_4]^{3-}$ (*168*, *169*). Since $[PS_4]^{3-}$ ions are the dominating species observed in the Raman spectrum of the mixture, we may confirm the stoichiometric composition of the milled powder. Taking both the XRD pattern and the Raman spectrum of $75Li_2S$-$25P_2S_5$ into consideration, an amorphous Li_3PS_4 was synthesized after the first step of mechanical milling of Li_2S and P_2S_5.

XRD patterns of self-synthesized β-Li_3PO_4 and calcined β-Li_3PS_4 with the calculated profiles after Rietveld refinement are presented in Figure 4.3 (a) and (b). All reflections of the β-Li_3PO_4 in Figure 4.3 (a) can be indexed to the orthorhombic structure model with space group $Pmn2_1$ and the lattice parameters are a = 6.1225 Å, b = 5.2351 Å, c = 4.8537 Å, which agrees with the β-Li_3PO_4 phase in the literature (*170*, *171*). β-Li_3PS_4 synthesized by calcination of amorphous Li_3PS_4 at 250 °C for 2 h was also investigated with X-ray powder diffraction as displayed in Figure 4.3 (b). All the main reflections can be indexed to the orthorhombic structure model with space group Pnma and the lattice parameters are a = 12.9649 Å, b = 8.0145 Å, c = 6.0785 Å. However, it shows peak broadening due to the poor crystallinity which may arise from the low annealing temperature or short annealing time of 2 h (*172*).

In order to introduce oxygen into $75Li_2S$-$25P_2S_5$, β-Li_3PO_4 and β-Li_3PS_4 were mixed by the second step of mechanical milling. Figure 4.3 (c) shows the XRD patterns of β-Li_3PO_4, β-Li_3PS_4, and the evolution of the heterogeneous mixtures $(100\text{-}x)Li_3PS_4$-xLi_3PO_4 at different molar ratios in the range of $10 \leq x \leq 40$. Compared to the patterns of the starting materials β-Li_3PO_4 and β-Li_3PS_4, the heterogeneous oxysulfides show mixed diffraction patterns of these two initial binary compounds with strong broadening of reflections and intensity decrease of the Bragg reflections, indicating the formation of the heterostructured composites. All the mixed powders remain glass-ceramic after a long-time (80 h) of ball milling. Even if Li_3PO_4 is the minor compound in the heterogeneous mixtures, the reflections of the powder mixtures mainly originate from β-Li_3PO_4, while the diffractions of the major composite β-Li_3PS_4 are not that intensive after long-time mechanical milling, because crystalline Li_3PS_4 is easier to be milled to glass than crystalline Li_3PO_4 owing to their different physical and mechanical properties. As

expected, the intensities of the diffractions have a tendency of reduction with the decreasing content of Li_3PO_4. For the powder with x = 10, the diffractions are very weak and the powder seems to become amorphous.

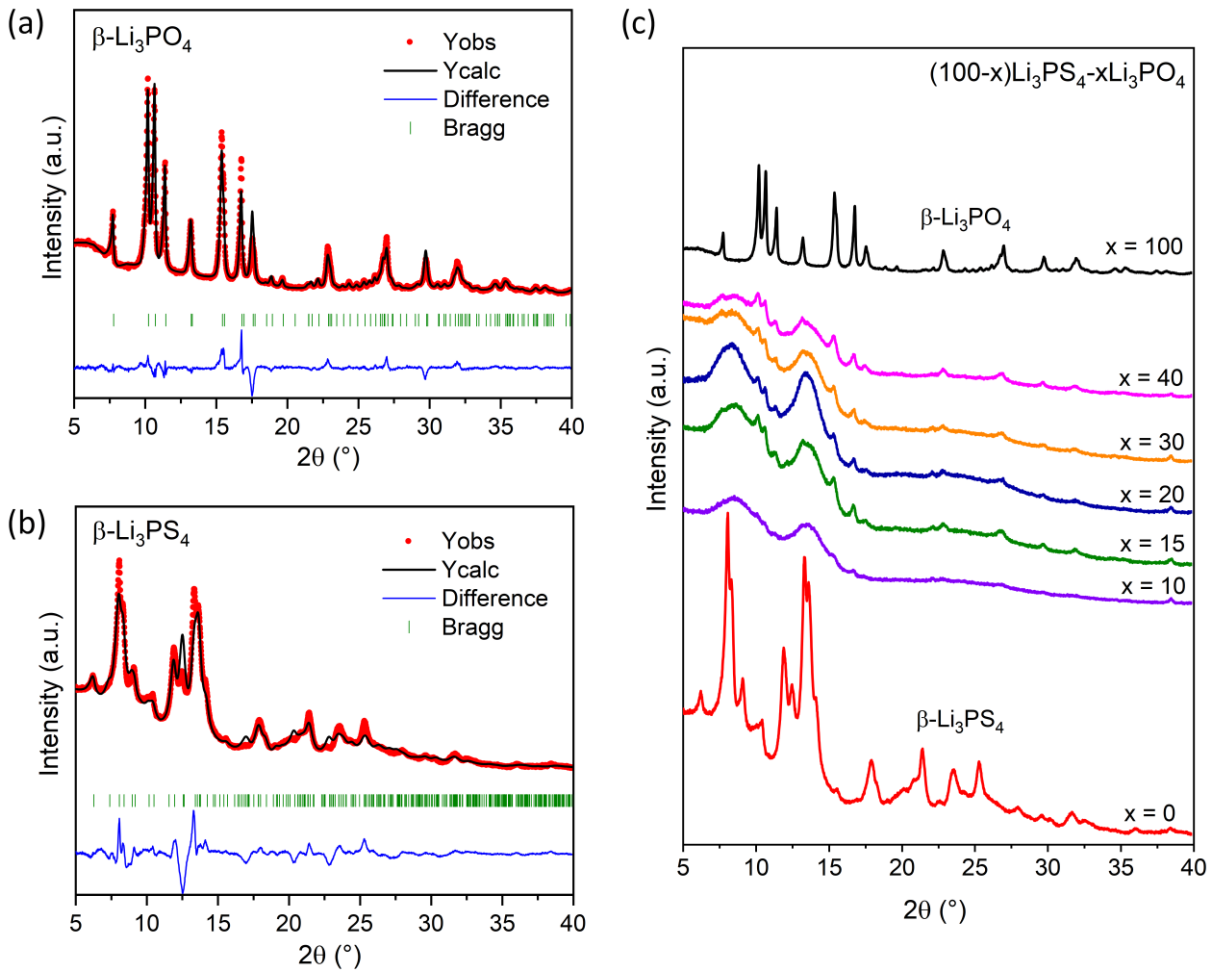

Figure 4.3: Rietveld refinement based on XRD data of starting materials β-Li_3PO_4 (a) and β-Li_3PS_4 (b); (c) XRD patterns of starting materials of β-Li_3PO_4, β-Li_3PS_4, and the evolution of heterogeneous oxysulfides (100-x)Li_3PS_4-xLi_3PO_4 ($10 \leq x \leq 40$).

To investigate the local structure around phosphorus of the heterogeneous glass-ceramics, ^{31}P MAS NMR measurements were performed as displayed in Figure 4.4 (a). According to the literature, the resonances at 10.9 ppm for β-Li_3PO_4 and 86.3 ppm for β-Li_3PS_4 are respectively attributable to the $[PO_4]^{3-}$ and $[PS_4]^{3-}$ units (*173*, *174*). After mechanical milling of β-Li_3PO_4 and β-Li_3PS_4, a broad peak at 83.1 ppm is observed instead of the sharp peak of $[PS_4]^{3-}$ units in all heterogeneous powders. This peak is assigned to the overlap of $[PS_4]^{3-}$ and $[PS_3O]^{3-}$ resonances and the broadening of the line shape again reflects the glass-ceramic property of the

oxysulfide mixtures (100-x)Li_3PS_4-xLi_3PO_4 (*154*). Two additional broad resonances at around 69.5 ppm and 36.3 ppm in the spectra for the milled mixtures are attributed to $[PS_2O_2]^{3-}$ and $[PSO_3]^{3-}$ units, respectively (*175*, *176*). The other two broad resonances at a low chemical shift of 8.8 ppm and -2.8 ppm can be probably attributed to the poorly crystalline orthophosphate tetrahedra $[PO_4]^{3-}$ and dimeric $[P_2O_7]^{4-}$ units after ball milling, respectively (*175–181*). The sharp peak of crystalline $[PO_4]^{3-}$ at 10.9 ppm still exists in the oxysulfide mixtures agreeing with the XRD results that the diffractions of β-Li_3PO_4 remain in the heterogeneous oxysulfides. The presence of the additional units $[PS_3O]^{3-}$, $[PS_2O_2]^{3-}$, $[PSO_3]^{3-}$, and dimeric $[P_2O_7]^{4-}$ units reveal that the sulfur atoms in $[PS_4]^{3-}$ tetrahedra are partially substituted by the oxygen atoms from tetrahedra $[PO_4]^{3-}$. These MAS NMR results demonstrate that the structure of the β-Li_3PS_4 was modified by doping β-Li_3PO_4 via mechanical milling. It is worth noting that long relaxation times (> 30 min) of different samples may lead to selective suppression of the intensity of some of the peaks.

Raman spectroscopy was performed on β-Li_3PO_4 and β-Li_3PS_4, and heterogeneous oxysulfides (100-x)Li_3PS_4-xLi_3PO_4 to investigate the bonding situation. In Figure 4.4 (b), all vibrations of β-Li_3PO_4 are in accordance with the Raman results presented in the literature except for a tiny unknown peak at around 704 cm^{-1}, which is also observed in other publications (*182*, *183*). The strongest Raman peak of β-Li_3PO_4 located at 942 cm^{-1} stems from the symmetrical stretching vibration of the P-O bonds v_1 in $[PO_4]^{3-}$ unit. Raman vibrations of β-Li_3PO_4 located in the ranges of 300-400 cm^{-1}, 450-550 cm^{-1}, 550-650 cm^{-1}, and 980-1100 cm^{-1} are assigned to translation vibration, symmetric bending vibration v_2, asymmetric bending vibration v_4, asymmetric stretching vibration v_3 of $[PO_4]^{3-}$, respectively (*182*). Similar to glass Li_3PS_4, crystalline β-Li_3PS_4 has a dominant peak at 422 cm^{-1} assigned to the symmetrical stretching vibration of the P-S bonds v_1 in $[PS_4]^{3-}$ unit. Other vibrations in the ranges of 150-300 cm^{-1} (v_2 and v_4) and 500-600 cm^{-1} (v_3) in the Raman spectrum of β-Li_3PS_4 are narrowed and shifted to a lower wavenumber after annealing. In the spectra of heterogeneous oxysulfides, these vibrations are broadened and shifted back after mechanical milling, in good agreement with the spectrum of amorphous Li_3PS_4. In addition to the vibrations of $[PS_4]^{3-}$ units, a small peak at 942 cm^{-1} can be observed in the spectra of our oxysulfide mixtures. This vibration is attributed to the symmetrical stretching vibration of the P-O bonds v_1 in $[PO_4]^{3-}$ from the crystalline β-Li_3PO_4. The shoulder peak with a slightly higher wavenumber than the former one can be also assigned to the

symmetrical stretching vibration v_1 $[PO_4]^{3-}$ units from the milled amorphous Li_3PO_4, which confirms our assignment in MAS NMR spectra. The peak broadening and shift may arise from the amorphization process of β-Li_3PO_4 by mechanical milling (*184*, *185*). No obvious vibrations of $[PO_4]^{3-}$ are detected for the sample with x = 10 due to the limited amount of Li_3PO_4. Furthermore, the large difference in Raman scattering cross-sections between O and S hampers the analysis of $[PO_4]^{3-}$ units. As expected, the peak intensity of v_1 in $[PO_4]^{3-}$ for β-Li_3PO_4 increases when more β-Li_3PO_4 is added to the mixtures (100-x)Li_3PS_4-xLi_3PO_4. The results of Raman spectroscopy again prove the formation of (100-x)Li_3PS_4-xLi_3PO_4 from the starting materials of β-Li_3PS_4 and β-Li_3PO_4.

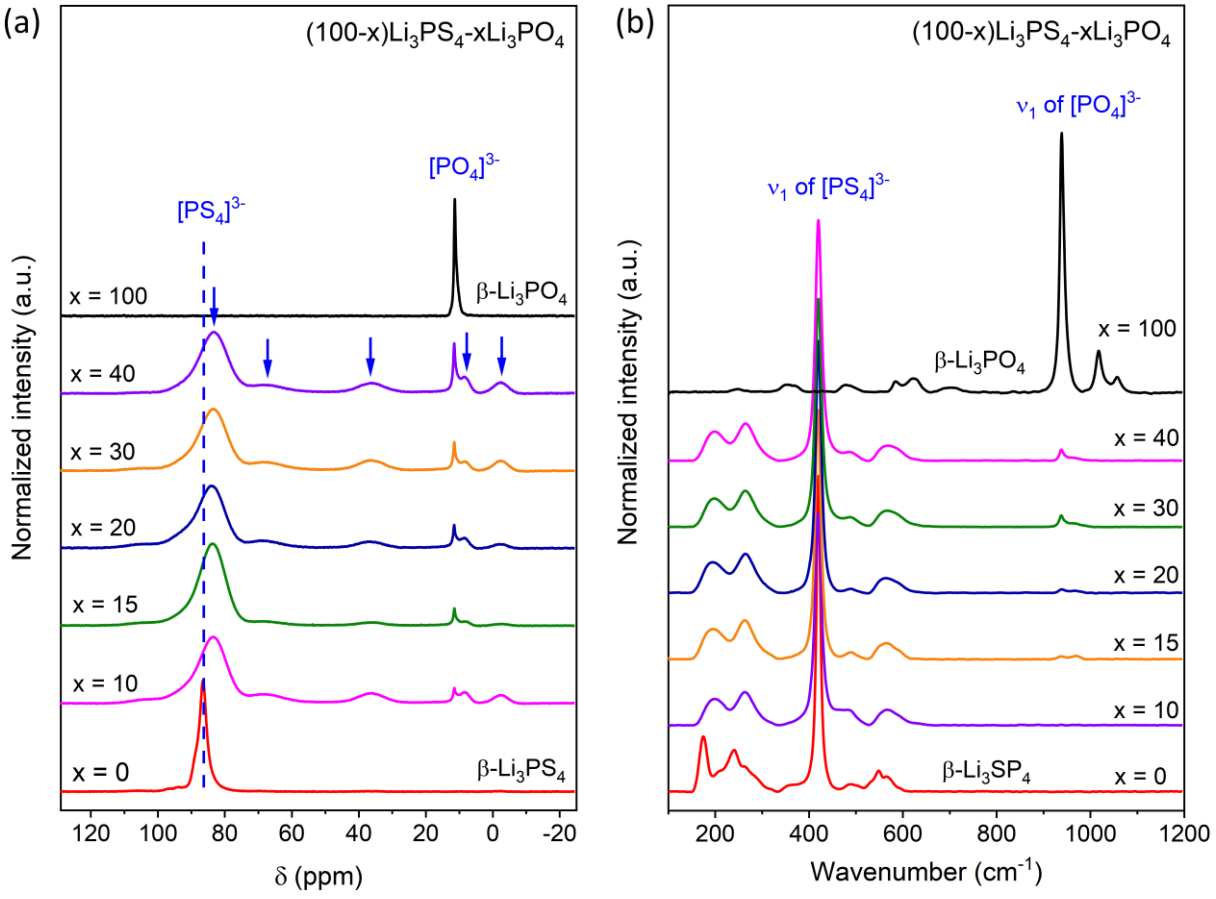

Figure 4.4: ^{31}P MAS NMR spectra (a) and Raman spectra (b) of starting materials of β-Li_3PO_4 and β-Li_3PS_4, and the evolution of heterogeneous oxysulfides (100-x)Li_3PS_4-xLi_3PO_4 ($10 \leq x \leq 40$).

4.3.2 Chemical analysis

XPS measurements were carried out on Li_3PO_4, Li_3PS_4, and the heterogeneous oxysulfides to obtain chemical information about the surface regions. Figure 4.5 (a) shows the XPS wide-scan surveys of both starting materials and the milled oxysulfide mixtures. All S-containing spectra are normalized with respect to the intensity of S 2p and all the characteristic peaks are marked with light blue or red bars. As expected, photoelectrons of Li 1s, P 2p, P 2s, and O 1s with binding energies at around 55 eV, 132 eV, 189 eV, and 530 eV, respectively, are detected in all of our samples. S 2p and S 2s peaks at binding energies of 162 eV and 226 eV, respectively, are found in pure Li_3PS_4 and all (100-x)Li_3PS_4-xLi_3PO_4 powders. The O 1s signal at a binding energy of about 530 eV in the sample of Li_3PS_4 originates from organic contaminations on the surface. While for the other Li_3PO_4-containing samples, the O 1s photoelectrons arise from both the oxygen in Li_3PO_4 and organic contaminations. The C 1s peak at a binding energy around 285 eV was observed in all powders resulting from the carbonaceous contamination. Since the contents of oxygen and carbon contaminations vary from sample to sample, a direct quantitative comparison by peak intensity is not possible from these survey spectra.

In order to quantify the Li_3PO_4, high-resolution P 2p spectra (marked in red in Figure 4.5 (a)) were collected from starting materials and all heterogeneous mixtures, as can be seen in Figure 4.5 (b). P 2p XPS spectra of both Li_3PS_4 and Li_3PO_4 are fitted with a single doublet at a binding energy of the main peak (P $2p_{3/2}$) of 132.3 eV and 133.3 eV assigned to $[PS_4]^{3-}$ and $[PO_4]^{3-}$, respectively (*186–188*). This suggests that only the pure oxide and sulfide environment exists around P in the starting materials Li_3PO_4 and Li_3PS_4, respectively. P 2p spectra of the heterogeneous oxysulfides (100-x)Li_3PS_4-xLi_3PO_4 are deconvoluted into two doublets: $[PO_4]^{3-}$ at higher binding energy (filled in orange) and $[PS_4]^{3-}$ at lower binding energy (filled in green). As expected, the peak intensity of $[PO_4]^{3-}$ increases with the increasing content of Li_3PO_4. Based on XPS P 2p spectra, molar fractions of $[PO_4]^{3-}$ for all milled mixtures are calculated and presented in Figure 4.6. The values of the molar fractions are very close to the desired values except for the sample with x = 10. The excess $[PO_4]^{3-}$ in this sample may arise from surface oxidation.

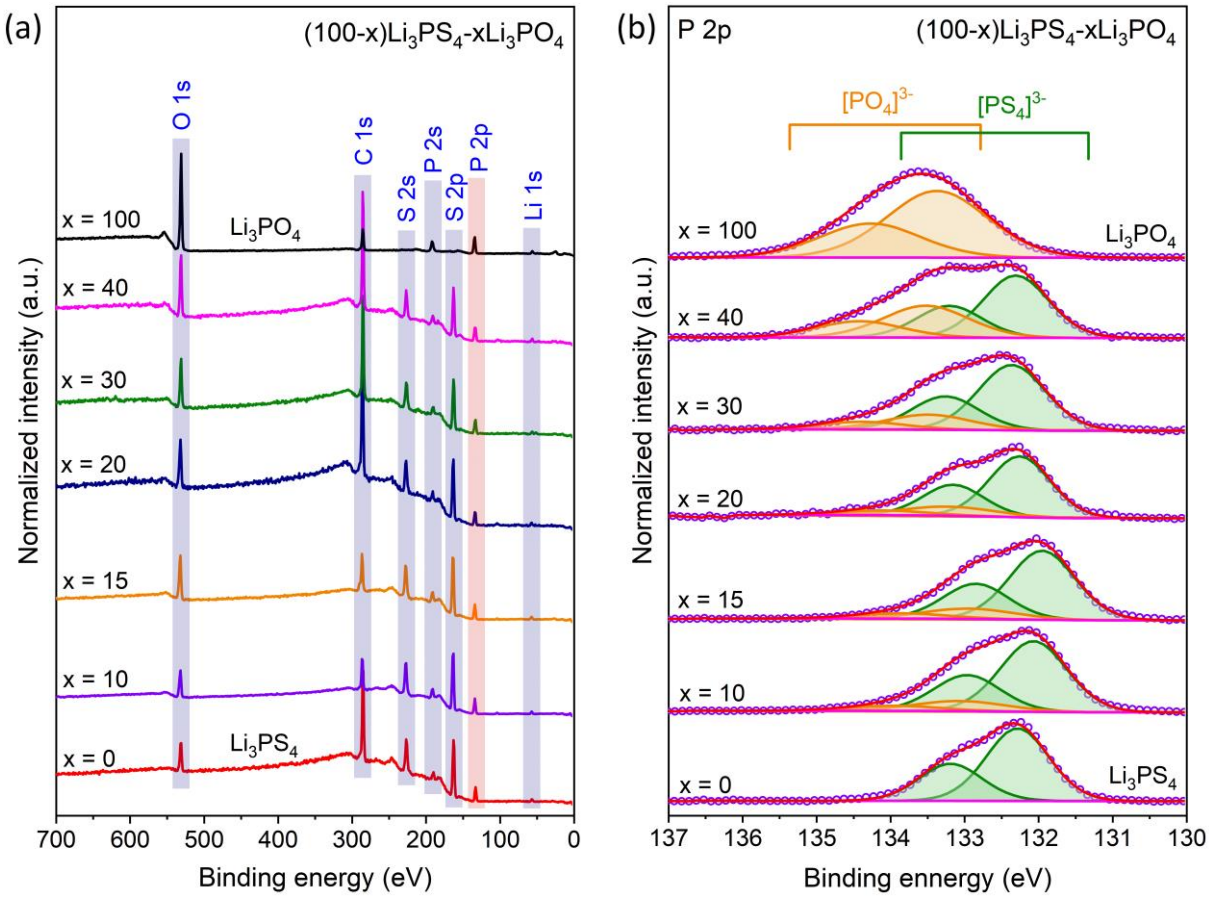

Figure 4.5: XPS survey spectra (a) and high-resolution P 2p spectra (b) of starting materials of Li_3PO_4, Li_3PS_4, and heterogeneous mixtures $(100\text{-}x)Li_3PS_4\text{-}xLi_3PO_4$ ($10 \leq x \leq 40$) after mechanical milling.

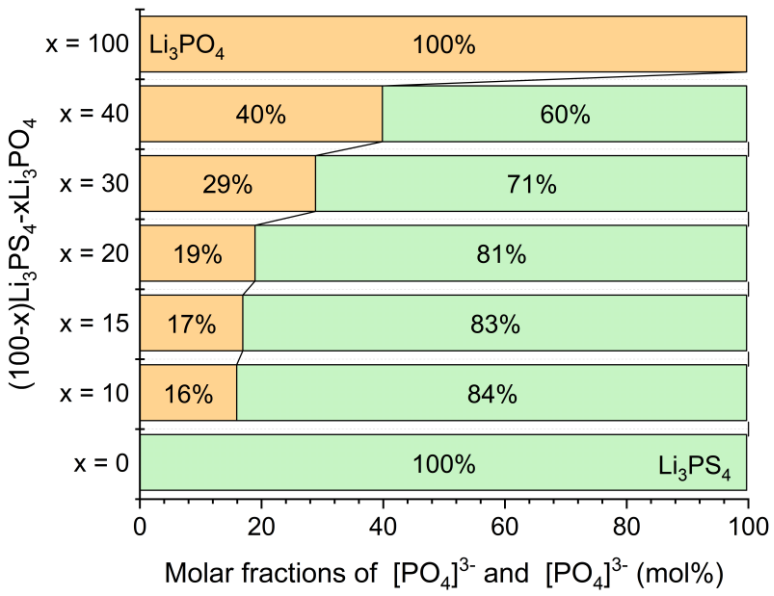

Figure 4.6: Molar fractions of $[PO_4]^{3-}$ (in orange) and $[PS_4]^{3-}$ (in green) for Li_3PO_4, Li_3PS_4, and $(100\text{-}x)Li_3PS_4\text{-}xLi_3PO_4$ based on XPS P 2p spectra.

Figure 4.7 (a) and (b) show SEM and EDX results of samples with x = 15 and x = 20 to gather morphological information and identify the elemental distribution. SEM images show that particles in both heterogeneous samples share a size range of 1-5 µm. In P and S EDX mappings, both elements are homogeneously distributed and most particle boundaries are not visible in P and S due to their strong signals. Oxygen is found to be homogeneously doped in both samples and the clear boundaries suggest that O is the minor doping element in both mixtures.

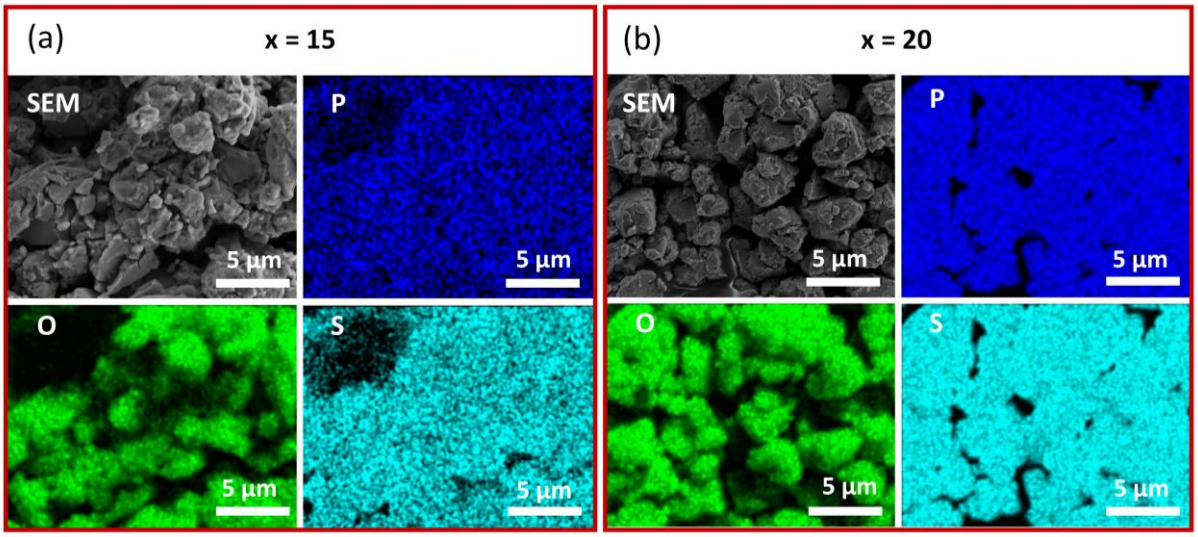

Figure 4.7: SEM images and EDX mappings for x = 15 (a) and x = 20 (b) for (100-x)Li_3PS_4-xLi_3PO_4.

4.3.3 Ionic conductivity and stability vs. Li metal

The exemplary time-resolved EIS spectra in the frequency range of 1 MHz - 500 mHz were collected from symmetric Li/(100-x)Li_3PS_4-xLi_3PO_4/Li cells with x = 20 and 15, respectively, to investigate the interface between Li and oxysulfides and its impact on ionic conductivity. Figure 4.8 (a) and (b) show the Nyquist plots of both samples with different storage times at 15 °C. 0 h stands for the spectra collected right after the assembly (less than 1 min). The deviation of the data points with a frequency higher than 400 kHz in all spectra may result from the experimental setup. Insufficient information in the high-frequency region is a general problem for fast ionic conductors. The semicircle in the frequency range of 400 kHz - 500 Hz is related to the highly overlapping semicircles for bulk electrolytes and the interface between lithium metal and SEs. Therefore, it is hard to resolve interface and bulk contributions by fitting

these spectra. The semicircular tail in the low-frequency region (< 500 Hz) can be related to the diffusion of Li^+ ions (*189*).

In Figure 4.8 (a) and (b), both freshly contacted samples exhibit a resistance of around 1200 Ω arising from both electrolyte and Li/SE interface. After 2h rest, the resistances increase to around 1700 Ω for x = 15 and around 1450 Ω for x = 20. This increase of resistance could be assigned to the formation of a interphase due to the decomposition of sulfide electrolyte in contact with lithium metal (*190*, *191*). The EIS spectra were recorded after storage for 4 h, 8 h, and 16 h, respectively, and they are very similar to the spectra obtained after 2 h resting. This suggests that a stabilized solid electrolyte interphase (SEI) is formed in both samples 2 h after contacting with Li. A lot of experimental and computational literature showed that Li_2S is formed at the interface when sulfide SEs come in contact with Li metal (*191–195*). Li_2S has poor electronic and ionic conductivity and will result in a self-limiting SEI serving as a stable interface (*196*). This could be also the origin of the increased resistance of our Li symmetric cells with heterogeneous oxysulfides A similar phenomenon was also found in time-dependent EIS spectra of milled Li_3PS_4 (x = 0), see Figure A 2.

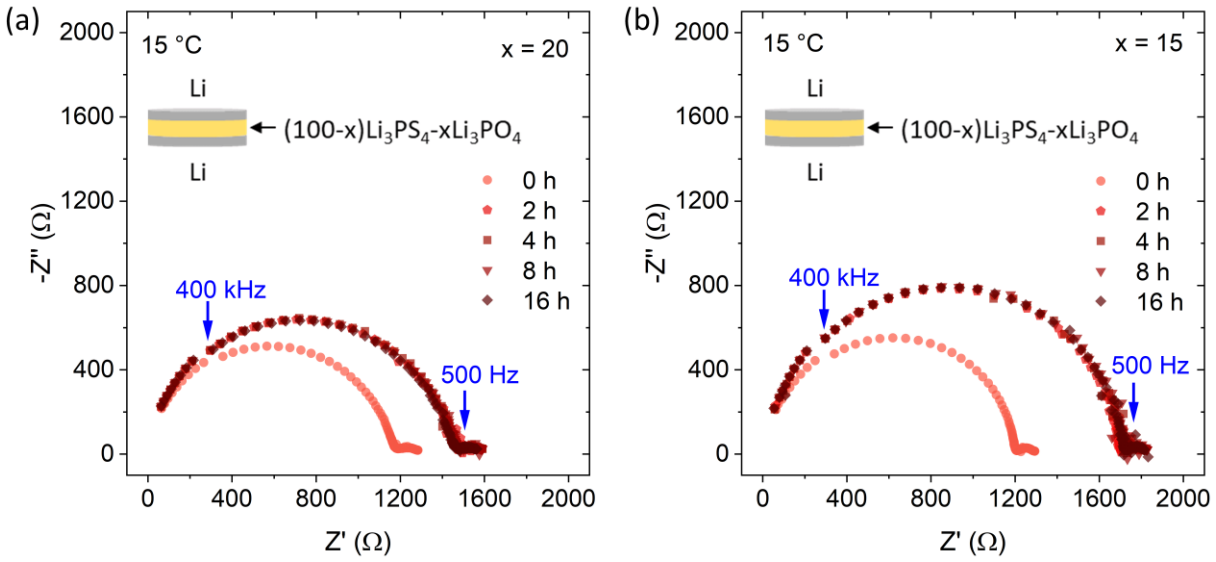

Figure 4.8: Evolution of the impedance response of symmetric Li/(100-x)Li_3PS_4-xLi_3PO_4/Li cells with x = 20 (a) and x = 15 (b) at 15 °C as a function of time. The schematic of the symmetric cell setup is shown in the inset.

EIS measurements in the temperature range of 5-75 °C were carried out to study the kinetic behavior of Li^+ ions transport. To stabilize the interphase, symmetric (100-x)Li_3PS_4-xLi_3PO_4 cells

were assembled and then stored overnight in an argon-filled glovebox. Figure 4.9 (a) shows the Nyquist plots of samples with x = 20, x = 15, and x = 0 (milled Li_3PS_4) in the frequency range of 1 MHz - 500 mHz at RT. The intercept on the x-axis (real part) at the end of the semicircle (at about 500 Hz) is the sum of electrolyte resistance and Li/SE interface resistance. In this way, the RT resistances of heterogeneous oxysulfides x = 20 and x = 15 share a close value of about 900 Ω, which is lower than that of glass thiophosphate Li_3PS_4 of 1150 Ω. Based on Equation 3.12, the RT ionic conductivities of symmetric cells with heterogeneous oxysulfides of x = 20 and 15 are 1.6 x 10^{-4} S/cm. This value is higher than that of milled amorphous Li_3PS_4 (x = 0) with 1.2 x 10^{-4} S/cm. In other words, the RT ionic conductivity of milled Li_3PS_4 is enhanced by heterogeneous doping with 15 or 20 mol % of Li_3PO_4. It is noteworthy that both interface and bulk resistances are counted for the calculation of ionic conductivity. The RT ionic conductivities in our symmetric cells are comparable to the reported values of oxysulfides based on bulk electrolyte resistance in previous papers.[137–151] The Nyquist plots in the temperature range from 5 °C to 75 °C for x = 20 and x = 15 are presented in Figure A 3 and Figure A 4, respectively.

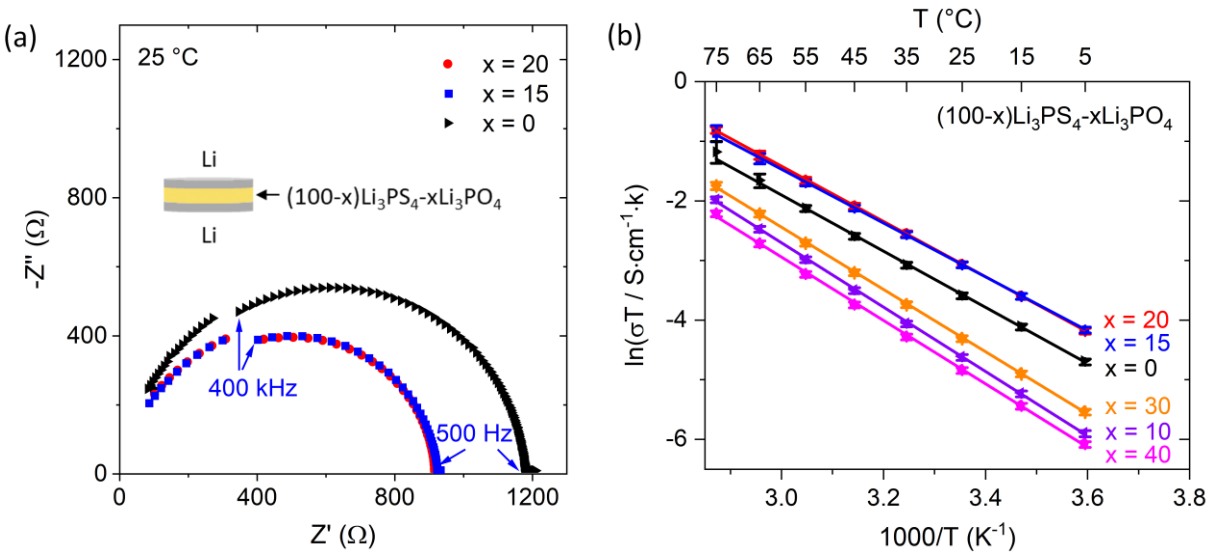

Figure 4.9: (a) Nyquist plots of symmetric Li/(100-x)Li_3PS_4-xLi_3PO_4/Li cells (x = 20, x = 15, and 0) at RT; inset shows the symmetric cell setup; (b) Temperature dependence of ionic conductivities for (100-x)Li_3PS_4-xLi_3PO_4 (0 ≤ x ≤ 40) after mechanical milling in symmetric cells from 5 °C to 75 °C.

The temperature dependence of ionic conductivities on the heterogeneous composites (100-x)Li_3PS_4-xLi_3PO_4 ($0 \leq x \leq 40$) in Li symmetric cells is shown in Figure 4.9 (b). The conductivities of all samples, derived from the resistances of both bulk electrolyte and interface, obey the Arrhenius equation (see Equation 2.16). The samples with x = 20 and x = 15 exhibit higher conductivity than the pure milled Li_3PS_4, while the other oxysulfides with x = 40, 30, and 10 have lower conductivities. The activation energies of all oxysulfides are calculated from the slope of the lines based on Equation 2.17, as summarized in Table 4.1. The lowest activation energy is observed for x = 15 and 20 with around 0.39 eV corresponding to the highest conductivity. All the other oxysulfide glass-ceramics exhibit activation energies higher than the 0.42 eV of mechanically milled Li_3PS_4. These activation energies concerning both bulk conductivity and interface conductivity are comparable to the pure bulk conductivity values of reported Li_3PO_4 doped heterogeneous oxysulfides (*148*, *149*). One possible reason for the enhancement of ionic conductivity for heterogeneous oxysulfides with x = 20 and x = 15 is the space charge effect, leading to the redistribution of charge carriers and defect formation at the heterointerface between Li_3PO_4 and Li_3PS_4 particles (*33*, *145*, *147*, *203–205*). Furthermore, the substitution of a sulfur atom by an oxygen atom forming $[PS_3O]^{3-}$, $[PS_2O_2]^{3-}$, and $[PSO_3]^{3-}$ units observed in ^{31}P MAS NMR could be another origin for this enhancement (*99*, *200*). On the other hand, the non-bridging oxygen atoms in $[PO_4]^{3-}$ are the strong trap of Li^+ ions impeding the ionic conduction (blocking effect) (*153*, *200*, *204–207*). Consequently, the highest conductivity and lowest activation energy are observed at substitution amounts of 15 and 20 mol % Li_3PO_4.

Table 4.1: Activation energies of (100-x)Li_3PS_4-xLi_3PO_4 in symmetric Li cells for ionic conduction.

x (mol %)	40	30	20	15	10	0
E_a (eV)*	0.46	0.45	0.40	0.39	0.47	0.42

*The Error of activation energy is less than 0.01 eV for all samples.

The long-term compatibility with lithium metal and ionic conductivity of heterogeneous oxysulfides were further investigated by voltage profiles of symmetric Li/(100-x)Li_3PS_4-xLi_3PO_4/Li (x = 20, 15, and 0) cells at a current density of 100 μA/cm^2, as presented in Figure 4.10. The positive and negative voltage corresponds to Li stripping and Li plating, respectively. During the first several hours, the potentials of all three samples are decreasing until they reach their constant currents. In this period, a “wetting reaction” occurred at the fresh

interface between electrolyte and lithium by Li stripping and plating to form stable SEI and good physical contact. Galvanostatic plating-stripping cycles are stable in the following 100 h with constant voltage plateaus for all three samples which demonstrates the formation of a stable interface and its long-term electrochemical stability against lithium metal.

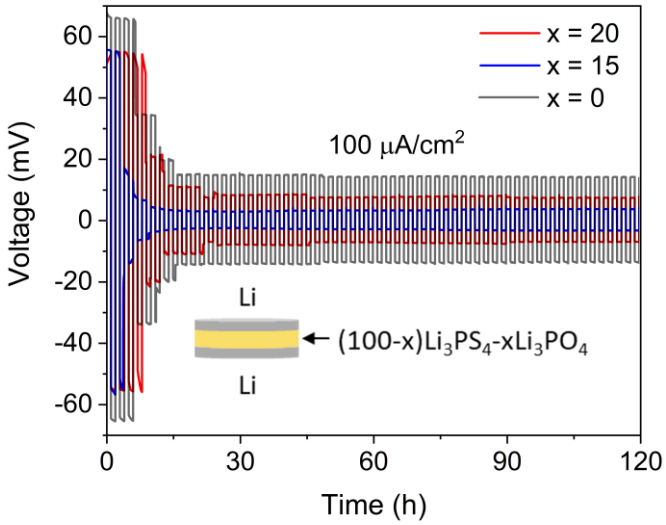

Figure 4.10: Voltage-time profiles of the Li symmetric cells Li/(100-x)Li_3PS_4-xLi_3PO_4/Li (x = 20, 15, and 0) at a current density of 100 μA/cm^2 with 1 h time interval at RT.

The direct-current (DC) conductivities of the symmetric cells could be calculated by the combination of Equation 3.12 and Ohm's law:

$$\sigma = Id/UA \qquad \text{Equation 4.1}$$

where σ (S/cm) refers to the conductivity, I (A) refers to the current, d (cm) refers to the thickness of the electrolyte pellet, R (Ω) refers to the impedance, and A (cm^2) refers to the cross-sectional area of the electrolyte pellet. DC ionic conductivities based on the voltage plateaus before the 'wetting reaction' for symmetric cells with glass-ceramics with x = 20 and x = 15 are similar with 1.4 x 10^{-4} S/cm and higher than that of glass Li_3PS_4 with 1.1 x 10^{-4} S/cm. These values are close to the corresponding alternating current (AC) conductivities obtained from impedance spectra at RT, indicating that the electrical contribution could be neglected. After several cycles of Li stripping and plating, the direct current (DC) conductivities improved to 2.4 x 10^{-3} S/cm and 9.5 x 10^{-4} S/cm for x = 20 and x =15, respectively, still higher than the DC conductivity of amorphous Li_3PS_4 with 5.1 x 10^{-4} S/cm. This large enhancement of ionic conductivity can be attributed to the highly conducting SEI and a more favorable physical contact formed after several cycles of Li plating and stripping. It is noted that the ionic

conductivities of both symmetric cells with oxysulfide glass-ceramics are enhanced by heterogeneous doping of Li_3PO_4 compared with pure glass Li_3PS_4, which agrees with the results obtained by EIS spectra.

4.3.4 Electrochemical performance

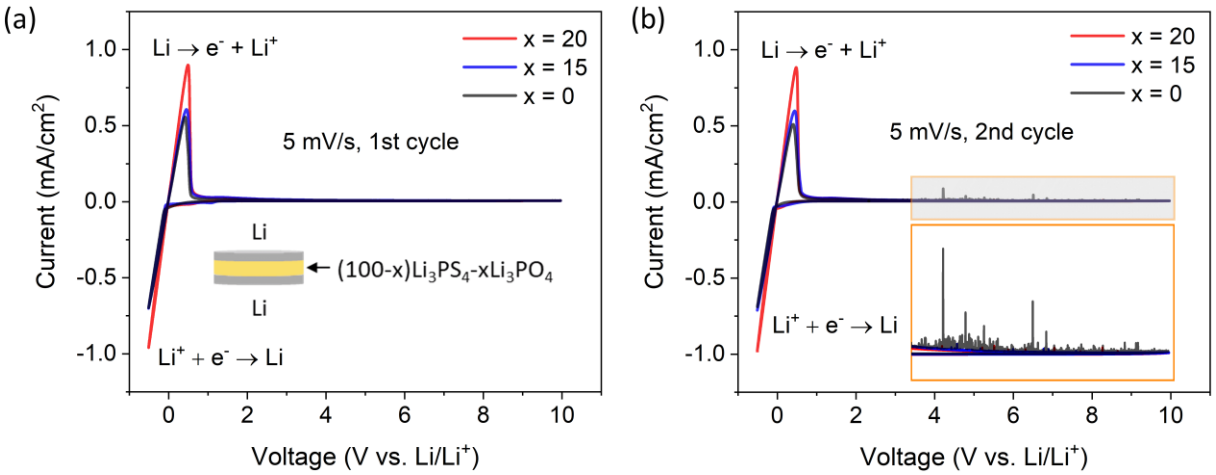

Figure 4.11: CV curves for the symmetric Li/(100-x)Li_3PS_4-xLi_3PO_4/Li cells (x = 20, x = 15, and x = 0) in the potential range from -0.5 V to 10 V (vs. Li/Li^+) at a scanning rate of 5mV/s at the first cycle (a) and the second cycle insetted with enlarged CV curves at the high voltage part (b).

Cyclic voltammetry (CV) was carried out on the symmetric Li/(100-x)Li_3PS_4-xLi_3PO_4/Li cells (x = 0, x = 0.15, and 0.20) to investigate the electrochemical stability window of our glass-ceramic oxysulfides. At the first CV cycle, as displayed in Figure 4.11 (a), a cathodic current peak at around -0.5 V (vs. Li/Li^+) refers to the deposition reaction of metallic lithium, and the other anodic current peak at around 0.5 V (vs. Li/Li^+) results from the dissolution reaction of metallic lithium (*53*). No additional peaks are observed in the voltage range from -0.5 V to 10 V (vs. Li/Li^+) for all three cells. Figure 4.11 (b) represents the CV curves of the second cycle for all three samples. Two dominant peaks for lithium deposition and dissolution are identical to those in the first cycle. Still, at high voltages over 4 V (vs. Li/Li^+), the CV curve for the sample x = 0 is strongly fluctuating suggesting the instability of the interface due to side reactions. No obvious additional peak is found for the symmetric cells with compositions of x = 15 and x = 20, which means both electrolytes have a wide electrochemical window. This indicates that the introduction of Li_3PO_4 improves the electrochemical stability of the heterogeneous oxysulfides against lithium metal. Wang et al. suggest that the enhancement of

electrochemical stability by doping with oxygen results from the stronger bonding strength between the oxygen and Li than that of sulfur and Li which in turn can modify the energy landscape for Li diffusion (*208*, *209*). According to the peak strength in the CV curves, we can again confirm that both samples, x = 20 and x = 15, exhibit higher ionic conductivity than pure Li_3PS_4.

All-solid-state batteries (ASSBs) Li-In/(100-x)Li_3PS_4-xLi_3PO_4/$LiCoO_2$ were assembled with heterogeneous oxysulfides with the compositions of x = 20, x = 15, and x = 0 (pure Li_3PS_4) to study their electrochemical performance. The scheme of the ASSB is presented as an inset in Figure 4.12 (b). Figure 4.12 (a) shows the first (dark color) and tenth (light color) charge-discharge curves for the ASSBs with three different electrolytes with x = 20, 15, and 0. The initial charge capacities of the cells with x = 20 and x =15 are 224 mAh/g and 216 mAh/g, respectively, and correspondingly the first discharge capacities are 165 mAh/g and 160 mAh/g. Both heterogeneously doped glass-ceramics exhibit higher charge and discharge capacities than pure Li_3PS_4 of 215 mAh/g and 154 mAh/g, respectively. At the tenth cycle, cells with oxysulfides with x = 20 and x = 15 share similar charge and discharge capacities of around 115 mAh/g and 113 mAh/g, respectively, while those of pure Li_3PS_4 are at 105 mAh/g 102 mAh/g, respectively. The enlarged capacity difference between the cells with oxysulfide electrolytes and pure Li_3PS_4 without oxygen dopant reveals increased cycling stability by partial substitution of Li_3PS_4 with Li_3PO_4. A clearer tendency can be seen from the long-term cycling performance of Li-In/(100-x)Li_3PS_4-xLi_3PO_4/$LiCoO_2$ (x = 20, x = 15, and x = 0) in Figure 4.12 (b). During the whole galvanostatic cycling, ASSBs with oxysulfide electrolytes with x = 20 and x = 15 have a similar discharge capacity which is higher than the cell with pure Li_3PS_4. After 60 charge and discharge cycles, cells with x = 20 and x = 15 show a discharge capacity of around 80 mAh/g, while 69 mAh/g is obtained for the cell without oxygen dopant. The Coulombic efficiency of the first cycle for these three cells with x = 20, x = 15, x = 0 are 76 %, 71 %, and 71 %, respectively. After several charge-discharge cycles, these values increase to 99 %, 99 %, and 97 %, and are maintained up to the 60^{th} cycle. These results suggest that the heterogeneous addition of Li_3PO_4 to some extend improves the cycling performance of pure Li_3PS_4 in ASSB.

However, there is still a large capacity loss for all cells at the initial cycles, which is a common phenomenon in many studies of sulfide SEs (*210*–*213*). One possible reason for this rapid decrease of capacity is the undesired side reactions between the sulfide SE and oxide positive electrode $LiCoO_2$ forming an unstable interface with increased interfacial resistance (*192*, *214*). It has been reported that cobalt and lithium phosphates, sulfates, and sulfides are formed at the interface when the sulfide electrolytes are in contact with delithiated $LiCoO_2$, and some of these compounds are electronically conductive leading to the continuous growth of the SEI (*192*, *215*, *216*). Another possible reason is the contact loss due to the depletion of lithium in the sulfide electrolyte near $LiCoO_2$ during delithiation (*217*–*219*). Furthermore, the diffusion of Co into sulfide electrolyte could also lead to large interfacial resistance and capacity decrease (*220*, *221*).

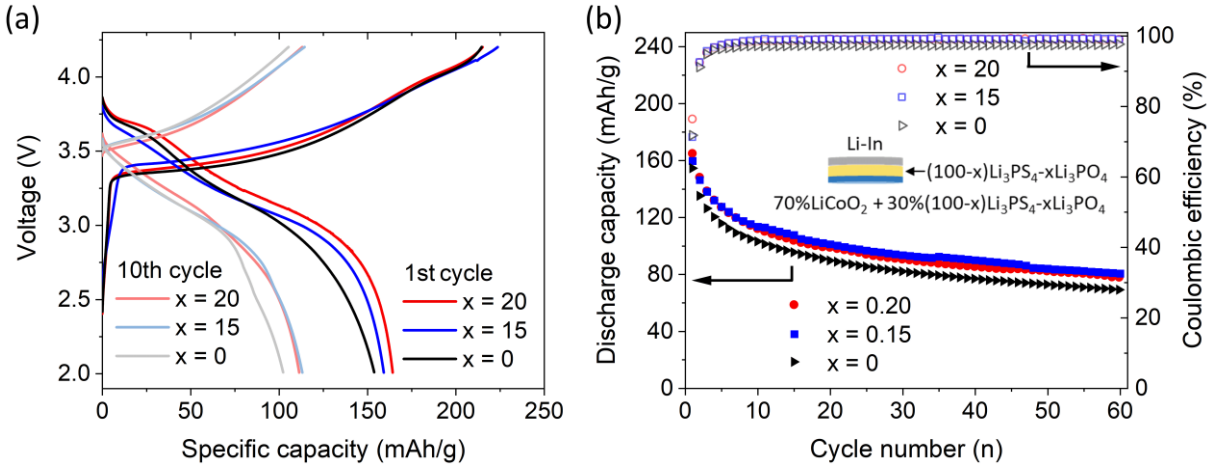

Figure 4.12: (a) Charge-discharge curves of the ASSBs Li-In/(100-x)Li_3PS_4-xLi_3PO_4/$LiCoO_2$ (x = 20, x = 15, and x = 0) in the 1st (dark color) and 10th (light color) cycle at RT; (b) galvanostatic cycling performances of the ASSBs Li-In/(100-x)Li_3PS_4-xLi_3PO_4/$LiCoO_2$ (x = 20, x = 15, and x = 0) at a rate of C/10 at 25 °C. The schematic of ASSB is displayed in the inset.

To investigate the origin of the capacity loss, EIS measurements were performed on ASSBs with SE of x = 20, x = 15, and x = 0 after long-term cycling (more than 60 cycles). The data were collected in the frequency range of 1 MHz - 10 mHz at 15 °C as shown in Figure 4.13 (a). The small semicircle in the high-frequency region is ascribed to the bulk resistance of SE and interfacial resistance of Li-In/SE, while the depressed semicircle in the low-frequency region corresponds to the overlap of charge transfer resistance and interfacial resistance of SE/$LiCoO_2$ (*147*, *222*, *223*). According to the intercept on the x-axis in the medium-frequency

range, the sums of bulk resistance of SE and interfacial resistance of Li-In/SE for the ASSBs with x = 20, x = 15, and x = 0 after long cycling are around 1750 Ω, 1550 Ω, and 2700 Ω, respectively. Surprisingly, these values are close to those for corresponding Li symmetric cells with 1700 Ω, 1450 Ω, and 2520 Ω. This indicates that the interphase between Li-In and our SE in ASSBs is extremely stable after over 60 cycles. Additionally, the resistance originating from the positive electrode (interface resistance and charge transfer resistance) in the high-frequency region is 7-8 times higher than the sum of SE resistance and Li-In/SE resistance in the low-frequency region. Hence, we may confirm that the capacity loss of the ASSBs mainly results from the huge resistance caused by the SE/$LiCoO_2$ interface. Comparing the impedance spectra of ASSBs with heterogeneous oxysulfide electrolytes with x = 20 and x = 15 to that of pure sulfide glass Li_3PS_4, the former ones have smaller semicircles in both high-frequency and low-frequency regions than the latter one after long-term cycling. This again proves the enhancement of electrochemical performance by introducing Li_3PO_4 dopant into the Li_3PS_4 electrolyte.

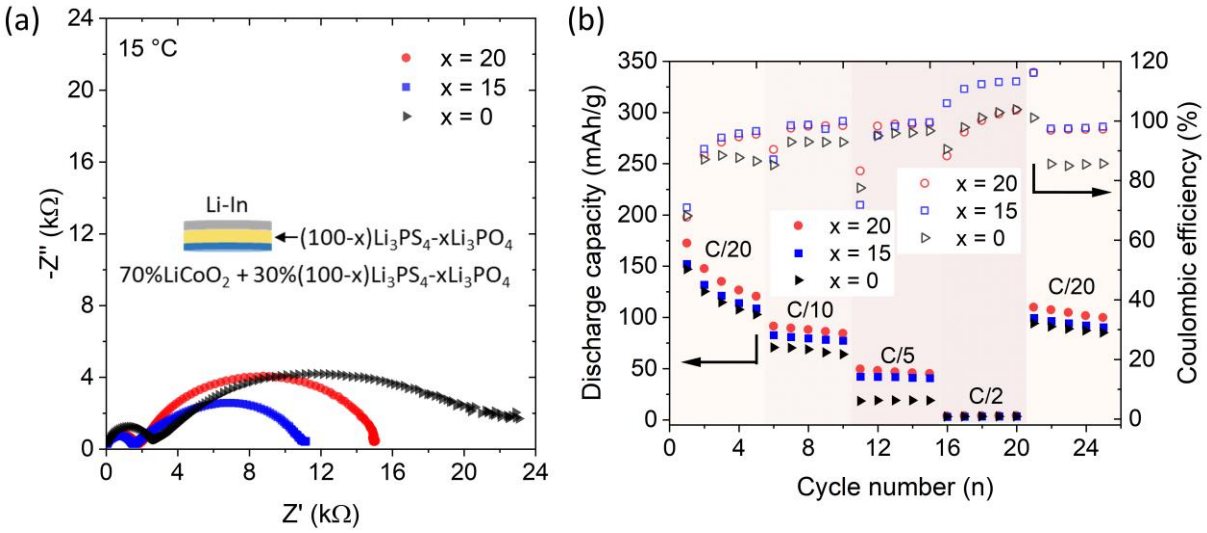

Figure 4.13: (a) EIS spectra of ASSBs with Li-In/(100-x)Li_3PS_4-xLi_3PO_4/$LiCoO_2$ (x = 20, x = 15, and x = 0) after long-term cycling with an inset of the schematic of the cells; (b) Rate capabilities of Li-In/(100-x)Li_3PS_4-xLi_3PO_4/$LiCoO_2$ (x = 20, x = 15, and x = 0) after charging and discharging at different C-rates (C/20, C/10, C/5, C/2, and again with C/20 in the end), each for 5 cycles.

Figure 4.13 (b) shows the discharge capacities and Coulombic efficiencies of ASSBs with oxysulfide electrolytes with x = 20, x = 15, and x = 0 at different cycling rates. Full cells with x =20 and x = 15 have higher discharge capacity and Coulombic efficiency than pure Li_3PS_4 at all current densities other than at C/2, demonstrating the improvement of rate performance by

oxygen dopant. Moreover, these enhancements of discharge capacity and Coulombic efficiency increase with increasing current density. The full cell with x = 20 exhibits the best rate performance with discharge capacities of 140, 88, 47, 3, and 104 mAh/g at C/20, C/10, C/5, C/2, and again with C/20, respectively. For all three cells, the capacity goes down with increasing current density, and only a very limited capacity was obtained at C/2 suggesting that all of them cannot be qualified for the request of fast charge and discharge. Values close to the initial capacities are again obtained when cycled with C/20 in the end. It is noted for all three cells that a smaller C rate leads to a stronger capacity fade. This happens as a small C rate relates to longer charge-discharge providing more time for the continuous growth of SEI at the SE/$LiCoO_2$ interface and therefore increasing interfacial resistance.

4.4 Conclusions

In this work, heterogeneous oxysulfides (100-x)Li_3PS_4-xLi_3PO_4 ($10 \leq x \leq 40$) were synthesized by two-step mechanical milling. The starting material of crystalline Li_3PS_4 was prepared by the first-step ball milling of Li_2S and P_2S_5 followed by calcination, as proved by the XRD patterns. Li_3PO_4 was synthesized by co-precipitation method and mixed with crystalline Li_3PS_4 by the second-step mechanical milling to obtain heterogeneous oxysulfides (100-x)Li_3PS_4-xLi_3PO_4. The desired compositions of the heterogeneous oxysulfides were confirmed by XPS. XRD patterns of all oxysulfide mixtures show mixed diffractions from both starting materials of Li_3PS_4 and Li_3PO_4, indicating the formation of mixed heterogeneous composites, in good agreement with the results of Raman spectroscopy and ^{31}P MAS NMR. Temperature-dependent ionic conductivity shows that symmetric cells Li/(100-x)Li_3PS_4-xLi_3PO_4/Li with compositions of x = 15 and x = 20 exhibit higher conductivity and lower activation energy than the pure milled Li_3PS_4, which is again proved by CV and galvanostatic cycling of Li symmetric cells. The space charge effect at the heterointerface of Li_3PO_4 and Li_3PS_4 is deemed to be one possible reason for this enhancement. Furthermore, oxysulfide units $[PS_3O]^{3-}$, $[PS_2O_2]^{3-}$, and $[PSO_3]^{3-}$ in the heterogeneous mixtures, which were found by ^{31}P MAS NMR, could be another possible origin for this enhancement. The conductivity of heterogeneous oxysulfides decreases when more poorly conductive Li_3PO_4 was added to the mixture, due to the increasing blocking effect. According to AC impedance data, RT conductivities of Li/80Li_3PS_4-20Li_3PO_4/Li and Li/85Li_3PS_4-15Li_3PO_4/Li concerning both interface resistance and SE bulk

resistance share a similar value of 1.6 x 10^{-4} S/cm. Interestingly, higher RT DC conductivities of 2.4 x 10^{-3} S/cm and 9.5 x 10^{-4} S/cm were obtained for these two Li symmetric cells with x = 20 and x = 15 respectively, after stabilization in the initial galvanostatic cycles. These values are higher than most Li_3PO_4 doped sulfides stated in the literature, although both bulk and interface resistance are inclusive. The contribution of electrical conduction could be negligible since the AC conductivities of both mixtures are similar to the DC conductivities before the stabilization. High interface stability between Li and the heterogeneous oxysulfides was confirmed by time-resolved EIS and Li plating and stripping measurements. Remarkably, the resistances of bulk SE and Li-In/SE interface stay almost the same after long-term cycling, which again proves the excellent stability of heterogeneous oxysulfides with x = 20 and x = 15 against Li. Furthermore, side reactions were observed at the second CV cycle of Li/Li_3PS_4/Li. These side reactions are not present in x = 20 and x = 15 revealing enhanced electrochemical stability by heterogeneous Li_3PO_4 dopant. The cycling stability and rate capability of Li-In/(100-x)Li_3PS_4-xLi_3PO_4/$LiCoO_2$ full cells with oxysulfides x = 20 and x = 15 were also improved compared with pure Li_3PS_4. However, the capacity loss during the initial charge-discharge cycles is still not eliminated by reason of the huge resistance at the interface between SE and $LiCoO_2$ after cycling. This issue should be addressed in future studies.

5 Thin-Film Solid Electrolyte LiON-Al_2O_3

This chapter focuses on the heterogeneous multilayer LiON-Al_2O_3 SE thin films. The motivation of the investigation of heterostructured LiON-Al_2O_3 ALD films is introduced in section 5.1. Section 5.2 describes the synthesis of LiON-Al_2O_3 ALD films, corresponding characterization techniques, and the set-up for impedance spectroscopy. Surface and in-depth information, and the ionic conductivity of the multilayered LiON-Al_2O_3 films are presented in section 5.3. Section 5.4 gives a conclusion of the results in this chapter.

5.1 Introduction

To power the increasing number of microdevices, the development of a miniaturized energy storage system is more and more urgent. Three-dimensional (3D) batteries with high energy density per footprint area have received great attention for their promising application in microdevices (*23*, *224*). Deposition of a conformal thin-film SE over a complex 3D structure is one of the key challenges to build a 3D battery. Owing to its cyclic and self-saturating nature, atomic layer deposition (ALD) has the capability to grow conformal and pinhole-free thin films with adjustable composition and controllable thickness on the nanoscale (*26*, *225*, *226*). These features make ALD one of the most promising techniques to fabricate 3D batteries. Moreover, ALD thin films are widely employed as electrode coatings to improve the ionic conductivity and stability (*227*, *228*).

Since the first deposition of Li-containing ALD films using five different precursors by Putkonen et al. in 2009, various ALDs films were synthesized as thin-film SEs (*229*, *230*). In order to improve the ionic conductivity of the Al_2O_3 ALD protecting layer, binary films of lithium aluminum oxide ($Li_xAl_yO_z$) were prepared by introducing a Li-rich sublayer (*30*, *130*, *231–233*). Aaltonen et al. prepared the first $Li_xAl_yO_z$ ALD films using trimethylaluminum (TMA) and ozone (O_3) as precursors for the Al_2O_3 sublayer and lithium *tert*-butoxide (LiO^tBu) and H_2O as precursors for the Li_2O sublayer (*30*). This Li_2O sublayer was later reported to be LiOH by Kozen et al. (*234*). The Li^+ ionic conductivity of their $Li_xAl_yO_z$ films obtained by extrapolation was $3x10^{-1}$ S/cm at 500 °C, $9x10^{-4}$ S/cm at 400 °C, and $1x10^{-7}$ S/cm at 300 °C. In 2014, Park et al. synthesized $Li_xAl_yO_z$ films using LiO^tBu-H_2O for the LiOH sublayer and TMA-H_2O instead of O_3

for the Al_2O_3 sublayer (*233*). These ALD films with an extrapolated RT conductivity of $1x10^{-7}$ S/cm served as a barrier layer between $LiNi_{0.5}Mn_{1.5}O_4$ and graphite electrodes to improve the electrochemical stability of LIBs. Hu et al. performed both in-plane and cross-plane impedance measurements on amorphous $Li_xAl_yO_z$ films, in which TMA-O_3 and lithium trimethyl silanolate (LiTMSO)-H_2O were used as precursors for Al-rich sublayers and Li-rich sublayers, respectively (*232*). The RT Li^+ conductivity of their $Li_xAl_yO_z$ films was in the order of 10^{-10} S/cm with an activation energy of ca. 0.8 eV.

The multilayered system with a heterostructure was proved to be able to significantly improve the ionic conductivity of a solid electrolyte (*34*, *35*). The ionic conductivity could be further enhanced by decreasing the thickness of the sublayer in the scale of the Debye length (λ_D) (*32*, *235*, *236*). In this case, space charge regions are overlapping and can provide more charge carriers for ionic conduction. However, none of the $Li_xAl_yO_z$ ALD films mentioned above show a layer-by-layer heterostructure for the enhancement of conductivity. Hence, we synthesized multilayered heterostructures based on $Li_xAl_yO_z$ with the thickness of each sublayer in the range of several nanometers with overlapping space charge regions. It is reported that the ionic conductivity of lithium phosphate oxynitride (LiPON) thin films could be improved by partial substitution of oxygen with nitrogen (*237–239*). With this in mind, radiofrequency N_2 plasma followed by purging of NH_3 was employed to dope nitrogen into the Li-rich sublayer in this work. As a result, we prepared novel heterogeneous lithium aluminum oxynitride (LiON-Al_2O_3) multilayered thin films by alternating deposition of lithium oxynitride (LiON) sublayer and Al_2O_3 sublayer via ALD. The surface and in-depth properties of these heterostructured thin films were investigated by various techniques. The Li^+ ionic conductivity of the ALD films with various thicknesses of sublayers was measured by in-plane impedance spectroscopy at different temperatures to investigate the transport mechanism of Li^+ ions in heterostructured nanolayers and the influence of the thickness of sublayers.

5.2 Experimental

5.2.1 Synthesis

The samples were prepared by Dr. Andy Fiedler in the group of Prof. Xiang Yang Kong in the Institute of Materials for Mobile Energy, Shanghai Jiao Tong University, China.

All films were deposited on SiO_2/Si substrates (300 nm SiO_2 on Si) at 200 °C using a Beneq TFS 200 apparatus. Before the deposition, all SiO_2/Si substrates were washed with 99.9 % ethanol and dried with nitrogen gas. TMA (Sigma Aldrich, 98 %) and deionized H_2O were stored at RT and alternatively introduced to the chamber to synthesize the Al_2O_3 layer. The LiON layer was grown through subsequent exposure of LiO^tBu (Sigma Aldrich, 99.9 %), N_2-fed (99.999 %) plasma with a power of 100 W, and NH_3 (5 % in argon) as the last step. The LiO^tBu precursor was maintained at 155 °C because of its solid nature at RT. Nitrogen (99.999 % N_2) was employed as a purging gas after every ALD process. Pure 600LiON film and pure 200 Al_2O_3 film were prepared using 600 ALD cycles of LiO^tBu-N_2 plasma-NH_3 and 200 ALD cycles of TMA-H_2O, respectively. Multilayered LiON-Al_2O_3 heterostructures were synthesized by combining individual sublayers of Al_2O_3 and LiON with different ALD cycles to control the thickness of each sublayer. All ALD films are listed in Table 5.1. All multilayers in Table 5.1 are labeled as (*a*LiON-*b*Al_2O_3)x*c*, where three numbers of *a*, *b*, and *c* refer to the number of ALD cycles for the LiON sublayer (*a*), the number of ALD cycles for the Al_2O_3 sublayer (*b*), and the number of bilayer repetitions (*c*).

Table 5.1: Sample list of ALD thin films.

Sample	Number of LiON subcycle per sublayer	Thickness of LiON sublayer (nm)*	Number of Al_2O_3 subcycle per sublayer	Thickness of Al_2O_3 sublayer (nm)*	Number of repetitions of both sublayers	Total thickness of the sample (nm)*
200Al_2O_3	0	0	200	20	0	20
600LiON	600	48	0	0	0	48
(20LiON-20Al_2O_3)x10	20	1.6	20	2	10	36
(20LiON-20Al_2O_3)x20	20	1.6	20	2	20	72
(40LiON-05Al_2O_3)x20	40	3.2	05	0.5	20	72
(40LiON-10Al_2O_3)x20	40	3.2	10	1	20	84
(40LiON-20Al_2O_3)x20	40	3.2	20	2	20	104
(20LiON-10Al_2O_3)x30	20	1.6	10	1	30	78
(40LiON-10Al_2O_3)x15	40	3.2	10	1	15	63
(50LiON-10Al_2O_3)x12	50	4	10	1	12	60
(75LiON-10Al_2O_3)x08	75	6	10	1	8	56

*Thicknesses of all sublayers and films were calculated from the number of subcycles with respect to the deposition rate of LiON (0.8 Å/cycle) and Al_2O_3 (1 Å/cycle), as determined from TEM results.

5.2.2 Film characterization

The surface roughness of the ALD films was characterized by a ContourGT-K scanning white light interferometer (Bruker, Germany) with a maximum vertical resolution of 0.1 nm. The morphology and elemental distribution were analyzed using a Zeiss Merlin scanning-electron microscope (ZEISS SMT AG, Germany) equipped with a 60 mm^2 XFlash EDX detector (Bruker, Germany). A grazing incidence X-ray diffractometer (GIXRD) equipped with a Cu anode tube (Rigaku SmartLab, Japan) was used to characterize the structure of our thin film with an incident angle of 2°. The scan step was 0.04° for every 40 s in the 2θ range of 15-80°.

40 ALD cycles of Al_2O_3 film followed by a carbon film was first deposited on the $(20LiON\text{-}20Al_2O_3)x10$ film to protect it from the damage of the focused ion beam (FIB). The cross-section of the specimen was then prepared using a Helios G4 FIB system (Thermo Fisher Scientific, USA) including the low-pressure polishing process at 5 keV and 2 keV. High-resolution TEM measurement was conducted on this cross-sectional sample using JEM-2100F microscopy (JEOL, Japan) operated at 200 kV. This high-resolution TEM was perfomed by Dr. Wangqiong Xu in the group of Prof. Rong Huang in the Key Laboratory of Polar Materials and Devices (MOE), East China Normal University, China;

^7Li and ^{27}Al MAS NMR spectroscopy was performed with an Avance 500 MHz spectrometer (Bruker, Germany) at a magnetic field of 11.7 T, corresponding to resonance frequencies of 194.4 MHz (^7Li) and 130.3 MHz (^{27}Al). Powder samples were obtained by grinding the Si wavers with deposited films in an argon-filled glovebox (O_2, H_2O < 0.1 ppm). Spinning was performed in 2.5 mm rotors at 30 kHz. Spectra were acquired with a rotor-synchronized Hahn-echo pulse sequence. The chemical shifts of ^7Li and ^{27}Al were referenced to aqueous solutions of 1M LiCl and 1M $Al(NO_3)_3$, respectively.

ToF-SIMS measurements were performed with a TOF.SIMS5 instrument (ION-TOF GmbH, Germany) equipped with a Bi cluster primary ion source and a nonlinear type time-of-flight analyzer. UHV base pressure was < 5×10^{-9} mbar. For depth profiling a dual-beam analysis was performed in noninterlaced mode: the primary ion source (25 keV Bi^+) with a reduced pulse of 1 ns was scanned over an area of 200 × 200 μm^2 and the sputter gun for etching was operated with Ar clusters (Ar_{1500}^+) at 20 keV scanned over a concentric field of 400 × 400 μm^2 (target

current 15.5 nA). A shallow wedge-shaped crater was made to resolve the topmost sublayers of the multilayered film. The wedge-shaped crater was eroded by applying an increasing ion fluence along a certain direction using a 2 keV Cs^+ ion beam rastered in dc mode over a 400 µm x 200 µm area. The dwell time was restricted to 2 ms during each pass. The normal crater was etched by an Ar cluster of 2.5 keV or 20 keV with a dwell time of 0.1 ms. The information of all craters was obtained by taking a ToF-SIMS image of the resulting crater region with a 500 µm x 500 µm field of view and a resolution of 256 x 256 pixels.

A (20LiON-20Al_2O_3)x20 film or a (75LiON-10Al_2O_3)x08 film was chosen as examples to perform the above-mentioned measurements. XPS measurements were conducted on all ALD films by a K-Alpha or a K-Alpha$^+$ instrument (Thermo Fisher Scientific, UK) using a micro-focused, monochromated Al Kα X-ray source with 400 µm spot size. High current monoatomic Ar^+ ions with 1 keV energy at a scan size of 2 mm x 1mm were utilized for XPS sputter depth profiling. Charge compensation was utilized to minimize the buildup of local electrical charge during the measurement. All spectra were referenced to the carbonaceous C 1s peak (C–C/C–H) at 285.0 eV binding energy on the top surface since no distinct energy shift was caused by sputtering. Details about data acquisition and analysis are explained in section 4.2.2. Angle-resolved XPS (ARXPS) measurements were performed in a modified Vacuum Generators ESCALAB Xi^+ (Thermo Scientific, UK) using a monochromated Al K_α X-ray source with an energy of 1486.6 eV and a spot size of 650 µm. The sample was rotated from 0° to 70° in a 10° increment. Charge compensation was utilized to minimize the buildup of local electrical charge during the measurement.

5.2.3 Impedance spectroscopy characterization

To ensure good electrical contact of the samples, a gold electrode was evaporated on the samples using an S2000 sputter machine (MTI, USA) in an argon-filled glovebox (MBraun, Germany). The samples were covered with a mask, see Figure A 5, and the gold evaporation was conducted with a current of 12 amperes after evacuating the system with a pressure lower than 5 mbar. Figure 5.1 (a) and (b) show an image of the sample after gold evaporation and an SEM image of the gold electrode, which suggests that a good gold contact was deposited on our ALD film. Impedance measurements were performed with a potentiostat (Solartron,

England) in an argon-filled glovebox and the setup for impedance measurements is displayed in Figure 5.1 (c). Two probe stations were employed to ensure good electrical contact and a heating stage was used to regulate the test temperature. EIS spectra were collected with an applied voltage of 200 mV in a frequency range from 1 MHz to 20 mHz in the temperature range of 120-180 °C.

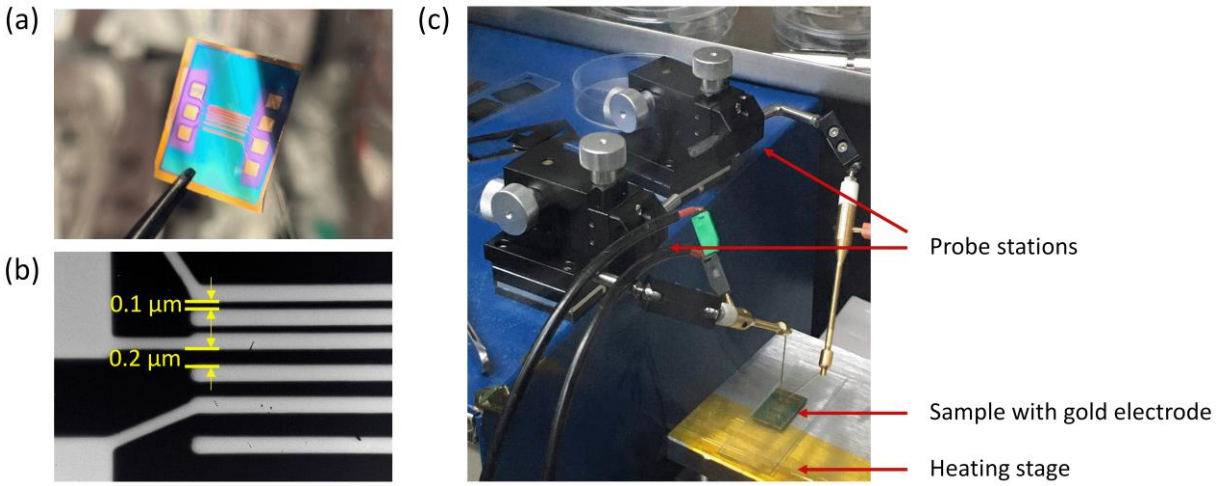

Figure 5.1: (a) Image of the sample with gold electrode; (b) SEM images of the gold electrode; (c) Setup for in-plane EIS measurements.

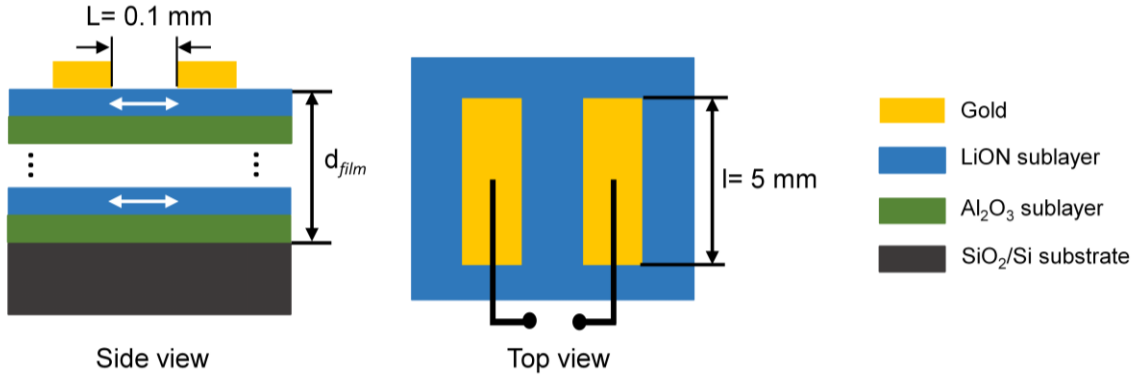

Figure 5.2: Schematic model of the setup for in-plane EIS measurements.

According to the schematic model of the setup for EIS, see Figure 5.2, the ionic conductivity can be calculated with the following equation

$$\sigma = L/[R(l \cdot d_{film})] \qquad \text{Equation 5.1}$$

where L refers to the distance between both electrodes, R refers to the ionic resistance obtained from EIS, l refers to the length of the electrode, and d_{film} refers to the thickness of the film.

5.3 Results and discussion

5.3.1 Structural and chemical analysis

The morphology was investigated by SEM and WLI to verify the flat and pinhole-free films. Figure 5.3 (a) shows the SEM image of the (20LiON-20Al_2O_3)x20 film with a magnification of 25000x. No holes can be observed from the image and the surface is extremely flat and smooth. Figure 5.3 (b) shows the 2D vertical surface roughness map of the (20LiON-20Al_2O_3)x20 film at a resolution of 0.1 nm. The roughness of the (20LiON-20Al_2O_3)x20 film is calculated to be less than 1 nm. Figure 5.3 (c) and (d) correspond to the cross-sectional profiles in the x and y-direction, respectively. The height differences between the highest point and the lowest point in both profiles are less than 4 nm. Similar SEM and WLI results were also obtained from the (75LiON-10Al_2O_3)x08 film, as displayed in Figure A 6. SEM and WLI results of both the (20LiON-20Al_2O_3)x20 film and (the 75LiON-10Al_2O_3)x08 film indicate that extremely flat, smooth, and pinhole-free multilayered LiON-Al_2O_3 heterostructures were synthesized via ALD.

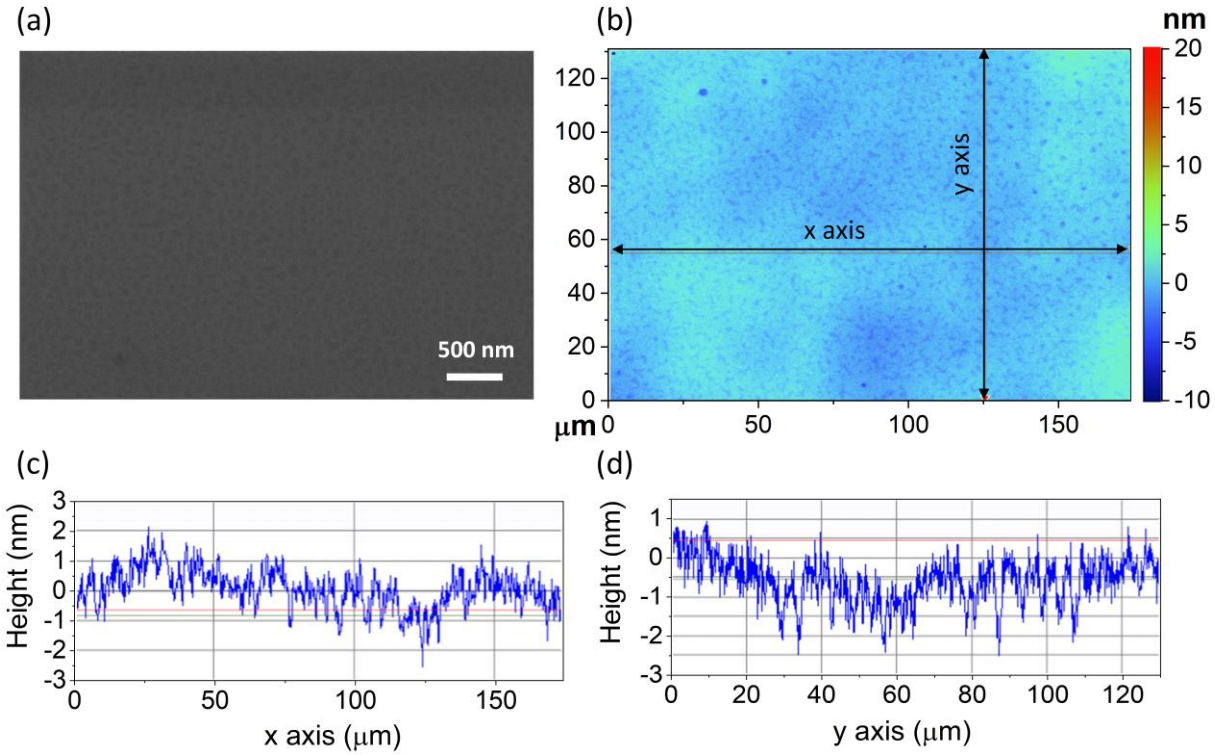

Figure 5.3: (a) SEM image of the (20LiON-20Al_2O_3)x20 film; (b) Surface map of the (20LiON-20Al_2O_3)x20 film obtained by WLI; Cross-sectional profiles of the x-axis (c) and the y-axis (d), as marked in (b).

EDX measurements were performed for both the (20LiON-20Al_2O_3)x20 film and the (75LiON-10Al_2O_3)x08 film to investigate the elemental distribution of our ALD films. The SEM image of the (20LiON-20Al_2O_3)x20 film in Figure 5.4 (a) again shows that the ALD film is very flat and homogeneous. EDX mappings of C, N, O, Al, Si in Figure 5.4 (a) demonstrate that all the elements are homogeneously distributed in the (20LiON-20Al_2O_3)x20 film. Figure 5.4 (b) is the corresponding EDX spectrum. The peaks of C, N, O, Al, Si were detected on the film, whereas other elements were not observed in the EDX spectrum. Li can not be detected due to the limitation of this technique. The detected Si signal stems from the SiO_2/Si substrate since the film's thickness is around 70 nm according to the TEM results in Figure 5.8 while the sampling depth of EDX reaches 1-2 µm. In the same way, a certain amount of oxygen also arises from the substrate. EDX measurements of the (75LiON-10Al_2O_3)x08 film in Figure A 7 show similar results while having a stronger Si peak compared with the (20LiON-20Al_2O_3)x20 film. Since the (75LiON-10Al_2O_3)x08 film is thinner than the (20LiON-20Al_2O_3)x20 film, it contains stronger signals from the substrate. Hence, carbon is the only contamination detected by EDX in our ALD films, which might originate from the carbonaceous contamination on the surface and residual carbon from the precursors after the purge process.

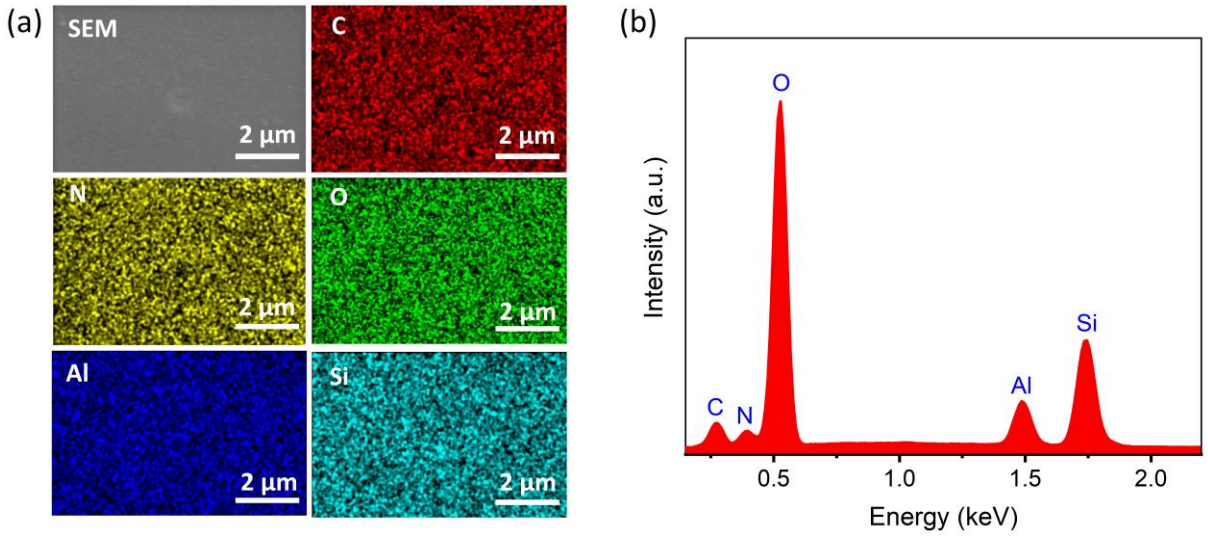

Figure 5.4: (a) SEM image and corresponding EDX mappings (C, N, O, Al, Si) of (20LiON-20Al_2O_3)x20 film; (b) EDX spectrum of the (20LiON-20Al_2O_3)x20 film.

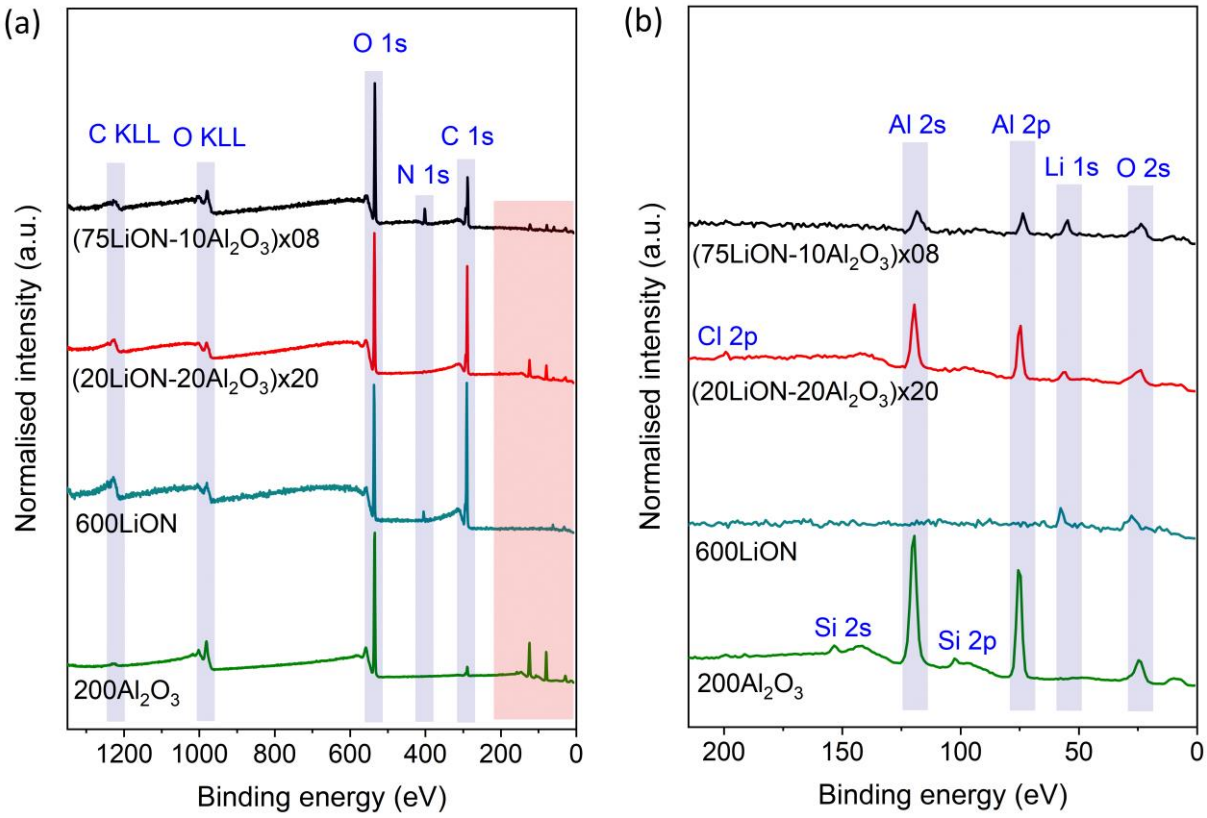

Figure 5.5: (a) XPS survey spectra collected on the surface of the $200Al_2O_3$ film, the 600LiON film, the $(20LiON\text{-}20Al_2O_3)x20$ film, and the $(75LiON\text{-}10Al_2O_3)x08$ film; (b) Enlarged XPS survey spectra corresponding to the red area in (a).

XPS measurements were conducted on the ALD films to obtain the chemical information on the surface of the films. Figure 5.5 (a) shows wide-scan survey spectra in the binding energy range of 0-1350 eV for a $200Al_2O_3$ film, a 600LiON film, a multilayered $(20LiON\text{-}20Al_2O_3)x20$ film, and a multilayered $(75LiON\text{-}10Al_2O_3)x08$ film. All spectra were normalized with respect to the peak intensity of O 1s and all characteristic peaks were marked with light blue bars. To resolve the signals at low binding energy, enlarged spectra in the binding energy range of 0-215 eV are displayed in Figure 5.5 (b). Since the sampling depth of XPS (5-10 nm) is higher than the thicknesses of both the LiON sublayer and the Al_2O_3 sublayer of the $(20LiON\text{-}20Al_2O_3)x20$ film and the $(75LiON\text{-}10Al_2O_3)x08$ film, photoelectrons from both sublayers were detected during the measurement. The survey spectra of all films contain photoelectrons of O 2s at around 23 eV, C 1s at around 285 eV, O 1s at around 531 eV, and corresponding Auger electrons of O KLL at around 975 eV and C KLL at around 1230 eV. The strong signal of carbon originates from surface contamination, which is anticipated for this surface-sensitive

technique. As expected, Li 1s at 55 eV is observed in all Li-containing films rather than in the 200Al_2O_3 film. By contrast, Al 2p at 74 eV and Al 2s at 119 eV are detected in all Al-containing films, not in 600LiON film. A distinct peak at around 400 eV for N 1s can be seen from the survey spectra of both films of 600LiON and (75LiON-10Al_2O_3)x08, while less intensity is observed for the (20LiON-20Al_2O_3)x20 film owing to fewer LiON sublayers. This proves that nitrogen was added to the ALD films by N_2 plasma and NH_3 gas. There is a weak peak at 199 eV for the (20LiON-20Al_2O_3)x20 film, which is assigned to Cl 2p and arises from the glovebox or sample transportation. Two tiny peaks at 100 eV and 150 eV in the 200Al_2O_3 film represent Si 2p and Si 2s, respectively, which are proved to be the surface contamination in Figure 5.12 (a). No other peaks were observed from the spectra of all four ALD films, suggesting that the desired ALD films were obtained in terms of chemical elements. Furthermore, there are no signals from the substrate in all survey spectra, which reveals dense and homogeneous ALD films.

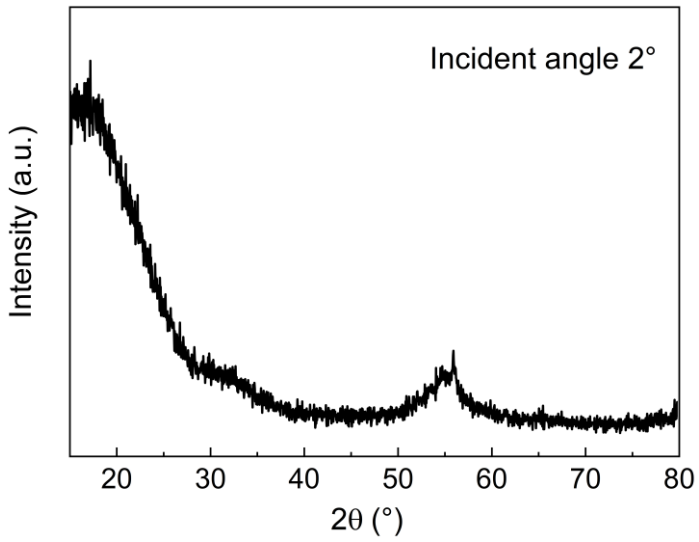

Figure 5.6: GIXRD pattern of the (20LiON-20Al_2O_3)x20 film.

To characterize the crystallinity of heterostructured ALD films, a GIXRD measurement was carried out on the (20LiON-20Al_2O_3)x20 film with an incident angle of 2°, as shown in Figure 5.6. Two broad diffractions at around 18° and 55° were observed from the pattern. The former corresponds to the reflection of the SiO_2 substrate and the latter corresponds to the (311) reflection of the Si substrate (*240*, *241*). No other visible reflections can be found in the pattern, demonstrating that the (20LiON-20Al_2O_3)x20 ALD film deposited at 200 °C is amorphous.

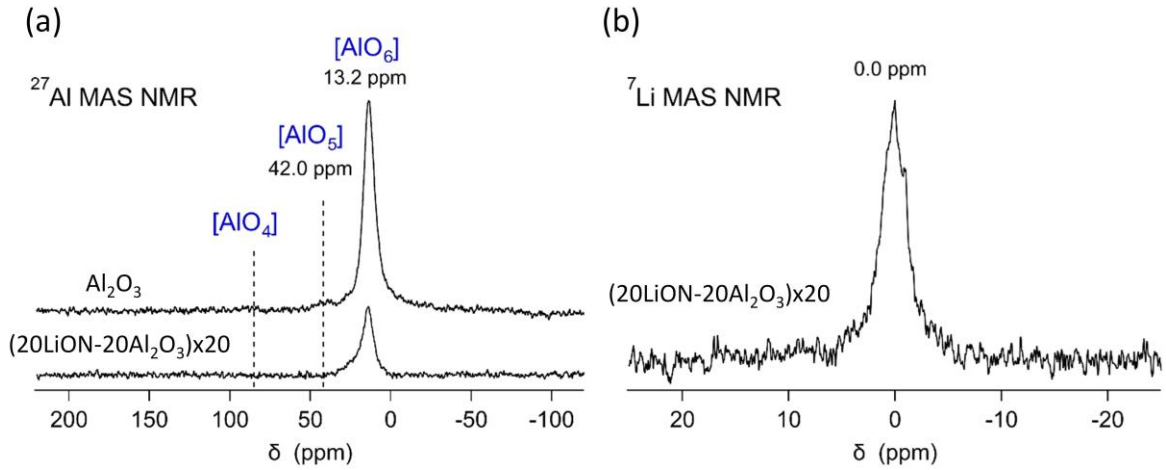

Figure 5.7: (a) ^{27}Al MAS NMR spectra of the (20LiON-20Al_2O_3)x20 film and the 200Al_2O_3 film ; (b) ^{7}Li MAS NMR spectrum of the (20LiON-20Al2O3)x20 film.

^{27}Al and ^{7}Li MAS NMR were carried out on the (20LiON-20Al_2O_3)x20 film to investigate the local structure of our ALD films. ^{27}Al MAS NMR of a pure 200Al_2O_3 film was also conducted as a reference. In Figure 5.7 (a), the ^{27}Al NMR spectra for both samples show predominantly a quite broad, symmetric peak at 13.2 ppm with large width of about 8 ppm. The position of this peak reveals that the Al ions in these samples are mostly present in octahedral [AlO_6] units, and tetrahedral units [AlO_4], as they are present in, e.g., crystalline γ-Al_2O_3 or γ-$LiAlO_2$, can be excluded (*242–244*). Furthermore, the large width of these peaks without any substructure hints at highly disordered or amorphous films, in agreement with the GIXRD results (*245*, *246*). For the 200Al_2O_3 sample, the presence of structural disorder is also confirmed by the presence of a small peak at 42.0 ppm representing a small amount of [AlO_5] units. The ^{7}Li NMR spectrum of the (20LiON-20Al_2O_3)x20 film in Figure 5.7 (b) reveals a broad peak centered around 0 ppm without substructure, again reflecting large variations in the local environments around the Li ions, as it is expected for amorphous materials.

5.3.2 Depth-dependent structural analysis

An in-depth analysis of the ALD films was carried out by creating a cross-section for imaging (SEM, TEM) or applying a sputter gun for XPS and ToF-SIMS measurements. Figure 5.8 (a) shows the cross-sectional SEM image of the (20LiON-20Al_2O_3)x20 film. The cross-section was simply prepared by breaking the sample along the scratch created by a diamond knife. Three different layers of the (20LiON-20Al_2O_3)x20 film, SiO_2 substrate, and Si substrate are observed

from the top to the bottom of the image. The thickness of the SiO_2 substrate is about 300 nm as expected and the (20LiON-20Al_2O_3)x20 is about 100 nm. For the preparation of the cross-section for high-resolution TEM, 40 ALD cycles of pure Al_2O_3 followed by the sputtering of a carbon film were deposited on the (20LiON-20Al_2O_3)x10 film to protect the sample. A focused ion beam (FIB) was then employed to create the cross-section, on which the TEM bright-field measurement was performed, as shown in Figure 5.8 (b). Except for the carbon above and dark SiO_2 substrate below, the bright regions in the TEM image represent LiON layers and the dark regions represent the Al_2O_3 layers. With this in mind, a relatively flat and clear layer-by-layer heterostructure is observed, although some damages of bright LiON sublayers caused by high energy electrons of TEM are visible (*247–251*). As expected, 10 bilayers of LiON and Al_2O_3 can be counted from this 35 nm multilayered (20LiON-20Al_2O_3)x10 film. According to the thickness and the number of ALD cycles of the Al_2O_3 protection layer, the deposition rate of Al_2O_3 is determined to be about 1 Å/cycle. With this in mind, the deposition rate of LiON can be calculated to be about 0.8 Å/cycle. All the thicknesses in Table 5.1 are calculated based on the deposition rates of the LiON sublayer and the Al_2O_3 sublayer. It is noted that the calculated thickness of the (20LiON-20Al_2O_3)x20 film with 72 nm is lower than 100 nm from the cross-sectional SEM image. This probably results from the damage of the sample during the preparation of the SEM cross-section.

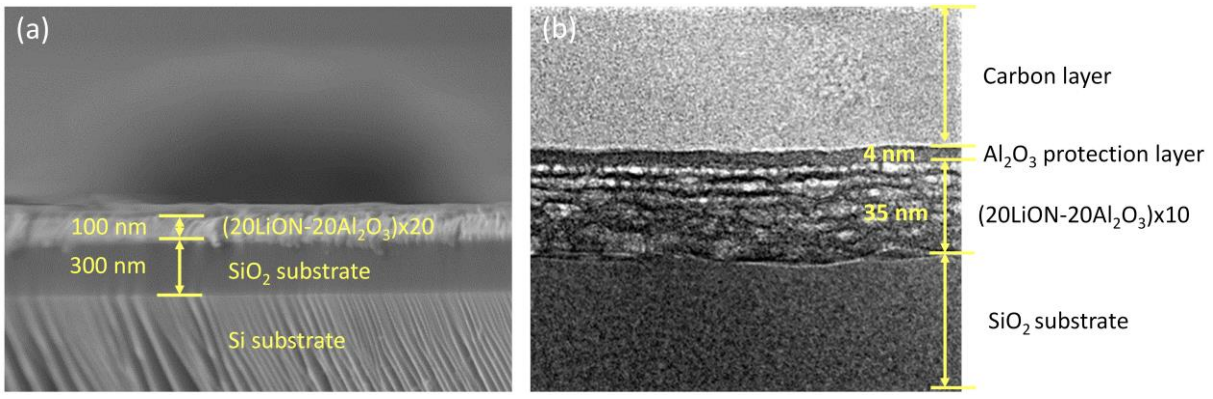

Figure 5.8 (a) Cross-sectional SEM image of the of the (20LiON-20Al_2O_3)x20 film; (b) Cross-sectional TEM bright-field image of the (20LiON-20Al_2O_3)x10 film (bright for LiON layers, dark for Al_2O_3 layers).

In order to further investigate the layer-by-layer structure of our multilayered film, a 200 x 400 μm^2 wedge-shaped crater with increasing erosion depth was sputtered on the (20LiON-

$20Al_2O_3$)x20 film by 2 keV Cs^+ ions, as illustrated in Figure 5.9 (a). This crater provides a laterally magnified cross-section of the film's topmost layers since the small angel wedge increases the detected area (*252*, *253*) Figure 5.9 (b) shows the positive ion ToF-SIMS imaging on this wedge structure marked with a red line in Figure 5.9 (a). A strong signal of Li^+ ions (in red) was detected around the crater without sputtering as well as in the crater with weak erosion, indicating that the topmost layer is a Li-rich sublayer (1st LiON sublayer). With increasing sputtering depth, the first LiON sublayer was removed and the first Al-rich sublayer (1st Al_2O_3 sublayer) in green is observed in the upper part of the crater. When the film was even deeper eroded, the intensity of Al^+ ions decreases while that of Li^+ ions increases. This happens because both the first LiON sublayer and the first Al_2O_3 sublayer were removed by relatively stronger sputtering and the second LiON sublayer was detected. A small amount of Al^+ ions is detected in the Li-rich sublayer and vice versa. Possible reasons are the slightly lower thickness of each sublayer relative to the sampling depth of ToF-SIMS (approximately 2 nm) and sputter-induced migration. The yellow part of the picture refers to the boundary of the wedge, which contains strong signals from both Li^+ and Al^+ owing to the nature of the crater walls. The topmost three sublayers of the (20LiON-$20Al_2O_3$)x20 film were proved to exist in a layer-by-layer structure. It is not possible to observe more sublayers due to the enhanced mixing of elements for extensive sputtering.

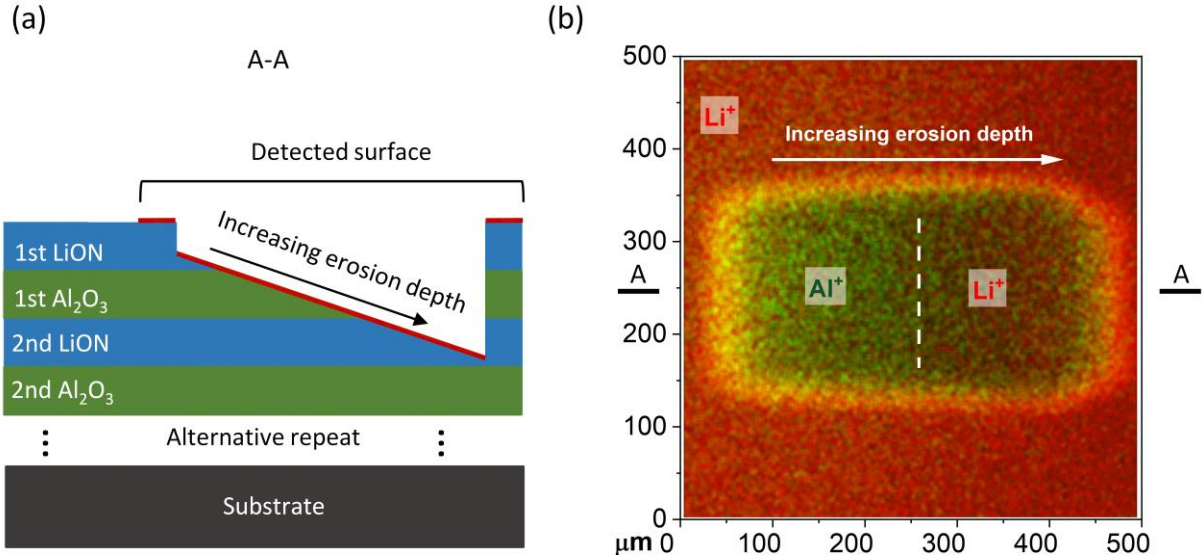

Figure 5.9: (a) Schematic cutaway view (A-A) of the wedge-shaped crater of the (20LiON-$20Al_2O_3$)x20 film; (b) Overlaid positive ion ToF-SIMS map of Li^+ and Al^+ on the wedge-shaped crater (green for Al^+, red for Li^+, yellow for the mixture of Al^+ and Li^+).

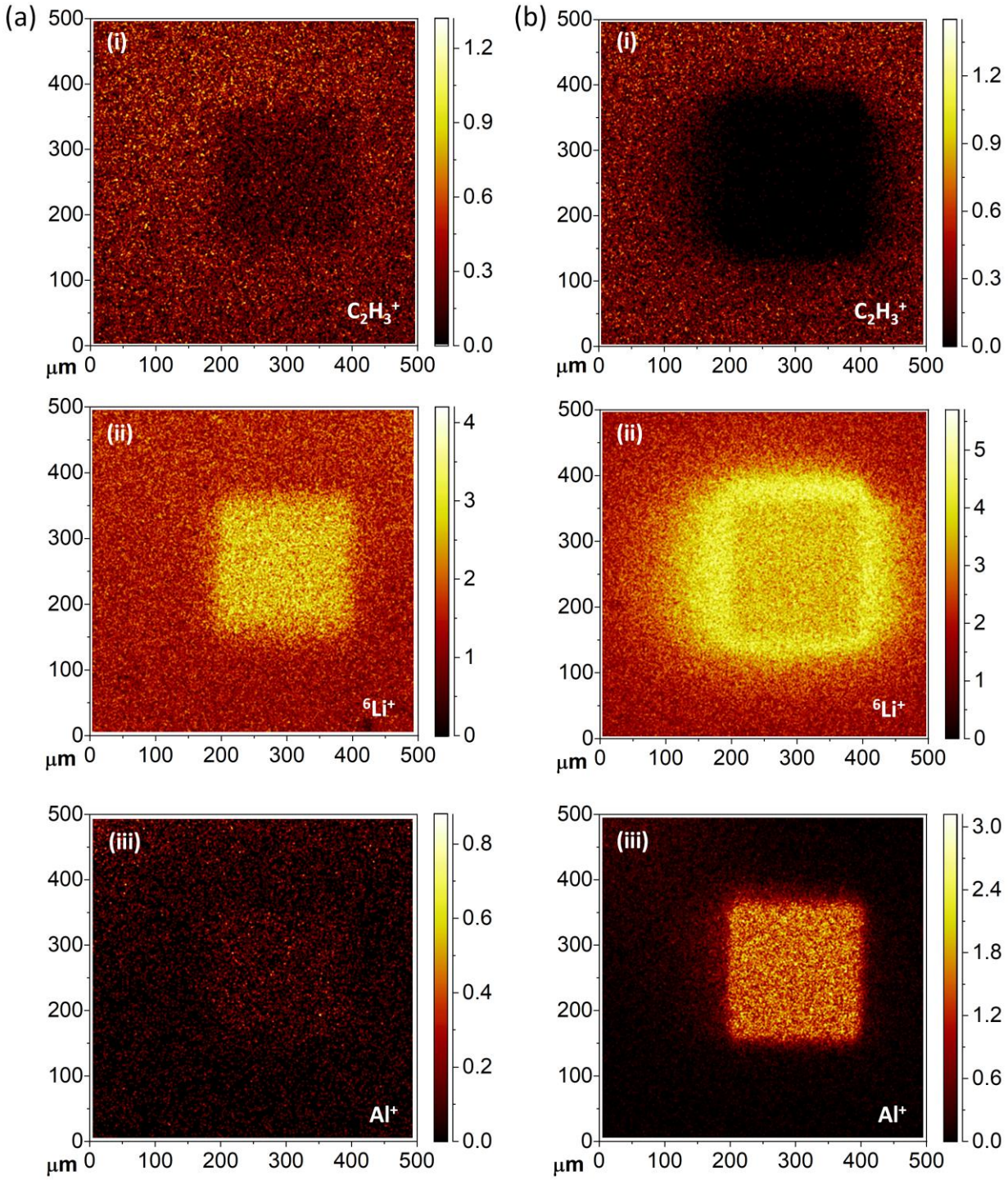

Figure 5.10: Positive ion ToF-SIMS mappings of the (75LiON-10Al_2O_3)x08 film with a crater etched by 2.5 keV (a) and 20 keV (b) Ar clusters for 0.1 ms: (i) $C_2H_3^+$, (ii) $6Li^+$, (iii) Al^+.

Another approach to explore the layer-by-layer heterostructure is the use of a weak or short sputtering to etch only a single topmost sublayer. The minimum dwell time of 0.1 ms was utilized for the weak erosion of the (75LiON-10Al_2O_3)x08 film. Figure 5.10 (a) shows the positive ion ToF-SIMS imaging on the crater sputtered by 2.5 keV Ar^+ clusters for 0.1 ms. In

Figure 5.10 (a)(i) and(ii), fewer $C_2H_3^+$ but more $^6Li^+$ ions were detected in the crater compared with the ions around the surface. This means that some of the carbonaceous contamination was removed and more signal from the first Li-rich sublayer was found after the weak erosion. Since the sampling depth of ToF-SIMS (1-2 nm) is in the same range as the thickness of our sublayer (1.8-2 nm), a negligible amount of Al^+ appeared on the surface around the crater, and very little Al^+ was detected in the crater either, see Figure 5.10 (a)(iii). These results demonstrate that the topmost layer is a Li-rich layer (first LiON sublayer) with some carbonaceous contamination on the topmost surface. By contrast, $C_2H_3^+$ ions were completely removed when the sputter gun was operated at a higher energy of 20 keV was applied for 1 ms, as displayed in Figure 5.10 (b)(i). Figure 5.10 (b)(ii) shows that Li^+ ions were still in the crater after the stronger sputtering because the employed high-energy Ar^+ clusters lead to the migration of Li^+ ions which is also proved by the special distribution of Li^+ ions around the crater. Figure 5.10 (b)(iii) shows that a strong signal of Al^+ ions was observed in the crater but no Al^+ ions were found on the surface around the crater, which again suggests that there is an Al-rich layer (first Al_2O_3 sublayer) under the first Li-rich layer. It can be concluded that the topmost bilayer of the first LiON sublayer and the first Al_2O_3 sublayer below are separated in the prepared (75LiON-10Al_2O_3)x08 film. However, the sputter-induced migration hampers the measurement for deeper sublayers.

Compared to the in-depth analysis by ToF-SIMS, ARXPS is a nondestructive technique without migration of ions induced by sputtering. Hence, ARXPS was also performed to probe the layer-by-layer structure of our multilayered ALD films. It is worth noting that the information depth of ARXPS is about 5-10 nm at the tilt angle (φ) of 0° and about half of that at 60°. According to the deposition rates of LiON (0.8 Å/cycle) and Al_2O_3 (1 Å/cycle) calculated from the TEM image, the thicknesses of the LiON (75 ALD cycles) and the Al_2O_3 (10 ALD cycles) sublayer of the (75LiON-10Al_2O_3)x08 film are around 6 nm and 1 nm, respectively. Therefore, the (75LiON-10Al_2O_3)x08 film with a thicker LiON sublayer was chosen to conduct ARXPS measurement, considering the sampling depth of ARXPS after tilting reaches still over 2 nm. Figure 5.11 (a) and (b) present high-resolution XPS spectra of Li 1s and Al 2p from 0° to 70° for the (75LiON-10Al_2O_3)x08 film, respectively. Photoelectrons from both Li 1s and Al 2p were detected at 0° due to the higher sampling depth of ARXPS which is larger than the thickness of the first bilayer of the (75LiON-10Al_2O_3)x08 film (7 nm). When the sample was rotated to a higher tile angle,

peak intensities of both Li 1s and Al 2p decreases due to the increase of signals from the surface contaminations. At a tilt angle of 60°, the signal of Al 2p fades away but that of Li 1s remains, which indicates that there is a pure Li-rich layer without Al on the topmost surface. These results again demonstrate that the sublayers of the (75LiON-10Al_2O_3)x08 film were individually deposited (at least the topmost bilayer) instead of a mixture of LiON and Al_2O_3.

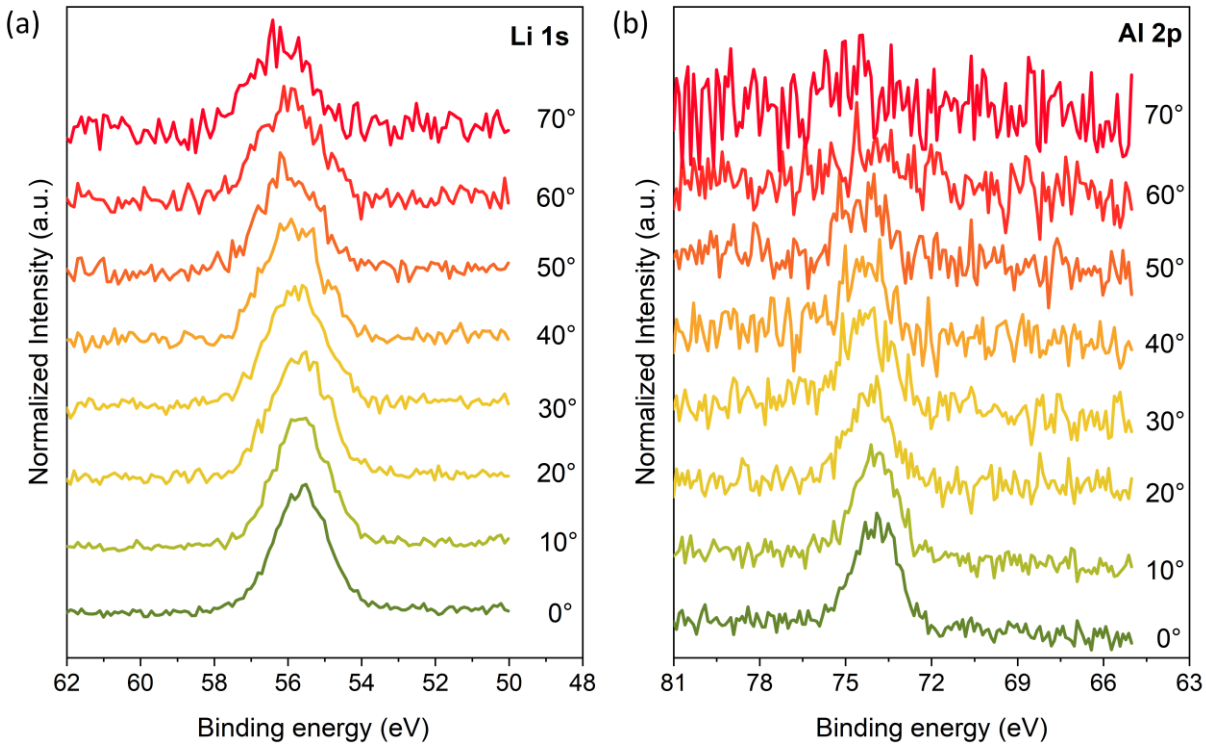

Figure 5.11: ARXPS spectra of the (75LiON-10Al_2O_3)x08 film in the Li 1s (a) and Al 2p (b) ranges collected over φ values from 0° to 70°.

XPS sputter depth profiling was conducted to obtain in-depth chemical information of the ALD films. Figure 5.12 (a) presents the XPS depth profile of a pure 200Al_2O_3 using a 1 keV monoatomic Ar^+ sputter gun. In accordance with the results of ToF-SIMS images, the carbonaceous contamination on the ALD film was removed after the first etching. The Si contamination, observed in the survey spectra in Figure 5.5, is also removed after the first etching. This indicates that the Si signal originates from the surface contamination instead of the substrate revealing the homogeneity of the 200Al_2O_3 film. In the inner film, the atomic concentrations of Al and O stay stable with a ratio of about 2:3, suggesting the formation of a pure Al_2O_3 film. After an etch time of 150 s, the signal of Si appears, and the content of O increases while that of Al decreases. This indicates that both the Al_2O_3 film and the SiO_2 were

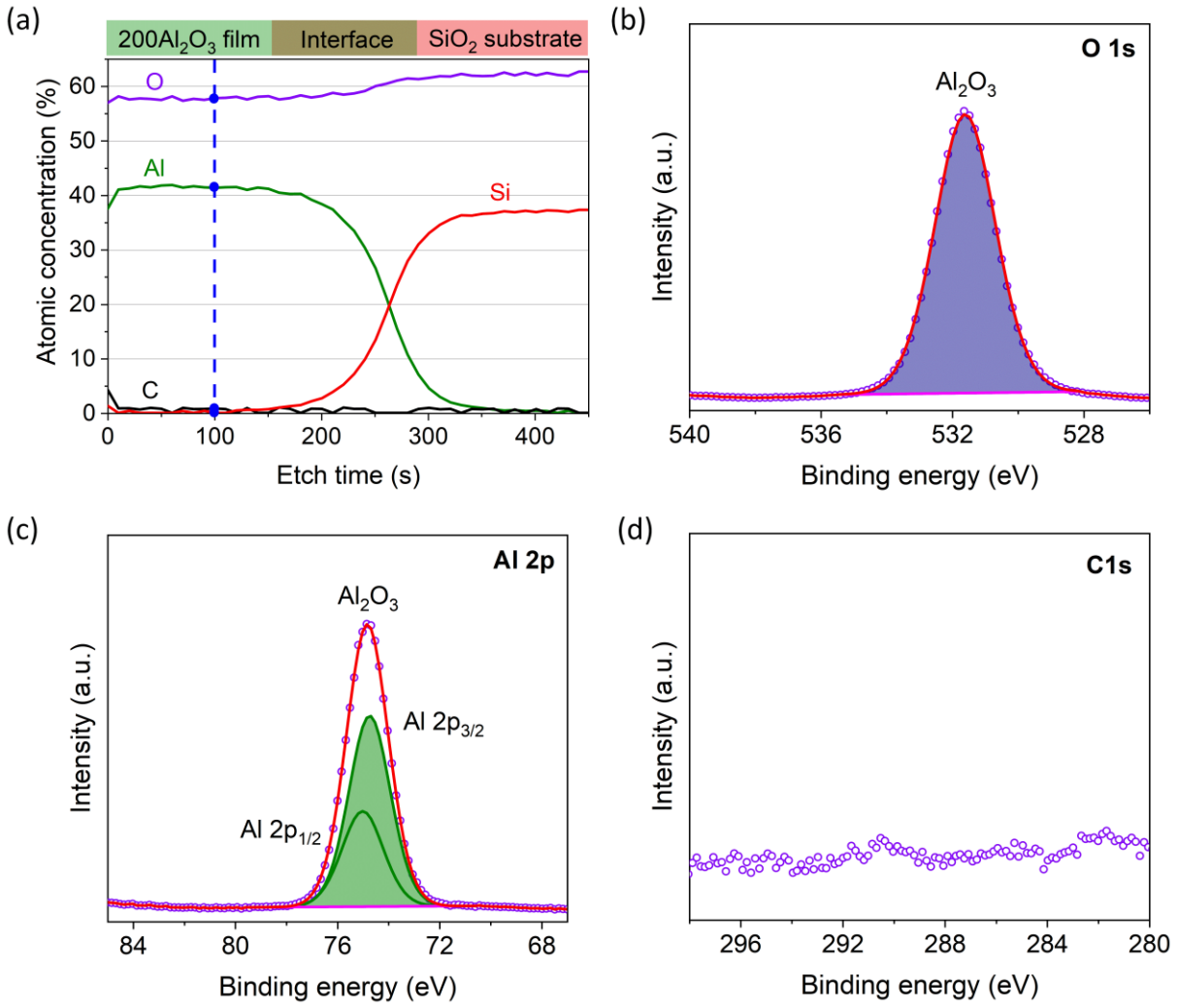

Figure 5.12: (a) XPS sputter depth profile of the $200Al_2O_3$ film; Fitted high-resolution XPS spectra of O1s (b), Al 2p (c), and C 1s (d) after 100 s sputtering (blue dashed line and blue points in (a)).

detected at the interface. The signal of Al disappears beyond 400 s and a pure substrate with a Si/O ratio of about 1:2 is observed from the concentration profile, in good agreement with the theoretical ratio of SiO_2. According to the thickness of the Al_2O_3 film (20 nm) and the etch time (400 s), the etching rate of the Al_2O_3 ALD film using 1 keV monoatomic Ar^+ sputter gun is 0.5 Å/s. Figure 5.12 (b), (c), and (d) are the fitted high-resolution O 1s, Al 2p, and C 1s XPS spectra, respectively, derived from the XPS depth profile at an etch time of 100 s. The O 1s spectrum was fitted with a single Voigt profile at a binding energy of 531.6 eV. A single doublet was used to fit Al 2p spectrum and the binding energy of Al $2p_{3/2}$ is around 74.7 eV. The binding energies of O 1s and Al $2p_{3/2}$ are close to the reported values for Al_2O_3 ALD film (*254*, *255*). No

obvious peak can be observed from C 1s which again indicates no carbon contamination in the inner Al_2O_3 film.

As another reference for multilayered heterostructures, XPS sputter depth profiling was also carried out on a pure 600LiON film with the same sputter gun, see Figure 5.13 (a). The chemical composition of the 600LiON varies throughout the film because Li^+ ions exhibit high mobility in the film under the effect of high-energy Ar^+ ion sputtering. Moreover, the extremely low ionization cross-section of the Li 1s photoionization leads to relatively large uncertainty in lithium quantification (*156*). Most of the carbon contamination on the surface of both films was removed after the first etching. The residual carbon in the inner film might originate from the residual precursors after N_2 purging or elemental redistribution during sputtering. Nitrogen was incorporated into the 600LiON film with approximately 4 atomic % after removing surface contamination. There are more than 50 atomic % of Li and 40 atomic % of O in the inner 600LiON film. A large amount of Li was also detected at the interface and even in the substrate of the film due to the sputter-induced implantation. Similarly, pure SiO_2 substrate with an expected molar Si/O ratio of 1:2 is observed after 350 s erosion. Due to the high mobility of Li^+ during sputtering, the film is deemed to be etched through after 200 s when no obvious nitrogen peak can be detected. Taking the calculated thickness of LiON into consideration, the etching rate of LiON using a 1 keV monoatomic Ar+ sputter gun is approximately 2.4 Å/s.

XPS sputter depth profile derived from integrated peak areas only provides information about the composition. Figure 5.13 (b)-(f) illustrate more details about the chemical environments of the 600LiON film by fitting high-resolution Li 1s, O 1s, C 1s, N 1s, and Si 2p spectra after 100 s sputtering. All the spectra were referenced to the surface adventitious C 1s peak of C-C/C-H at 285.0 eV binding energy. As can be seen in Figure 5.13 (b), the peaks of LiOH, Li_2CO_3, and Li_3N in Li 1s spectra are strongly overlapping at around 55.4 eV except for Li_2O at a lower binding energy of 54.4 eV (*234*, *256*, *257*). The O 1s spectrum in Figure 5.13 (c) can be deconvoluted into 3 components: Li_2O at 529.2 eV, LiOH/Li_2CO_3/C=O at 531.9 eV, and SiO_2/C-O at 533.4 eV (*258*). The binding energies of LiOH and Li_2CO_3 in both Li 1s spectrum and O1s spectrum are very close (*256*, *257*). Therefore, it is difficult to distinguish LiOH and Li_2CO_3 in the ALD films via XPS. Figure 5.13 (d) shows the fitting of the C 1s with four components of C-

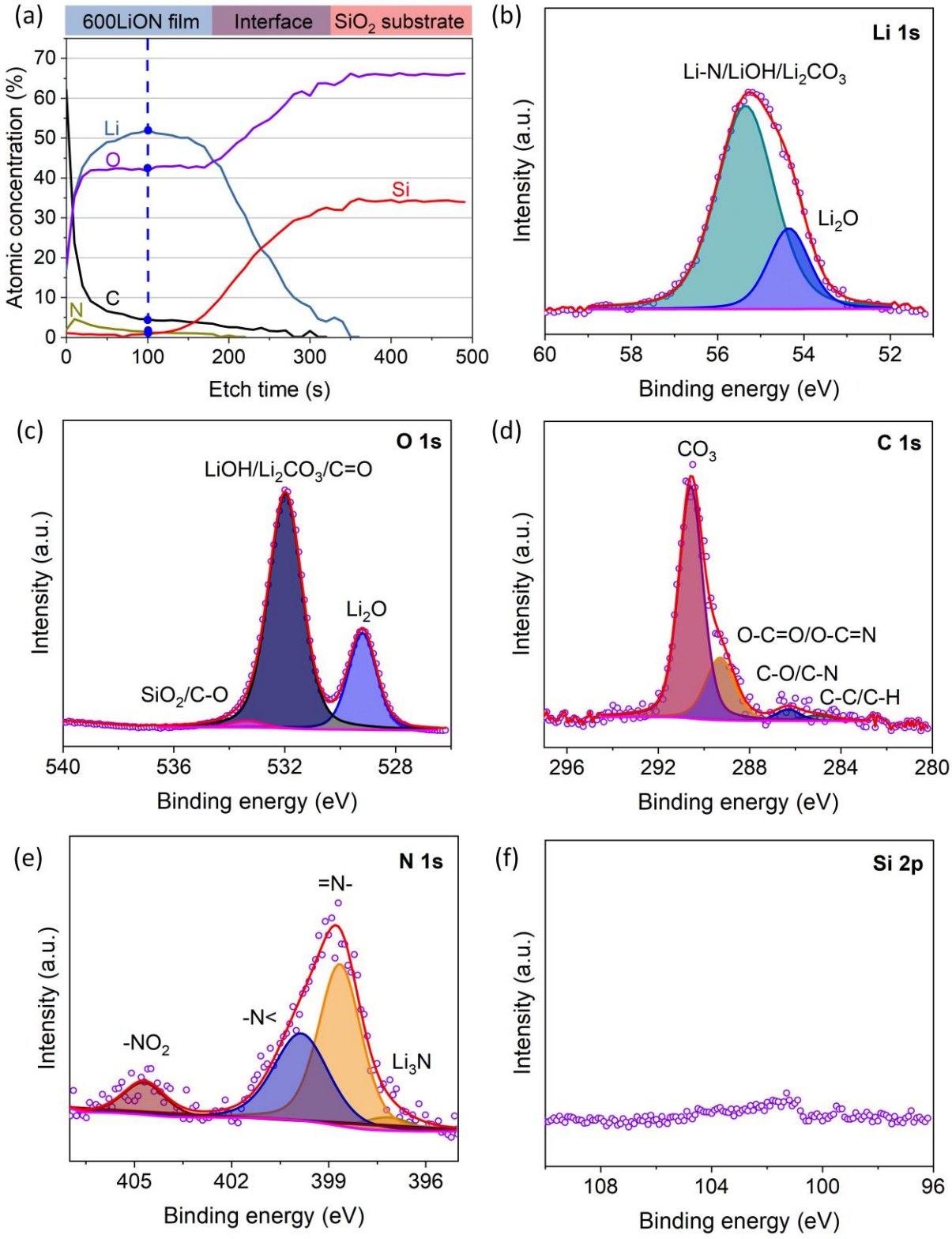

Figure 5.13: (a) XPS sputter depth profile of the 600LiON film; Fitted high-resolution XPS spectra of O1s (b), Al 2p (c), and C 1s (d) after 100 s sputtering (blue dashed line and blue points in (a)).

C/C-H at 285 eV,C-O/C-N at 286.3 eV, to O-C=O/O-C=N at 289.3 eV, and Li_2CO_3 at 290.5 eV (*259*, *260*). Carbon bonds of C-O, O-C=O, and CO_3 might originate from the Li precursor (LiO^tbu). The N 1s spectrum reveals four different bonds: Li_3N at 397.2 eV, -N= at 398.6 eV, -N< at 399.8, and $-NO_2$ at 404.7 eV, as shown in Figure 5.13 (e) (*259*, *260*). A small amount of nitrogen is located in an environment similar to that of Li_3N, while the majority of nitrogen is linked to carbon by single or double bonds. The residual nitrogen is attached to oxygen which stems from oxygen-containing precursors. There is no obvious Si 2p peak in Figure 5.13 (f) which demonstrates the high lateral homogeneity of the ALD films even after 100 s sputtering. In summary, the main compounds in the pure LiON film are LiOH, Li_2O, Li_2CO_3, and Li-N.

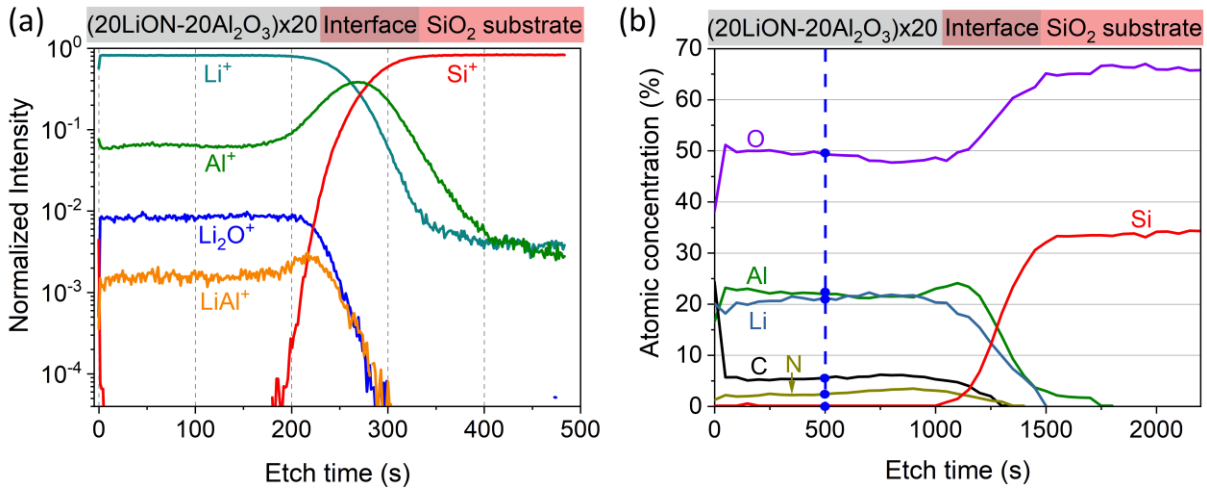

Figure 5.14: (a) Positive ion ToF-SIMS sputter depth profile of the (20LiON-20Al2O3)x20 film. (b) XPS sputter depth profile of the (20LiON-20Al_2O_3)x20 film. The dashed blue line and blue points relate to the fitted spectra at 500 s, see Figure 5.15.

Multilayered (20LiON-20Al2O3)x20 film was prepared by alternatingly stacking the pure LiON sublayer and pure Al2O3 sublayer. In order to obtain the in-depth elemental information of the multilayered heterostructure, ToF-SIMS sputter depth profiling was carried out on the multilayered (20LiON-20Al_2O_3)x20 film. Figure 5.14 (a) shows the ToF-SIMS sputter depth profile of the (20LiON-20Al_2O_3)x20 film eroded with a 20 keV Ar_{1500}^+ cluster sputtering ion gun. No compositional information can be obtained from ToF-SIMS depth profiling owing to the matrix-dependent ionization probabilities of different elements. The analysis shows the presence of Li^+, Al^+, Li_2O^+, and $LiAl^+$, uniformly distributed throughout the film. After 300 s of etching, Li_2O^+ and $LiAl^+$ tend to be etched out while Li^+ and Al^+ were still found in the Si^+-

containing substrate because of the ionic implantation induced by the high-energy Ar clusters. The enrichment of Al^+ and $LiAl^+$ at the interface results from lower mobility of Al-containing ions and weaker implantation compared with Li^+ ions. The expected fluctuant profile for the multilayer system was not observed since the sputter-induced migration. Based on the etch time of around 300 s and the film thickness of approximately 72 nm, the etching rate of the multilayered (20LiON-20Al_2O_3)x20 film applying a 20 keV Ar_{1500}^+ cluster is 2.4 Å/s.

To explore the in-depth chemical environment of the multilayered (20LiON-20Al2O3)x20 film, XPS sputter depth profiling was carried out applying a 1 keV monoatomic Ar^+ sputter gun, shown in Figure 5.14 (b). Similarly, most carbon contamination is located on the topmost surface of the film and the rest of the carbon in the inner film is probably attributed to the residual precursors or elemental redistribution caused by sputtering. Different from the XPS sputter depth profile of the pure 600LiON film, the elemental composition of the (20LiON-20Al_2O_3)x20 film remains constant with atomic concentrations of 21 % Li, 21 % Al, 50 % O, 5 % C, and 3 % N till the interface to the substrate. Li and Al detected at the interface or even in the substrate are deemed to be sputter-induced implantation. Similar to ToF-SIMS results, Al is slightly enriched at the interface between the film and the substrate because of its slow migration and implantation. According to both XPS and ToF-SIMS sputter depth profiles, elemental composition stays steady throughout the (20LiON-20Al_2O_3)x20 film. This in-depth uniform distribution may result from the low Li^+ ions mobility caused by the blocking effect of the insulating Al_2O_3 sublayers. Since the information depth of XPS (5-10 nm) exceeds the thicknesses of both LiON sublayer and Al_2O_3 sublayer, the layer-by-layer structure of the multilayer films cannot be resolved here. The etching of the (20LiON-20Al_2O_3)x20 film is considered to be finished after around 1350 s when no more nitrogen was detected by further sputtering. With this in mind, the etching rate of the multilayered (20LiON-20Al_2O_3)x20 by 1 keV monoatomic Ar^+ sputtering can be calculated to be 0.53 Å. As expected, this sputter gun etches the (20LiON-20Al_2O_3)x20 heterostructure slightly faster than the pure 200Al_2O_3 film while much slower than the pure 600LiON.

As an example of peak fitting, high-resolution O 1s, Al 2p, Li 1s, C 1s, N 1s, and Si 2p spectra of the (20LiON-20Al_2O_3)x20 film after 500 s sputtering (marked with a blue dashed line and blue points in Figure 5.14 (b)) are presented in Figure 5.15 (a)-(f), respectively. Compared to the 600LiON film, there is an additional peak in O 1s at a binding energy of 530.8 and an additional

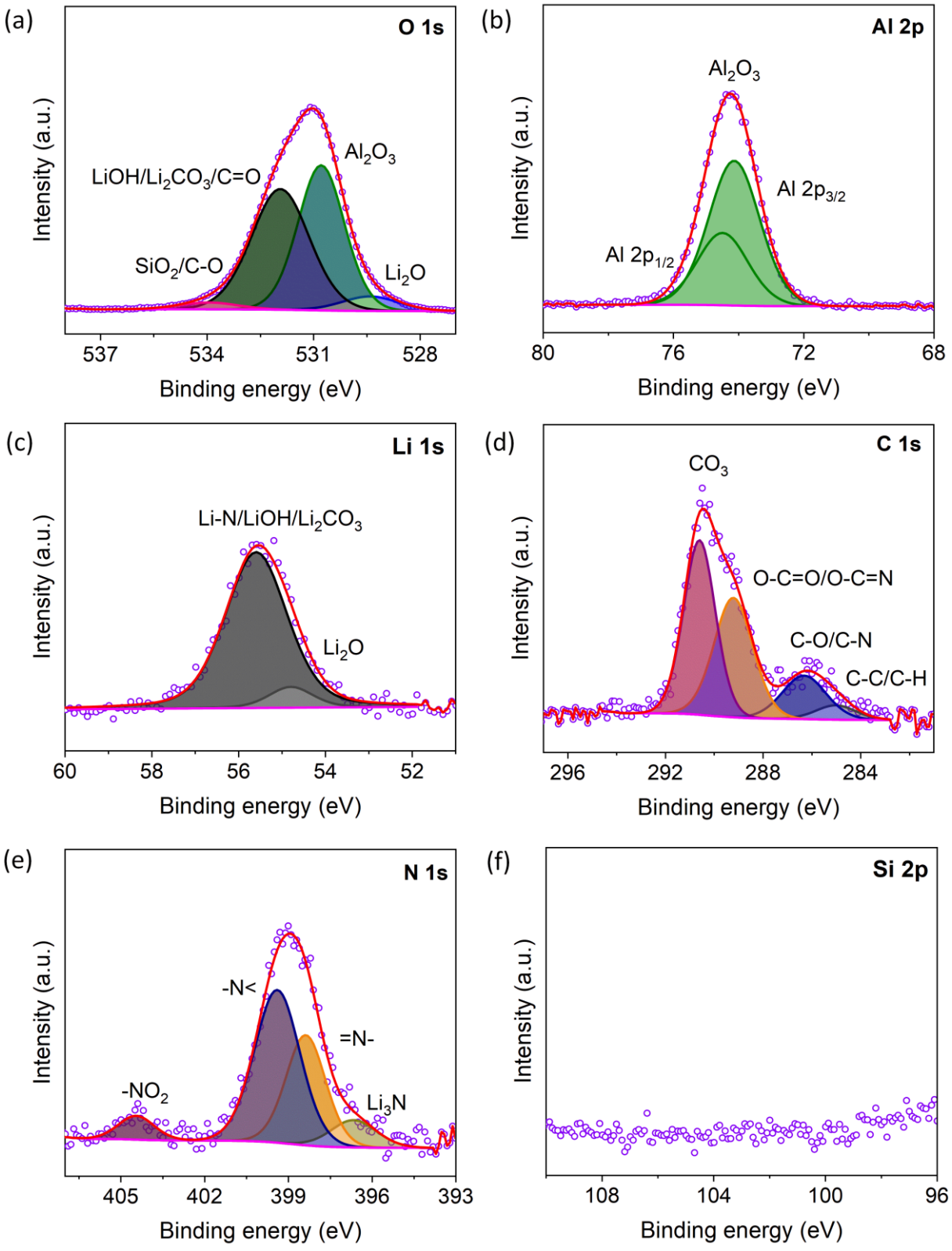

Figure 5.15: Fitted XPS spectra of the (20LiON-20Al_2O_3)x20 film after 500 s etching: (a) O 1s, (b) Al 2p, (c) Li 1s, (d) C 1s, (e) N 1s, (f) Si 2p.

Al 2p peak with Al $2p_{3/2}$ at 74.2 eV in Figure 5.15 (a) and (b), both of which are assigned to Al_2O_3 (*261*, *262*). These two peaks are shifted to higher binding energies compared with the pure 200Al_2O_3 film. Other XPS spectra were fitted in a similar way as the 600LiON film despite some small energy shifts: LiOH/Li_2CO_3/Li_3N at 55.7 eV and Li_2O at 54.9 eV for Li 1s in Figure 5.15 (c); C-C/C-H at 285 eV, C-O/C-N at 286.3 eV, O-C=O/O-C=N at 289.2 eV, and Li_2CO_3 at 290.6 eV for C 1s in Figure 5.15 (d); Li_3N at 396.8 eV, -N= at 398.3 eV, -N< at 399.3, and -NO_2 at 404.4 eV for N 1s in Figure 5.15 (e). Less Li_2O is present in the multilayered (20LiON-20Al_2O_3)x20 film as can be seen from both the O 1s spectrum and the Li 1s spectrum. The absence of a Si 2p peak from the substrate reveals homogeneously deposited ALD multilayered film.

According to the fitting results from Figure 5.15, a quantitative analysis of chemical environments in the inner (20LiON-20Al_2O_3)x20 film is presented in Figure 5.16. More than half of the atoms in the heterostructure of the (20LiON-20Al_2O_3)x20 belong to Al_2O_3. Li-containing compounds account for about 46.3 % of all atoms, corresponding to LiOH, Li_2CO_3, Li-N, and Li_2O with 22.9 %, 12.2 %, 6.2 %, and 5.0 % in atomic percentages, respectively. The remaining 3.1 atomic % belongs to the bonds between C, N, and O. Hydrogen is not included in the total amount of atoms since it is undetectable via XPS.

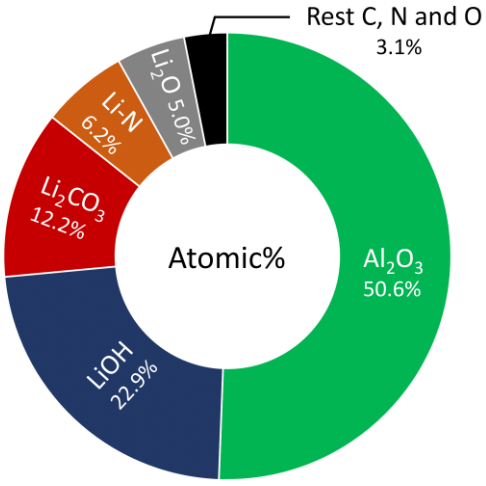

Figure 5.16: Pie chart of chemical compositions of the (20LiON-20Al_2O_3)x20 film after etching for 500 s based on the fitting results from Figure 5.15.

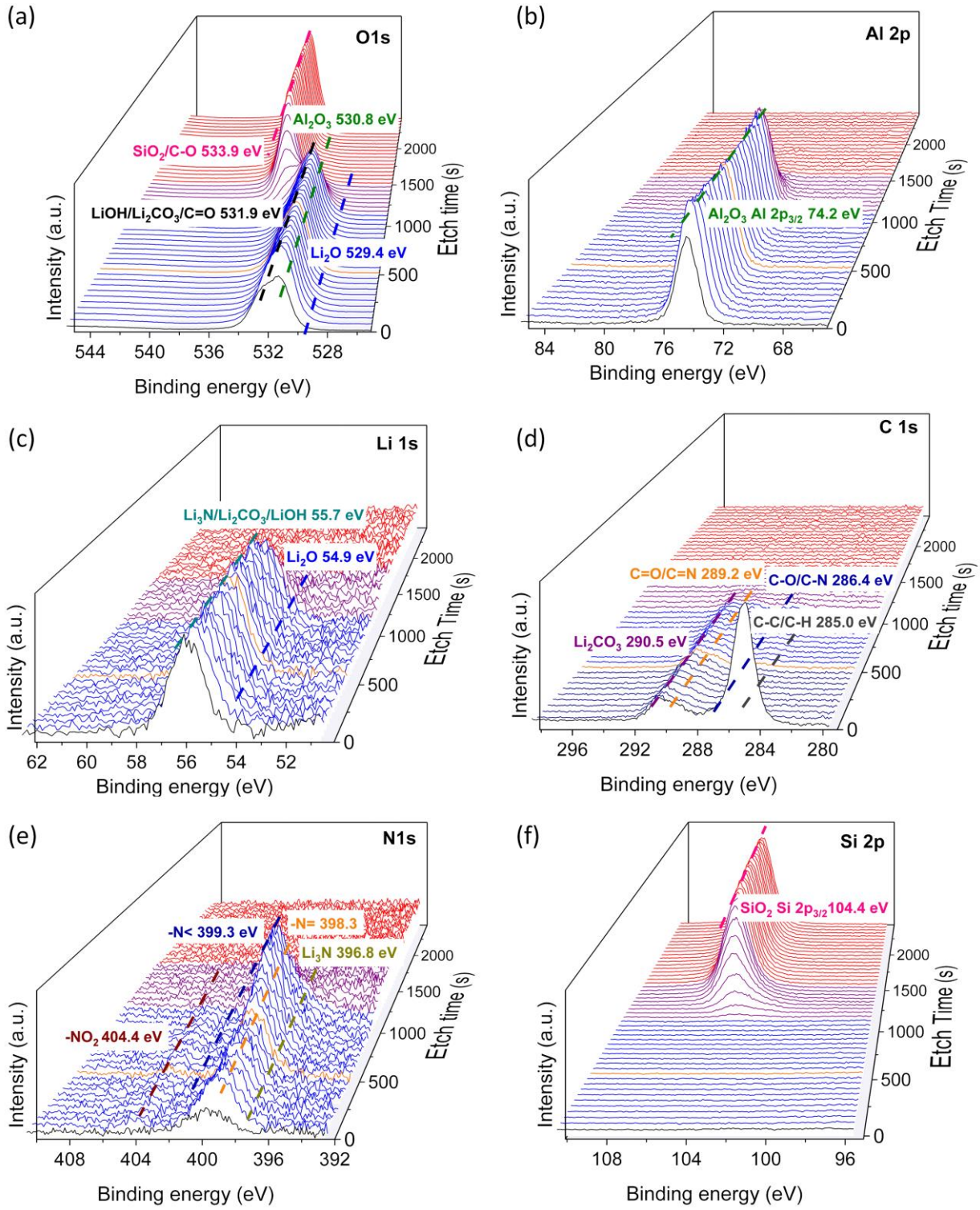

Figure 5.17: C 1s (a), N 1s (b), O 1s (c), Si 2p (d), Li 1s (e), and Al 2p (f) XPS spectra of the (20LiON-20Al_2O_3)x20 film as a function of etch time (black spectra for the surface; blue spectra for the inner film; violet spectra for the interface; red spectra for the substrate; orange spectra at 500 s etching time were fitted as presented in Figure 5.15).

Waterfall plots of O 1s, Al 2p, Li 1s, C 1s, N 1s, and Si 2p XPS spectra vs. etch time are presented in Figure 5.17(a)-(f) to track chemical bonds in the (20LiON-20Al_2O_3)x20 film during sputtering. In Figure 5.17, the first spectra on the topmost surface are plotted in black, the spectra of the inner film in blue, the spectra at the interface in violet, and the spectra of the substrate in red. All orange spectra at an etch time of 500s are used for fitting (see Figure 5.15). Figure 5.17 (a) shows stable O 1s spectra until the interface is reached, where the O 1s peak for SiO_2 at 533.9 eV appears corresponding to the Si 2p peak at a binding energy of 104.4 eV in Figure 5.17 (f), whilst the other three O 1s peaks for the ALD film fade away (*258*). Al 2p and Li 1s spectra in Figure 5.17 (b) and (c) stay steady throughout the film coinciding with the stable elemental compositions in the XPS sputter depth profile. The distinct change of the first spectra (in black) results from the elimination of a large amount of C-C/C-H at the topmost surface by sputtering, see Figure 5.17 (d). The residual Li_2CO_3 peak remains steady in the film until the interface, confirming the existence of Li_2CO_3 throughout the film. The peak intensity of N 1s in Figure 5.17 (e) goes up with increasing etch time indicating that the sputter-induced migration occurs for nitrogen as well.

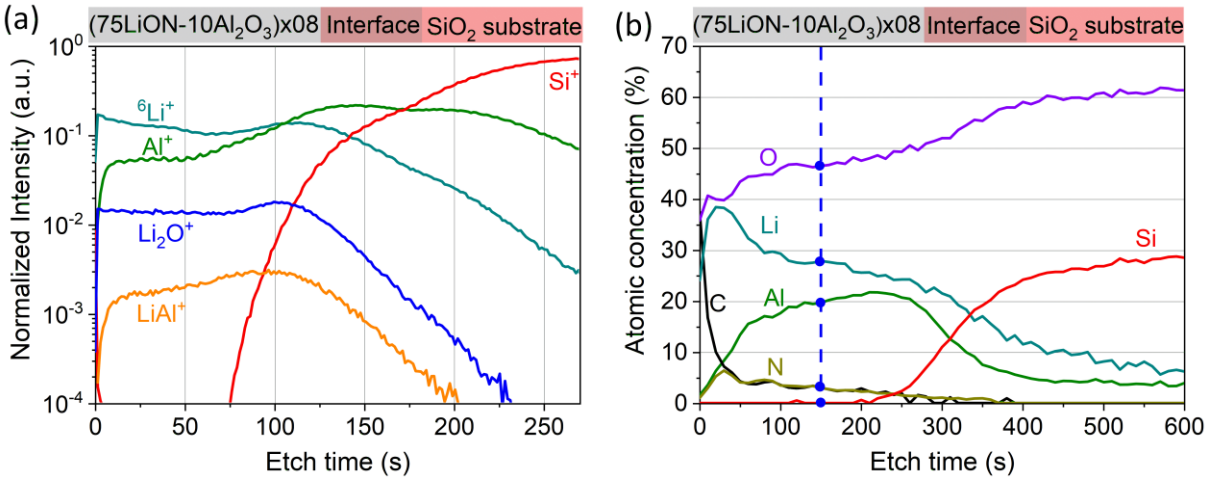

Figure 5.18: (a) Positive ion ToF-SIMS sputter depth profile of the (75LiON-10Al_2O_3)x08 film. (b) XPS sputter depth profile of the (75LiON-10Al_2O_3)x08 film. The dashed blue line and blue points relate to the fitted spectra at 150 s, as shown in Figure A 8.

Figure 5.18 (a) and (b) show positive ion ToF-SIMS and XPS depth profiles of the (75LiON-10Al_2O_3)x08 film. $^6Li^+$, Al^+, Li^2O, and $LiAl^+$ were detected at the (75LiON-10Al_2O_3)x08 film in the ToF-SIMS sputter depth profile. Owing to the influence of the sputter gun, these ions inhomogeneously distribute throughout the film and a large amount of them is implanted into

the substrate due to high ionic mobility. The XPS sputter depth profile shows that more Li is found in the (75LiON-10Al_2O_3)x08 film than in the (20LiON-20Al_2O_3)x20 film due to a higher ratio of LiON ALD cycle to Al_2O_3 ALD cycle. However, no apparent plateau is visible in the concentration depth profile of the (75LiON-10Al_2O_3)x08 film, and strong sputter-induced implantation at the interface is observed, confirming high ionic mobility under sputtering. The chemical environments of the (75LiON-10Al_2O_3)x08 film are similar to that of the (20LiON-20Al_2O_3)x20 film (see the fitted spectra in Figure A 8).

It is noted that both positive ion ToF-SIMS and XPS depth profiles reveal that the non-conductive Al_2O_3 sublayers in the (75LiON-10Al_2O_3)x08 film can not effectively block sputter-induced ionic migration as in the (20LiON-20Al_2O_3)x20 film. The Al_2O_3 sublayer in the (75LiON-10Al_2O_3)x08 film (1 nm) is thinner than in the (20LiON-20Al_2O_3)x20 film (2 nm) while the opposite is true for the LiON sublayer. The Al_2O_3 sublayer in the (75LiON-10Al_2O_3)x08 film is too thin or not stable to prevent effectively the sputter-induced migration of Li^+ ions from the thick LiON sublayer (6 nm). XPS sputter depth profiles of the (50LiON-10Al_2O_3)x12 film, the (40LiON-10Al_2O_3)x15 film, and the (20LiON-10Al_2O_3)x30 film in Figure A 9 indicate that a more stable concentration profile is obtained when more Al_2O_3 sublayers are inserted into the same thickness of the LiON layer. Based on the XPS sputter depth profiles using 1 keV monoatomic Ar^+, the etch rates of the (75LiON-10Al_2O_3)x08 film, the (50LiON-10Al_2O_3)x12 film, the (40LiON-10Al_2O_3)x15 film, and the (20LiON-10Al_2O_3)x30 film are about 1.6 Å/s, 1.3 Å/s, 1.2 Å/s, and 0.8 Å/s. As expected, the Al_2O_3 sublayers slow down the erosion in the multilayered LiON-Al_2O_3 films.

5.3.3 Ionic conductivity

The impedance measurements were done mainly by Dr. Andy Fiedler in the group of Prof. Xiang Yang Kong in the Institute of Materials for Mobile Energy, Shanghai Jiao Tong University, China.

The in-plane ionic conductivities of the pure 600LiON film and all multilayered heterostructures listed in Table 5.1 were characterized by impedance spectroscopy at temperatures between 120 °C and 180 °C. Figure 5.19 (a) presents typical Nyquist plots of the (75LiON-10Al_2O_3)x08 film, the (20LiON-20Al_2O_3)x20 film, and the pure 600LiON film at 160 °C.

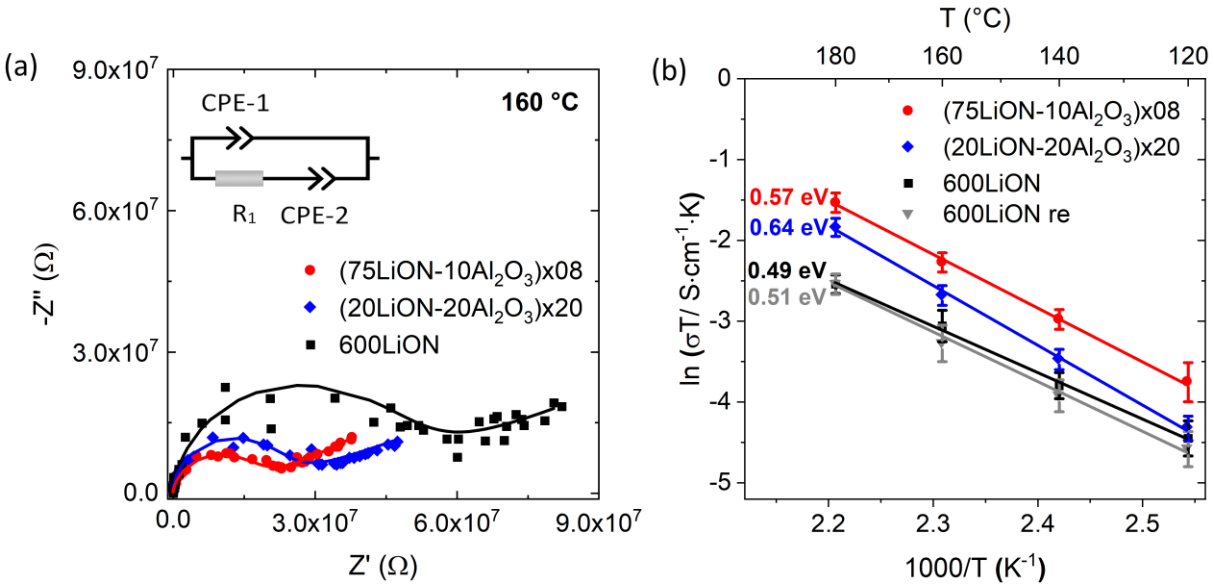

Figure 5.19: (a) Nyquist plots of the pure (75LiON-10Al_2O_3)x08 film, the (20LiON-20Al_2O_3)x20 film, and the 600LiON film at 160 °C; (b) Arrhenius plots of the (75LiON-10Al_2O_3)x08 film, the (20LiON-20Al_2O_3)x20 film, and the 600LiON film (two samples) in the temperature range of 120-180 °C.

All spectra comprise one semi-circle in the high-frequency region and an inclined line in the low-frequency region. The semi-circle represents the response of the film for Li^+ conduction and the inclined line can be ascribed to the diffusion of Li^+ ions which starts at a frequency of about 5 Hz. The impedance spectra were fitted with the equivalent circuit as shown in the inset of Figure 5.19 (a) using the software Relaxis 3 (rhd Instruments, Germany). R represents the ionic resistance of the film and the constant phase element CPE1 (Q_1) represents the capacitance of the experimental setup and the sample. The other CPE2 (Q_2) corresponds to the diffusion part in the Nyquist plot, which can be regarded as a Warburg-type CPE. The corresponding fitting parameters at 160 °C are shown in Table S 1. The ionic conductivities of all ALD films were calculated using Equation 5.1. Both the multilayered (75LiON-10Al_2O_3)x08 films and the multilayered (20LiON-20Al_2O_3)x20 show a smaller semi-circle than the pure 600LiON film at 160 °C, which can be explained as follows: the multilayered heterostructures have lower resistance than the 600LiON film at this temperature. The corresponding ionic conductivities at 160 °C are 2.8 x 10^{-4} S/cm for the (75LiON-10Al_2O_3)x08 film and 2.5 x 10^{-4} S/cm for the (20LiON-20Al_2O_3)x20 film, which are both higher than 1.1 x 10^{-4} S/cm for the

600LiON film. The conductivities of both heterostructured LiON-10Al_2O_3 films are higher than that of previously published $Li_xAl_yO_z$ ALD films without nitrogen dopant. (*232–234*)

As demonstrated in Figure 5.19 (b), the conductivities of all three films increase exponentially with increasing temperature, indicating a thermally activated conduction mechanism of our thin films. Both single 600LiON films share similar conductivity and activation energy indicating good reproducibility of these experiments. Both multilayered films exhibit higher ionic conductivity than the two pure 600LiON films in the temperature range of 120-180 °C. In other words, the ionic conductivity of the pure 600LiON film is enhanced by the interposition of non-conductive Al_2O_3 sublayers. One explanation is the introduction of heterointerfaces between LiON sublayers and Al_2O_3 sublayers. The dissimilarity in mobile ion concentrations of these two sublayers will lead to ion transfer across the heterointerface, forming a space charge region (*31*, *33*, *263*). The accumulation, depletion, and inversion effects of the charge carriers and defects in this region, i.e., space charge effect, can accelerate the transport of Li^+ ions due to an increase of concentration of point defects (*236*, *263–267*). The space charge effect has an effective range, known as the Debye length (λ_D) and the thicknesses of our sublayers are smaller than this length. As a result, the space charge regions are overlapping, and thus a stronger space charge effect impacts the ionic conduction (*32*, *235*, *236*). The slopes of the fitted lines in Figure 5.19 (b) provide the activation energies of the (75LiON-10Al_2O_3)x08 film, the (20LiON-20Al_2O_3)x20 film, and the 600LiON film with 0.57 (±0.02) eV, 0.64 (±0.01) eV, and 0.49 (±0.02) eV, respectively. Due to the insertion of Al_2O_3 sublayers, the activation energies of the multilayered (75LiON-10Al_2O_3)x08 film and the (20LiON-20Al_2O_3)x20 film increase owing to local structural distortions and the blocking effect brought by insulating Al_2O_3 sublayers (*235*, *268–270*). Consequently, more and thicker insulating Al_2O_3 sublayers in the (20LiON-20Al_2O_3)x20 film than in the (75LiON-10Al_2O_3)x08 film lead to a lower conductivity and higher activation energy. In summary, the heterointerfaces provide 2D channels for fast ionic conduction while increased activation energy. It is noteworthy that the (75LiON-10Al_2O_3)x08 film exhibits a higher conductivity than the (20LiON-20Al_2O_3)x20 film. This suggests a thickness-dependent ionic conductivity of multilayered heterostructures, which will be discussed in the following part.

In order to build optimized interfaces in the multilayer system for ionic conduction, three LiON-Al_2O_3 films with various thicknesses of Al_2O_3 sublayers were synthesized by ALD: a (40LiON-05Al_2O_3)x20, a (40LiON-10Al_2O_3)x20, and a (40LiON-20Al_2O_3)x20. These three films have the same thickness (3.2 nm) and number (40) of the LiON sublayers, while the thicknesses of the Al_2O_3 sublayer are adjusted to be 0.5 nm (05 subcycles), 1 nm (10 subcycles), and 2 nm (20 subcycles), respectively. The repetitions of the bilayer are the same for all three samples to ensure the same number of heterointerfaces. The temperature-dependent ionic conductivity of multilayered films vs. inverse temperature is presented in Figure 5.20 (a). The (40LiON-10Al_2O_3)x20 film shows the highest conductivity at all temperatures and the lowest activation energy of 0.58 (±0.02) eV. In contrast, (40LiON-20Al_2O_3)x20 with 2 nm Al_2O_3 sublayers exhibits lower ionic conductivity and higher activation energy due to the thicker non-conductive Al_2O_3 layers. For the (40LiON-05Al_2O_3)x20 film, 5 ALD subcycles of Al_2O_3 may not be enough to form a stable and uniform heterointerface for the interfacial conduction. As a result, the LiON-Al_2O_3 multilayer system with 1 nm Al_2O_3 sublayers provides better heterostructures for ionic conduction.

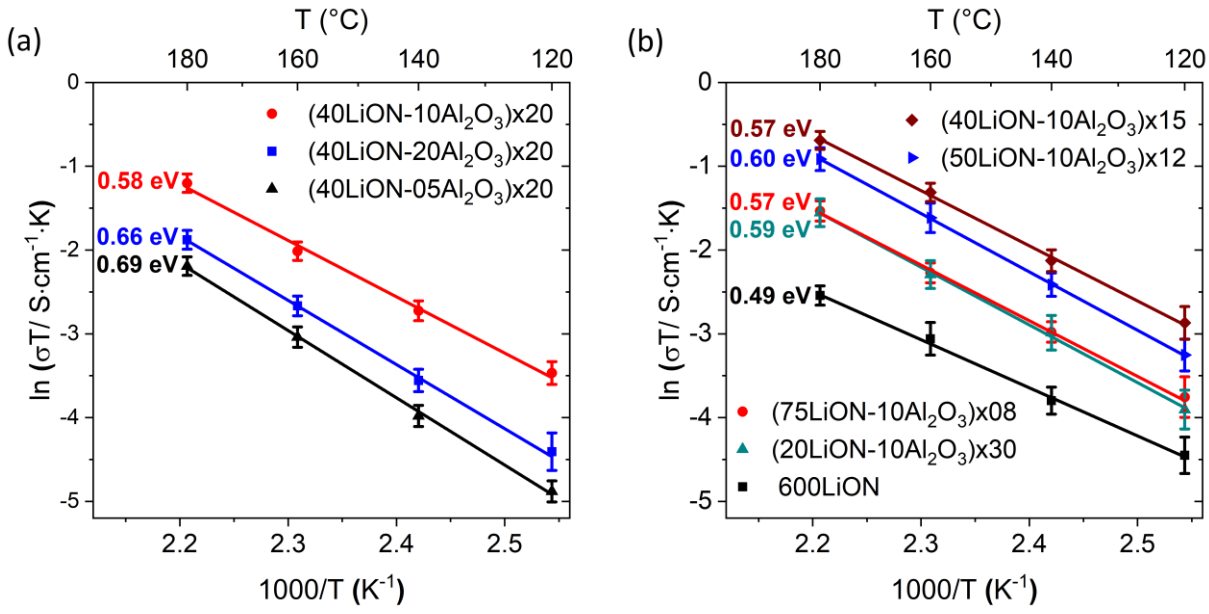

Figure 5.20: (a) Arrhenius plots of (40LiON-05Al_2O_3)x20 film, (40LiON-10Al_2O_3)x20 film, and (40LiON-20Al_2O_3)x20 film in the temperature range of 120-180 °C; (b) Arrhenius plots of the (20LiON-10Al_2O_3)x30 film, (40LiON-10Al_2O_3)x15 film, (50LiON-10Al_2O_3)x12 film, the (75LiON-10Al_2O_3)x08 film, and the pure 600LiON in the temperature range of 120-180 °C.

Apart from the Al_2O_3 sublayer, the thickness of the LiON sublayer also plays an important role in the conduction performance. Multilayered films with varied thicknesses of LiON sublayer were prepared by ALD: a (20LiON-10Al_2O_3)x30 film, a (40LiON-10Al_2O_3)x15 film, a (50LiON-10Al_2O_3)x12 film, and a (75LiON-10Al_2O_3)x08 film. In order to keep the amount of Li^+ ions the same for all these four samples, the number of total ALD cycles of LiON in all films is fixed to 600. These 600 cycles of LiON are evenly distributed in 8 bilayers, 12 bilayers, 15 bilayers, and 30 bilayers, respectively. With this in mind, the number of subcycles for each LiON sublayer is thus 75 subcycles, 50 subcycles, 40 subcycles, and 20 subcycles, respectively. These sublayers are separated by a 1 nm Al_2O_3 barrier layer which has demonstrated to be a better thickness for ionic conduction as discussed above. As expected, all these four multilayer films show higher ionic conductivities than the pure 600LiON film due to the space charge effect at the heterointerfaces as displayed in Figure 5.20 (b). They have a similar activation energy of around 0.58 eV, which may arise from the same thickness of the Al_2O_3 barrier layer and similar types of heterointerfaces. The (40LiON-10Al_2O_3)x15 film exhibits the best ionic conductivity of $6.2x10^{-4}$ S/cm at 160 °C. Compared to this sample, the (20LiON-10Al_2O_3)x30 film exhibits lower conductivity even if it contains double the number of heterointerfaces. This might be caused by the increased total thickness of the insulating Al_2O_3 layers, leading to stronger local distortions and blocking effect. For the (50LiON-10Al_2O_3)x12 film and the (75LiON-10Al_2O_3)x08 film, one possible reason is the less amount of Li^+ ions close to the heterointerfaces. Moreover, Li^+ ions can move not only along the interfaces but also in the direction perpendicular to the film when the LiON sublayer is over-thickened. That is to say, the Al_2O_3 sublayer can not effectively block the migration of Li^+ ions in the perpendicular direction, in good agreement with the XPS and ToF-SIMS depth profiles. These results demonstrate that (40LiON-10Al_2O_3)x15 with 3.2nm of LiON sublayer provides better heterointerfaces for ionic conduction.

The ionic conductivities of all LiON-Al_2O_3 films with various thicknesses of LiON (black) or Al_2O_3 (blue) at 160 °C, extracted from Figure 5.19 (b) and Figure 5.20 are displayed in Figure 5.21. All multilayer LiON-AlO_x films show higher ionic conductivity than the single 600LiON film at 160 °C, even if the lithium concentration of the multilayer films is lower than in the pure 600LiON films due to the insertion of insulating Al_2O_3 sublayer. A maximum can be observed for both series of samples. The (40LiON-10Al_2O_3)x15 film exhibits the highest conductivity with

$6.2x10^{-4}$ S/cm at 160 °C and an extrapolated value of $8.9x10^{-7}$ S/cm at RT among all LiON-Al_2O_3 multilayered heterostructures, which is higher than any previously reported $Li_xAl_yO_z$ ALD films (*232–234*). Besides, 3.2 nm LiON sublayer (40 subcycles) combined with 1nm Al_2O_3 sublayer (10 subcycles) is the best thickness combination in our multilayer system LiON-Al_2O_3 for ionic conduction. However, (40LiON-10Al_2O_3)x15 with fewer heterointerfaces shows higher conductivity than (40LiON-10Al_2O_3)x20. This could probably be explained by the difference in thickness between the two films (*264*, *271*).

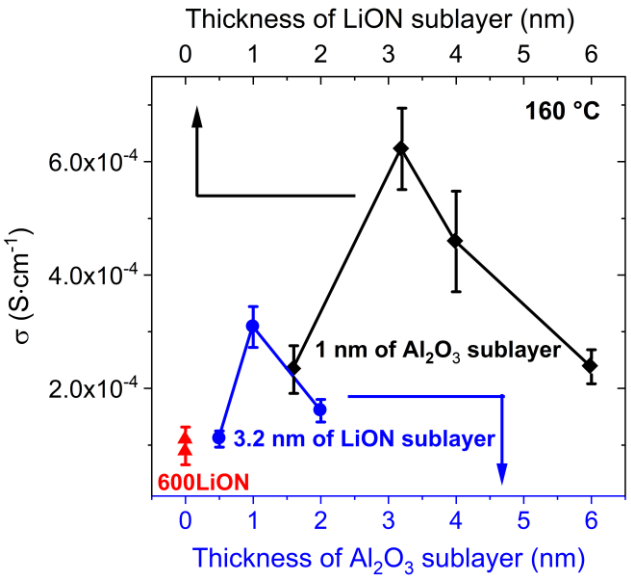

Figure 5.21: Sublayer-thickness-dependent ionic conductivity of LiON-Al_2O_3 films at 160 °C. The black and blue symbols refer to the dependence on the sublayer LiON and Al_2O_3 sublayer, respectively, while the thickness of the other layer is kept constant. Two identical 600LiON reference samples are shown in red color.

5.4 Conclusions

Novel heterostructured thin-film solid-state electrolytes LiON-Al2O3, synthesized via ALD, were investigated. Exemplarily characterizations were performed on the (20LiON-20Al_2O_3)x20 film and the (75LiON-10Al_2O_3)x08 film. Morphological and compositional data show that both ALD films are flat, pinhole-free, and homogeneous. GIXRD and MAS NMR results reveal that the multilayered (20LiON-20Al_2O_3)x20 film deposited at 200 °C is amorphous. Remarkably, the layer-by-layer structure with the sublayer thickness of around 2 nm was observed using cross-sectional HRTEM. ToF-SIMS images on the wedge-crater and normal crater show that the

topmost several sublayers of the heterostructure are individually deposited, which is confirmed by damage-free ARXPS measurement. Nevertheless, deeper sublayers are not able to be observed due to the limitation of these methods. The Al_2O_3 film was proved to be an extremely pure Al_2O_3 with the desired Al/O ratio of 2:3 as obtained by the XPS sputter depth profile, while that of the 600LiON is not that uniform due to the strong sputter-induced migration of Li^+ ions. By contrast, ToF-SIMS and XPS sputter depth profiles of the (20LiON-20Al_2O_3)x20 film present a stable plateau since the sputter-induced migration is blocked by insulating Al_2O_3 sublayers. Furthermore, the inner film of heterostructured (20LiON-20Al_2O_3)x20 mainly consists of Al_2O_3 from the Al_2O_3 sublayer and LiOH, Li_2CO_3, Li-N, and Li_2O from the LiON sublayer, as analyzed by XPS. Strong sputter-induced migration was observed also in the XPS depth profile of the (75LiON-10Al_2O_3)x08 film due to a less blocking effect of thinner Al_2O_3 sublayer but thicker LiON sublayer. This migration could be weakened by increasing the thickness of the Al_2O_3 sublayer or decreasing the thickness of the LiON sublayer.

Compared with the pure 600LiON film, the ionic conductivities of all multilayer LiON-Al_2O_3 films were increased by inserting non-conductive Al_2O_3 sublayers. This is remarkable since the overall concentration of Li^+ ions is lower, but the overall conductivity is enhanced. The space charge effect at the heterointerface is deemed to be the mechanism behind this enhancement. The increase of the activation energy mainly arises from local structural distortions induced by the insulating Al_2O_3 sublayers. LiON-Al_2O_3 films with nitrogen dopant, identified by EDX and XPS, exhibit a higher conductivity than previously reported $Li_xAl_yO_z$ ALD films without nitrogen. The thickness-dependent conductivity was investigated by impedance measurements of LiON-Al_2O_3 heterostructures with varied thicknesses of both sublayers. The combination of a 3.2 nm LiON sublayer and a 1 nm Al_2O_3 sublayer is proved to exhibit the best conductivity performance among all of our multilayer heterostructures. The (40LiON-10Al_2O_3)x15 film has the lowest activation energy of 0.57 eV and the highest ionic conductivity of 6.2×10^{-4} S/cm at 160 °C. These results enable the development of heterostructured thin films with highly conducting heterointerfaces by ALD as solid electrolytes/conductors for ionic devices.

6 Conclusions and Outlook

In this work, both heterogeneous composite and thin film solid electrolytes were synthesized to investigate the physicochemical and electrochemical properties of heterostructured materials with the variation of composition for SEs. To deeply understand their properties, various characterization methods were applied on both systems with systematically varied compositions. Remarkably, a higher conductivity was achieved with a specific combination of a good conductor and a bad conductor in both bulk-type and thin-film heterostructures. The underlying reason behind this is deemed to be the opposite effects: a space charge effect at the interface vs. local structural distortions and a blocking effect possibly in combination with the formation of new phases at the interface. The space charge effect at the heterointerfaces gives rise to the redistribution of charge carriers and point defects resulting in the acceleration of Li^+ ions transport along the interface. Local structural distortions and the blocking effect induced by the poor conductor can reduce the ionic conductivity of the heterogeneous system.

A series of heterogeneous (100-x)Li_3PS_4-xLi_3PO_4 ($10 \leq x \leq 40$) oxysulfides were synthesized by a two-step mechanical milling. The evolution of heterogeneous oxysulfides with various content of Li_3PO_4 dopant was systematically characterized by XRD, Raman spectroscopy, ^{31}P MAS NMR, and XPS. These results demonstrate that glass-ceramic heterogeneous composites with desired compositions were obtained by mechanical ball milling. Heterogeneous composites with x = 15 and x = 20 are more stable against Li metal and exhibit higher ionic conductivity than pure glass Li_3PS_4. Both oxysulfides with x = 15 and x =20 have similar AC conductivities of 1.6 x 10^{-4} S/cm at RT, while they have higher DC conductivities 9.5 x 10^{-4} S/cm and 2.4 x 10^{-3} S/cm at RT for x =15 and x =20, respectively, after stabilization by galvanostatic cycling. This suggests the formation of preferred interphase between heterogeneous oxysulfides and Li metal for ionic conduction, which even enables over 60 charge-discharge cycles in a full cell. Only heterogeneous composites with x = 15 and x = 20 have higher conductivity and lower activation energy than pure glass Li_3PS_4, while the other oxysulfides show opposite results. This phenomenon is attributed to the combined and opposite influences of the space charge effect and the blocking effect. Furthermore, three additional units of $[PS_3O]^{3-}$, $[PS_2O_2]^{3-}$, and $[PSO_3]^{3-}$ observed in ^{31}P MAS NMR spectra demonstrate the local structural changes and might also lead to the improvement of ionic conductivity.

Heterogeneous oxysulfides with x = 15 and x = 20 could improve the cycling stability and rate capability of a full cell to a certain extent, however, a large capacity loss was still observed due to the large resistance between Li_2CoO_2 and SE.

Heterogeneous novel LiON-Al_2O_3 thin films with multilayered structures were synthesized by ALD. The heterogeneous (20LiON-20Al_2O_3)x20 film is proved to be amorphous, flat, homogeneous, and pinhole-free. The layer-by-layer heterostructure with 2 nm thickness sublayers was observed by cross-sectional TEM and confirmed by ARXPS and ToF-SIMS images assisted with a sputter gun. XPS sputter depth profile shows that the multilayered (20LiON-20Al_2O_3)x20 film has a composition of Al_2O_3 for the Al_2O_3 sublayers and LiOH, Li_2CO_3, Li-N, and Li_2O for the LiON sublayers. Nitrogen-doped heterogeneous LiON-Al_2O_3 films exhibit higher conductivity than the $Li_xAl_yO_z$ ALD films described in the literature. Furthermore, almost all multilayered LiON-Al_2O_3 films have higher conductivity but also higher activation energy than the pure 600LiON film. The space charge effect at the heterointerfaces enhances the ionic conductivities of multilayered heterostructures, while the local structural distortions at the interface and the blocking effect of Al_2O_3 sublayers reduce the ionic conduction and increase the activation energy. Concerning these opposite effects, the optimized multilayered LiON-Al_2O_3 heterostructures consisting of 3.2 nm LiON sublayers and 1 nm Al_2O_3 sublayers exhibit the best conductivity. The heterostructured (40LiON-10Al_2O_3)x15 film has a conductivity of $6.2x10^{-4}$ S/cm at 160 °C (activation energy 0.57 eV) which is higher than previously reported $Li_xAl_yO_z$ films.

To better understand the enhancement of heterogeneous oxysulfides, synchrotron beamtime for pair distribution function (PDF) was applied for future analysis of the short-range order of these glass-ceramic oxysulfides. XPS measurement should be conducted at the interface of Li/SE by sputtering or on the cross-section of Li symmetric cell by FIB, to identify the stable interphase. 70 mol % Li_2CoO_2 mixed with 30 mol % SE was employed as the positive electrode in this work, which results in a huge interface resistance, and consequently large capacity loss. XPS or ToF-SIMS measurements on this interface can be very useful to explore the mechanism behind this poor electrochemical performance. Other positive electrode compositions or surface coatings could be applied to optimize the interface between SE and the positive electrode.

For the in-depth characterization of heterostructured LiON-Al_2O_3 films, a more proper sputtering strategy is expected to decrease the sputter-induced migration. Since the nitrogen dopant increases the ionic conductivity of the heterostructured LiON-Al_2O_3 films, varied content of nitrogen could be introduced to further optimize the LiON-Al_2O_3 films concerning ionic conduction. To clarify the influence of the number of heterointerfaces on ionic conductivity, LiON-Al_2O_3 films with a different number of heterointerfaces while possessing the same thicknesses of the LiON and the Al_2O_3 sublayer should be prepared for impedance measurements.

References

1. C. Pasten, J. C. Santamarina, Energy and quality of life. *Energy Policy*. **49**, 468–476 (2012).

2. J. Chow, R. J. Kopp, P. R. Portney, Energy resources and global development. *Science.* **302**, 1528–1531 (2003).

3. D. Larcher, J. M. Tarascon, Towards greener and more sustainable batteries for electrical energy storage. *Nat. Chem.* **7**, 19–29 (2015).

4. M. Armand, J.-M. Tarascon, Building better batteries. *Nature*. **451**, 652–657 (2008).

5. T. B. Reddy, *Linden's Handbook of Batteries* (McGraw-Hill Education, New York, Chicago, San Francisco, Lisbon, London, Madrid, Mexico, City Milan, New Delhi, San Juan, Seoul, Singapore, Sydney, Toronto, Fourth Edi., 2019).

6. G. Jeong, Y. U. Kim, H. Kim, Y. J. Kim, H. J. Sohn, Prospective materials and applications for Li secondary batteries. *Energy Environ. Sci.* **4**, 1986–2002 (2011).

7. T. H. Kim, J. S. Park, S. K. Chang, S. Choi, J. H. Ryu, H. K. Song, The current move of lithium ion batteries towards the next phase. *Adv. Energy Mater.* **2**, 860–872 (2012).

8. J. B. Goodenough, K. S. Park, The Li-ion rechargeable battery: A perspective. *J. Am. Chem. Soc.* **135**, 1167–1176 (2013).

9. G. Zubi, R. Dufo-López, M. Carvalho, G. Pasaoglu, The lithium-ion battery: State of the art and future perspectives. *Renew. Sustain. Energy Rev.* **89**, 292–308 (2018).

10. M. Li, J. Lu, Z. Chen, K. Amine, 30 years of lithium-ion batteries. *Adv. Mater.* **30**, 1–24 (2018).

11. T. M. Bandhauer, S. Garimella, T. F. Fuller, A critical review of thermal issues in lithium-ion batteries. *J. Electrochem. Soc.* **158**, R1–R25 (2011).

12. A. Mauger, C. M. Julien, Critical review on lithium-ion batteries: are they safe?

Sustainable? *Ionics.* **23**, 1933–1947 (2017).

13. J. Xiao, How lithium dendrites form in liquid batteries. *Science.* **366**, 426–427 (2019).

14. F. Han, J. Yue, X. Zhu, C. Wang, Suppressing Li dendrite formation in Li2S-P2S5 solid electrolyte by LiI incorporation. *Adv. Energy Mater.* **8** (2018), doi:10.1002/aenm.201703644.

15. A. Manthiram, X. Yu, S. Wang, Lithium battery chemistries enabled by solid-state electrolytes. *Nat. Rev. Mater.* **2**, 1–16 (2017).

16. E. Quartarone, P. Mustarelli, Electrolytes for solid-state lithium rechargeable batteries: Recent advances and perspectives. *Chem. Soc. Rev.* **40**, 2525–2540 (2011).

17. A. Manthiram, X. Yu, S. Wang, Lithium battery chemistries enabled by solid-state electrolytes. *Nat. Rev. Mater.* **2**, 16103 (2017).

18. F. Zheng, M. Kotobuki, S. Song, M. O. Lai, L. Lu, Review on solid electrolytes for all-solid-state lithium-ion batteries. *J. Power Sources*. **389**, 198–213 (2018).

19. M. Tatsumisago, M. Nagao, A. Hayashi, Recent development of sulfide solid electrolytes and interfacial modification for all-solid-state rechargeable lithium batteries. *J. Asian Ceram. Soc.* **1**, 17–25 (2013).

20. M. Swan, Sensor mania! the internet of things, wearable computing, objective metrics, and the quantified self 2.0. *J. Sens. Actuator Networks*. **1**, 217–253 (2012).

21. J. F. M. Oudenhoven, L. Baggetto, P. H. L. Notten, All-solid-state lithium-ion microbatteries: A review of various three-dimensional concepts. *Adv. Energy Mater.* **1**, 10–33 (2011).

22. Y. Wang, B. Liu, Q. Li, S. Cartmell, S. Ferrara, Z. D. Deng, J. Xiao, Lithium and lithium ion batteries for applications in microelectronic devices: A review. *J. Power Sources*. **286**, 330–345 (2015).

23. S. Moitzheim, B. Put, P. M. Vereecken, Advances in 3D thin-film Li-ion batteries. *Adv. Mater. Interfaces*. **6**, 1–17 (2019).

24. Y. Li, J. Qu, F. Li, Z. Qu, H. Tang, L. Liu, M. Zhu, O. G. Schmidt, Advanced architecture designs towards high-performance 3D microbatteries. *Nano Mater. Sci.* (2020), doi:10.1016/j.nanoms.2020.10.004.

25. S. Seshan, D. Schepis, *Handbook of Thin Film Deposition* (Elsevier Inc., Chennai, Fourth Edi., 2018).

26. S. M. George, Atomic layer deposition: An overview. *Chem. Rev.* **110**, 111–131 (2010).

27. R. W. Johnson, A. Hultqvist, S. F. Bent, A brief review of atomic layer deposition: From fundamentals to applications. *Mater. Today*. **17**, 236–246 (2014).

28. X. Meng, Atomic layer deposition of solid-state electrolytes for next-generation lithium-ion batteries and beyond: Opportunities and challenges. *Energy Storage Mater.* **30**, 296–328 (2020).

29. A. J. M. Mackus, J. R. Schneider, C. Macisaac, J. G. Baker, S. F. Bent, Synthesis of doped, ternary, and quaternary materials by atomic layer deposition: A review. *Chem. Mater.* **31**, 1142–1183 (2019).

30. R. E. Agbenyeke, E. A. Jung, B. K. Park, T. M. Chung, C. G. Kim, J. H. Han, Atomic layer deposition of Li_2O-Al_2O_3 thin films. *Appl. Surf. Sci.* **419**, 758–763 (2017).

31. J. Maier, Ionic conduction in space charge regions. *Prog. Solid State Chem.* **23**, 171–263 (1995).

32. J. Maier, Nano-sized mixed conductors (Aspects of nano-ionics. Part III). *Solid State Ionics*. **148**, 367–374 (2002).

33. J. Maier, Space charge regions in solid two-phase systems and their conduction contribution-I. Conductance enhancement in the system ionic conductor-'inert' phase and application on AgCl:Al_2O_3 and AgCl:SiO_2. *J. Phys. Chem. Solids*. **46**, 309–320 (1985).

34. C. Zhao, Y. Li, W. Zhang, Y. Zheng, X. Lou, B. Yu, J. Chen, Y. Chen, M. Liu, J. Wang, Heterointerface engineering for enhancing the electrochemical performance of solid oxide cells. *Energy Environ. Sci.* **13**, 53–85 (2020).

35. X. Guo, J. Maier, Ionically conducting two-dimensional heterostructures. *Adv. Mater.* **21**, 2619–2631 (2009).

36. R. C. Agrawal, R. K. Gupta, Superionic solids: composite electrolyte phase - an overview. *J. Mater. Sci.* **34**, 1131–1162 (1999).

37. Y. Xiao, Y. Wang, S. H. Bo, J. C. Kim, L. J. Miara, G. Ceder, Understanding interface stability in solid-state batteries. *Nat. Rev. Mater.* **5**, 105–126 (2020).

38. J. G. Kim, B. Son, S. Mukherjee, N. Schuppert, A. Bates, O. Kwon, M. J. Choi, H. Y. Chung, S. Park, A review of lithium and non-lithium based solid state batteries. *J. Power Sources*. **282**, 299–322 (2015).

39. N. J. Dudney, Solid-state thin-film rechargeable batteries. *Mater. Sci. Eng. B*. **116**, 245–249 (2005).

40. Z. Wu, Z. Xie, A. Yoshida, Z. Wang, X. Hao, A. Abudula, G. Guan, Utmost limits of various solid electrolytes in all-solid-state lithium batteries: A critical review. *Renew. Sustain. Energy Rev.* **109**, 367–385 (2019).

41. M. V. Reddy, C. M. Julien, A. Mauger, K. Zaghib, Sulfide and oxide inorganic solid electrolytes for all-solid-state li batteries: A review. *Nanomaterials*. **10**, 1–80 (2020).

42. M. Kotobuki, H. Munakata, K. Kanamura, Y. Sato, T. Yoshida, Compatibility of $Li_7La_3Zr_2O_{12}$ solid electrolyte to all-solid-state battery using Li metal anode. *J. Electrochem. Soc.* **157**, A1076 (2010).

43. V. Thangadurai, D. Pinzaru, S. Narayanan, A. K. Baral, Fast solid-state Li ion conducting garnet-type structure metal oxides for energy storage. *J. Phys. Chem. Lett.* **6**, 292–299 (2015).

44. V. Thangadurai, H. Kaack, W. J. F. Weppner, Novel fast lithium ion conduction in garnet-type $Li_5La_3M_2O_{12}$ (M = Nb, Ta). *J. Am. Ceram. Soc.* **86**, 437–440 (2003).

45. V. Thangadurai, W. Weppner, $Li_6ALa_2Ta_2O_{12}$ (A=Sr, Ba): Novel garnet-like oxides for fast lithium ion conduction. *Adv. Funct. Mater.* **15**, 107–112 (2005).

46. R. Murugan, V. Thangadurai, W. Weppner, Fast lithium ion conduction in garnet-type $Li_7La_3Zr_2O_{12}$. *Angew. Chemie Int. Ed.* **46**, 7778–7781 (2007).

47. J. Awaka, N. Kijima, H. Hayakawa, J. Akimoto, Synthesis and structure analysis of tetragonal $Li_7La_3Zr_2O_{12}$ with the garnet-related type structure. *J. Solid State Chem.* **182**, 2046–2052 (2009).

48. S. Kumazaki, Y. Iriyama, K. H. Kim, R. Murugan, K. Tanabe, K. Yamamoto, T. Hirayama, Z. Ogumi, High lithium ion conductive $Li_7La_3Zr_2O_{12}$ by inclusion of both Al and Si. *Electrochem. commun.* **13**, 509–512 (2011).

49. R. Murugan, S. Ramakumar, N. Janani, High conductive yttrium doped $Li_7La_3Zr_2O_{12}$ cubic lithium garnet. *Electrochem. commun.* **13**, 1373–1375 (2011).

50. H. El Shinawi, J. Janek, Stabilization of cubic lithium-stuffed garnets of the type "$Li_7La_3Zr_2O_{12}$" by addition of gallium. *J. Power Sources*. **225**, 13–19 (2013).

51. W. Gu, M. Ezbiri, R. Prasada Rao, M. Avdeev, S. Adams, Effects of penta-and trivalent dopants on structure and conductivity of $Li_7La_3Zr_2O_{12}$. *Solid State Ionics*. **274**, 100–105 (2015).

52. J. L. Allen, J. Wolfenstine, E. Rangasamy, J. Sakamoto, Effect of substitution (Ta, Al, Ga) on the conductivity of $Li_7La_3Zr_2O_{12}$. *J. Power Sources*. **206**, 315–319 (2012).

53. Y. Lu, X. Meng, J. A. Alonso, M. T. Fernández-Díaz, C. Sun, Effects of fluorine doping on structural and electrochemical properties of $Li_{6.25}Ga_{0.25}La_3Zr_2O_{12}$ as electrolytes for solid-state lithium batteries. *ACS Appl. Mater. Interfaces*. **11**, 2042–2049 (2019).

54. C. Deviannapoorani, L. Dhivya, S. Ramakumar, R. Murugan, Lithium ion transport

properties of high conductive tellurium substituted $Li_7La_3Zr_2O_{12}$ cubic lithium garnets. *J. Power Sources*. **240**, 18–25 (2013).

55. Y. Harada, T. Ishigaki, H. Kawai, J. Kuwano, Lithium ion conductivity of polycrystalline perovskite $La_{0.67-x}Li_{3x}TiO_3$ with ordered and disordered arrangements of the A-site ions. *Solid State Ionics*. **108**, 407–413 (1998).

56. Y. Inaguma, C. Liquan, M. Itoh, T. Nakamura, High ionic conductivity in lithium lanthanum titanate. *Solid State Commun.* **86**, 689–693 (1993).

57. S. Wenzel, T. Leichtweiss, D. Krüger, J. Sann, J. Janek, Interphase formation on lithium solid electrolytes - An in situ approach to study interfacial reactions by photoelectron spectroscopy. *Solid State Ionics*. **278**, 98–105 (2015).

58. H. Aono, E. Sugimoto, Y. Sadaoka, N. Imanaka, G. Adachi, Electrical property and sinterability of $LiTi_2(PO_4)_3$ mixed with lithium salt (Li_3PO_4 or Li_3BO_3). *Solid State Ionics*. **47**, 257–264 (1991).

59. A. R. West, Ionic conductivity of oxides based on Li_4SiO_4. *J. Appl. Electrochem.* **3**, 327–335 (1973).

60. P. Press, Ionic conductivity of $Li_{14}Zn(GeO_4)_4$ (LISICON). *Electrochim. Acta*. **13**, 1395–1397 (1978).

61. Y. Deng, C. Eames, B. Fleutot, R. David, J. N. Chotard, E. Suard, C. Masquelier, M. S. Islam, Enhancing the lithium ion conductivity in lithium superionic conductor (LISICON) solid electrolytes through a mixed polyanion effect. *ACS Appl. Mater. Interfaces*. **9**, 7050–7058 (2017).

62. A. K. Ivanov-Shitz, V. V. Kireev, Growth and ionic conductivity of $Li_{3+x}P_{1-x}Ge_xO_4$ (x = 0.34) single crystals. *Phys. Prop. Cryst.* **48**, 117–120 (2003).

63. G. Zhao, K. Suzuki, M. Yonemura, M. Hirayama, R. Kanno, Enhancing fast lithium ion conduction in Li_4GeO_4-Li_3PO_4 solid electrolytes. *ACS Appl. Energy Mater.* **2**, 6608–6615 (2019).

64. J. B. Goodenough, H. Y. Hong, J. A. Kafalas, Fast Na^+ - ion transport in skeleton structures*. *Mat. Res. Bull.* **I1**, 203–220 (1976).

65. V. Thangadurai, W. Weppner, Recent progress in solid oxide and lithium ion conducting electrolytes research. *Ionics.* **12**, 81–92 (2006).

66. H. Aono, E. Sugimoto, Y. Sadaoka, N. Imanaka, G. Adachi, Ionic conductivity of the lithium titanium phosphate ($Li_{1+x}M_xTi_{2-x}(PO_4)_3$, M = Al, Sc, Y, and La) Systems. *J. Electrochem. Soc.* **136**, 590–591 (1989).

67. G. Y. Adachi, N. Imanaka, H. Aono, Fast $Li^{\oplus}$ conducting ceramic electrolytes. *Adv. Mater.* **8**, 127–135 (1996).

68. C. J. Leo, B. V. R. Chowdari, G. V. S. Rao, J. L. Souquet, Lithium conducting glass ceramic with Nasicon structure. *Mater. Res. Bull.* **37**, 1419–1430 (2002).

69. R. DeWees, H. Wang, Synthesis and properties of NaSICON-type LATP and LAGP solid electrolytes. *ChemSusChem*. **12**, 3713–3725 (2019).

70. X. Xu, Z. Wen, X. Yang, L. Chen, Dense nanostructured solid electrolyte with high Li-ion conductivity by spark plasma sintering technique. *Mater. Res. Bull.* **43**, 2334–2341 (2008).

71. M. Illbeigi, A. Fazlali, M. Kazazi, A. H. Mohammadi, Effect of simultaneous addition of aluminum and chromium on the lithium ionic conductivity of $LiGe_2(PO_4)_3$ NASICON-type glass-ceramics. *Solid State Ionics*. **289**, 180–187 (2016).

72. J. K. Feng, B. G. Yan, J. C. Liu, M. O. Lai, L. Li, All solid state lithium ion rechargeable batteries using NASICON structured electrolyte. *Energy Mater. Mater. Sci. Eng. Energy Syst.* **8**, 276–279 (2013).

73. M. Tatsumisago, Glassy materials based on Li_2S for all-solid-state lithium secondary batteries. *Solid State Ionics*. **175**, 13–18 (2004).

74. M. Tachez, J. Malugani, R. Mercier, G. Robert, Ionic conductivity of and phase transition

in lithium thiophosphate Li_3PS_4. *Solid State Ionics*. **14**, 181–185 (1984).

75. K. Homma, M. Yonemura, T. Kobayashi, M. Nagao, M. Hirayama, R. Kanno, Crystal structure and phase transitions of the lithium ionic conductor Li_3PS_4. *Solid State Ionics*. **182**, 53–58 (2011).

76. Y. Seino, T. Ota, K. Takada, A. Hayashi, M. Tatsumisago, A sulphide lithium super ion conductor is superior to liquid ion conductors for use in rechargeable batteries. *Energy Environ. Sci.* **7**, 627–631 (2014).

77. A. Pradel, M. Ribes, Lithium chalcogenide conductive glasses. *Mater. Chem. Phys.* **23**, 121–142 (1989).

78. J. H. Kennedy, Ionically conductive glasses based on SiS_2. *Mater. Chem. Phys.* **23**, 29–50 (1989).

79. J. L. Souquet, E. Robinel, Glass formation and ionic conduction in the M_2S-GeS_2 (M= Li, Na, Ag) systems. *Solid State Ionics*. **4**, 317–321 (1981).

80. A. Hayashi, H. Yamashita, M. Tatsumisago, T. Minami, Characterization of Li_2S-SiS_2-Li_xMO_y (M=Si, P, Ge) amorphous solid electrolytes prepared by melt-quenching and mechanical milling. *Solid State Ionics*. **148**, 381–389 (2002).

81. J. H. Kennedy, S. Sahami, S. W. Shea, Z. Zhang, Preparation and conductivity measurements of SiS_2-Li_2S glasses doped with LiBr and LiCl. *Solid State Ionics*. **19**, 368–371 (1986).

82. J. H. Kennedy, Y. Yang, A highly conductive Li^+-glass system: (1-x)(0.4SiS_2-0.6Li_2S)-xLiI. *J. Electrochem. Soc.*, 2437–2438 (1986).

83. H. Wada, M. Menetrier, A. Levasseur, P. Hagenmuller, Preparation and ionic conductivity of new B_2S_3-Li_2S-LiI glasses. *Mat. Res. Bull.* **18**, 189–193 (1981).

84. N. Kamaya, K. Homma, Y. Yamakawa, M. Hirayama, R. Kanno, M. Yonemura, T. Kamiyama, Y. Kato, S. Hama, K. Kawamoto, A lithium superionic conductor. *Nat. Mater.*

10, 682–686 (2011).

85. J. M. Whiteley, J. H. Woo, E. Hu, K. Nam, S. Lee, Empowering the lithium metal battery through a silicon-based superionic conductor. *J. Electrochem. Soc.* **161**, 1812–1817 (2014).

86. P. Bron, S. Johansson, K. Zick, J. Schmedt auf der Guenne, S. Dehnen, B. Roling, $Li_{10}SnP_2S_{12}$: An affordable lithium superionic conductor. *J. Am. Chem. Soc.* **135**, 15694–15697 (2013).

87. P. Zhou, J. Wang, F. Cheng, F. Li, J. Chen, A solid lithium superionic conductor $Li_{11}AlP_2S_{12}$ with a thio-LISICON analogous structure†. *Chem. Commun.* **52**, 6091–6094 (2016).

88. K. Minami, A. Hayashi, S. Ujiie, M. Tatsumisago, Electrical and electrochemical properties of glass–ceramic electrolytes in the systems Li_2S–P_2S_5–P_2S_3 and Li_2S–P_2S_5–P_2O_5. *Solid State Ionics*. **192**, 122–125 (2011).

89. R. Xu, X. Xia, X. Wang, Y. Xia, J. Tu, Tailored Li_2S–P_2S_5 glass-ceramic electrolyte by MoS_2 doping, possessing high ionic conductivity for all-solid-state lithium-sulfur batteries. *J. Mater. Chem. A Mater. energy Sustain.* **5**, 2829–2834 (2017).

90. H. Deiseroth, S. Kong, H. Eckert, J. Vannahme, C. Reiner, T. Zaiß, M. Schlosser, Li_6PS_5X: A class of crystalline Li-rich solids with an unusually high Li^+ mobility†. *Angew. Chemie*. **120**, 767–770 (2008).

91. J. E. Trevey, J. R. Gilsdorf, S. W. Miller, S. Lee, Li_2S–Li_2O–P_2S_5 solid electrolyte for all-solid-state lithium batteries. *Solid State Ionics*. **214**, 25–30 (2012).

92. Ryoji Kanno, M. Murayama, Lithium ionic conductor thio-LISICON The Li_2S-GeS_2-P_2S_5 System. *J. Electrochem. Soc.* **148**, A742–A746 (2001).

93. P. R. Rayavarapu, N. Sharma, V. K. Peterson, S. Adams, Variation in structure and Li^+-ion migration in argyrodite-type Li_6PS_5X (X = Cl, Br, I) solid electrolytes. *Solid State Electrochem*. **16**, 1807–1813 (2012).

94. P. Adeli, J. D. Bazak, K. H. Park, I. Kochetkov, A. Huq, G. R. Goward, L. F. Nazar, Superionic conductor boosting solid-state diffusivity and conductivity in lithium superionic argyrodites by halide substitution. *Angew. Chemie*. **58**, 8681–8686 (2019).

95. R. P. Rao, S. Adams, Studies of lithium argyrodite solid electrolytes for all-solid-state batteries. *Phys. Status Solidi Appl. Mater. Sci.* **208**, 1804–1807 (2011).

96. S. Boulineau, M. Courty, J. Tarascon, V. Viallet, Mechanochemical synthesis of Li-argyrodite Li_6PS_5X (X = Cl, Br, I) as sulfur-based solid electrolytes for all solid state batteries application. *Solid State Ionics*. **221**, 1–5 (2012).

97. A. Hayashi, K. Noi, A. Sakuda, M. Tatsumisago, Superionic glass-ceramic electrolytes for room-temperature rechargeable sodium batteries. *Nat. Commun.* **3**, 856 (2012).

98. A. Hayashi, H. Muramatsu, T. Ohtomo, S. Hama, M. Tatsumisago, Improvement of chemical stability of Li_3PS_4 glass nanoparticles electrolytes by adding M_xO_y (M = Fe, Zn, and Bi) nanoparticles. *J. Mater. Chem. A*. **1**, 6320–6326 (2013).

99. B. Huang, X. Yao, Z. Huang, Y. Guan, Y. Jin, X. Xu, Li_3PO_4-doped $Li_7P_3S_{11}$ glass-ceramic electrolytes with enhanced lithium ion conductivities and application in all-solid-state batteries. *J. Power Sources*. **284**, 206–211 (2015).

100. S. Zhao, Z. Fu, Q. Qin, A solid-state electrolyte lithium phosphorus oxynitride film prepared by pulsed laser deposition. *Thin Solid Films*. **415**, 108–113 (2002).

101. J. B. Bates, N. J. Dudney, G. R. Gruzalski, R. A. Zuhr, A. Choudhury, C. F. Luck, Electrical properties of amorphous lithium electrolyte thin films. *Solid State Ionics*. **53**–**56**, 647–654 (1992).

102. Y. Hamon, A. Douard, F. Sabary, C. Marcel, P. Vinatier, B. Pecquenard, A. Levasseur, Influence of sputtering conditions on ionic conductivity of LiPON thin films. *Solid State Ionics*. **177**, 257–261 (2006).

103. A. C. Kozen, A. J. Pearse, C. F. Lin, M. Noked, G. W. Rubloff, Atomic layer deposition of the solid electrolyte LiPON. *Chem. Mater.* **27**, 5324–5331 (2015).

104. M. Nisula, Y. Shindo, H. Koga, M. Karppinen, Atomic layer deposition of lithium phosphorus oxynitride. *Chem. Mater.* **27**, 6987–6993 (2015).

105. A. J. Pearse, T. E. Schmitt, E. J. Fuller, F. El-Gabaly, C. F. Lin, K. Gerasopoulos, A. C. Kozen, A. A. Talin, G. Rubloff, K. E. Gregorczyk, Nanoscale solid state batteries enabled by thermal atomic layer deposition of a lithium polyphosphazene solid state electrolyte. *Chem. Mater.* **29**, 3740–3753 (2017).

106. B. Put, P. M. Vereecken, J. Meersschaut, A. Sepúlveda, A. Stesmans, Electrical characterization of ultrathin RF-sputtered LiPON layers for nanoscale batteries. *ACS Appl. Mater. Interfaces*. **8**, 7060–7069 (2016).

107. X. Yu, J. B. Bates, G. E. Jellison, F. X. Hart, A stable thin-film lithium electrolyte: lithium phosphorus oxynitride. *J. Electrochem. Soc.* **144**, 524–532 (1997).

108. K.-F. Chiu, C. C. Chen, K. M. Lin, C. C. Lo, H. C. Lin, W.-H. Ho, C. S. Jiang, Lithium phosphorus oxynitride solid-state thin-film electrolyte deposited and modified by bias sputtering and low temperature annealing. *J. Vac. Sci. Technol. A Vacuum, Surfaces, Film.* **28**, 568–572 (2010).

109. Z. Sun, L. Liu, B. Yang, Q. Li, B. Wu, J. Zhao, L. Ma, Y. Liu, H. An, Preparation and ion conduction of $Li_{1.5}Al_{0.5}Ge_{1.5}(PO_4)_3$ solid electrolyte films using radio frequency sputtering. *Solid State Ionics*. **346**, 115224 (2020).

110. H. Chen, H. Tao, X. Zhao, Q. Wu, Fabrication and ionic conductivity of amorphous Li-Al-Ti-P-O thin film. *J. Non. Cryst. Solids*. **357**, 3267–3271 (2011).

111. H. Ohta, T. Mizoguchi, N. Aoki, T. Yamamoto, A. Sabarudin, T. Umemura, Lithium-ion conducting $La_{2/3-x}Li_{3x}TiO_3$ solid electrolyte thin films with stepped and terraced surfaces. *Appl. Phys. Lett.* **100**, 173107 (2012).

112. J. K. Ahn, S. G. Yoon, Characteristics of perovskite $Li_{0.5}La_{0.5}TiO_3$ solid electrolyte thin films grown by pulsed laser deposition for rechargeable lithium microbattery. *Electrochim. Acta*. **50**, 371–374 (2004).

113. J. K. Ahn, S. G. Yoon, Characteristics of amorphous lithium lanthanum titanate electrolyte thin films grown by PLD for use in rechargeable lithium microbatteries. *Electrochem. Solid-State Lett.* **8**, 75–78 (2005).

114. S. I. Furusawa, H. Tabuchi, T. Sugiyama, S. Tao, J. T. S. Irvine, Ionic conductivity of amorphous lithium lanthanum titanate thin film. *Solid State Ionics*. **176**, 553–558 (2005).

115. T. Aaltonen, M. Alnes, O. Nilsen, L. Costelle, H. Fjellvåg, Lanthanum titanate and lithium lanthanum titanate thin films grown by atomic layer deposition. *J. Mater. Chem.* **20**, 2877–2881 (2010).

116. D. J. Kalita, S. H. Lee, K. S. Lee, D. H. Ko, Y. S. Yoon, Ionic conductivity properties of amorphous Li-La-Zr-O solid electrolyte for thin film batteries. *Solid State Ionics*. **229**, 14–19 (2012).

117. J. Tan, A. Tiwari, Fabrication and characterization of $Li_7La_3Zr_2O_{12}$ thin films for lithium ion battery. *ECS Solid State Lett.* **1**, 2012–2015 (2012).

118. H. Katsui, T. Goto, Preparation of cubic and tetragonal $Li_7La_3Zr_2O_{12}$ film by metal organic chemical vapor deposition. *Thin Solid Films*. **584**, 130–134 (2015).

119. K. Tadanaga, H. Egawa, A. Hayashi, M. Tatsumisago, J. Mosa, M. Aparicio, A. Duran, Preparation of lithium ion conductive Al-doped $Li_7La_3Zr_2O_{12}$ thin films by a sol-gel process. *J. Power Sources*. **273**, 844–847 (2015).

120. J. S. Park, L. Cheng, V. Zorba, A. Mehta, J. Cabana, G. Chen, M. M. Doeff, T. J. Richardson, J. H. Park, J. W. Son, W. S. Hong, Effects of crystallinity and impurities on the electrical conductivity of Li-La-Zr-O thin films. *Thin Solid Films*. **576**, 55–60 (2015).

121. M. Saccoccio, J. Yu, Z. Lu, S. C. T. Kwok, J. Wang, K. K. Yeung, M. M. F. Yuen, F. Ciucci, Low temperature pulsed laser deposition of garnet $Li_{6.4}La_3Zr_{1.4}Ta_{0.6}O_{12}$ films as all solid-state lithium battery electrolytes. *J. Power Sources*. **365**, 43–52 (2017).

122. S. Kim, M. Hirayama, S. Taminato, R. Kanno, Epitaxial growth and lithium ion conductivity of lithium-oxide garnet for an all solid-state battery electrolyte. *Dalt. Trans.*

42, 13112–13117 (2013).

123. S. Lobe, C. Dellen, M. Finsterbusch, H. G. Gehrke, D. Sebold, C. L. Tsai, S. Uhlenbruck, O. Guillon, Radio frequency magnetron sputtering of $Li_7La_3Zr_2O_{12}$ thin films for solid-state batteries. *J. Power Sources*. **307**, 684–689 (2016).

124. S. J. Lee, J. H. Bae, H. W. Lee, H. K. Baik, S. M. Lee, Electrical conductivity in Li-Si-P-O-N oxynitride thin-films. *J. Power Sources*. **123**, 61–64 (2003).

125. Y. Gao, W. E. Tenhaeff, Synthesis and characterization of thin film polyelectrolytes for solid-state lithium microbatteries. *J. Vac. Sci. Technol. B*. **37**, 051401 (2019).

126. T. Famprikis, J. Galipaud, O. Clemens, B. Pecquenard, F. Le Cras, Composition dependence of ionic conductivity in LiSiPO(N) thin-film electrolytes for solid-state batteries. *ACS Appl. Energy Mater.* **2**, 4782–4791 (2019).

127. B. Wang, Y. Zhao, M. N. Banis, Q. Sun, K. R. Adair, R. Li, T. K. Sham, X. Sun, Atomic layer deposition of lithium niobium oxides as potential solid-state electrolytes for lithium-ion batteries. *ACS Appl. Mater. Interfaces*. **10**, 1654–1661 (2018).

128. Y. C. Perng, J. Cho, S. Y. Sun, D. Membreno, N. Cirigliano, B. Dunn, J. P. Chang, Synthesis of ion conducting $Li_xAl_ySi_zO$ thin films by atomic layer deposition. *J. Mater. Chem. A*. **2**, 9566–9573 (2014).

129. A. Ruud, V. Miikkulainen, K. Mizohata, H. Fjellvåg, O. Nilsen, Enhanced process and composition control for atomic layer deposition with lithium trimethylsilanolate. *J. Vac. Sci. Technol. A*. **35**, 01B133 (2017).

130. D. J. Comstock, J. W. Elam, Mechanistic study of lithium aluminum oxide atomic layer deposition. *J. Phys. Chem. C*. **117**, 1677–1683 (2013).

131. J. Hämäläinen, J. Holopainen, F. Munnik, T. Hatanpää, M. Heikkilä, M. Ritala, M. Leskelä, Lithium phosphate thin films grown by atomic layer deposition. *J. Electrochem. Soc.* **159**, A259–A263 (2012).

132. J. Liu, M. N. Banis, X. Li, A. Lushington, M. Cai, R. Li, T. K. Sham, X. Sun, Atomic layer deposition of lithium tantalate solid-state electrolytes. *J. Phys. Chem. C*. **117**, 20260–20267 (2013).

133. E. Kazyak, K. H. Chen, A. L. Davis, S. Yu, A. J. Sanchez, J. Lasso, A. R. Bielinski, T. Thompson, J. Sakamoto, D. J. Siegel, N. P. Dasgupta, Atomic layer deposition and first principles modeling of glassy Li_3BO_3-Li_2CO_3 electrolytes for solid-state Li metal batteries. *J. Mater. Chem. A*. **6**, 19425–19437 (2018).

134. Y. Cao, X. Meng, J. W. Elam, Atomic layer deposition of Li_xAl_yS solid-state electrolytes for stabilizing lithium-metal anodes. *ChemElectroChem*. **3**, 858–863 (2016).

135. N. Ohta, K. Takada, M. Osada, L. Zhang, T. Sasaki, M. Watanabe, Solid electrolyte, thio-LISICON, thin film prepared by pulsed laser deposition. *J. Power Sources*. **146**, 707–710 (2005).

136. Z. Quan, M. Hirayama, D. Sato, Y. Zheng, T. A. Yano, K. Hara, K. Suzuki, M. Hara, R. Kanno, Effect of excess Li_2S on electrochemical properties of amorphous Li_3PS_4 films synthesized by pulsed laser deposition. *J. Am. Ceram. Soc.* **100**, 746–753 (2017).

137. I. Seo, S. W. Martin, Fast lithium ion conducting solid state thin-film electrolytes based on lithium thio-germanate materials. *Acta Mater.* **59**, 1839–1846 (2011).

138. S. Tanuma, C. J. Powell, D. R. Penn, Calculations of electron inelastic mean free paths. IX. Data for 41 elemental solids over the 50 eV to 30 keV range. *Surf. Interface Anal.* **43**, 689–713 (2011).

139. Thermo Scientific, K-Alpha: A new concept in XPS. *https://tools.thermofisher.com/content/sfs/brochures/D16110~.pdf*.

140. T. Terlier, Time-of-flight secondary ion mass spectroscopy. *http://simslab.rice.edu/surface-analysis-lab/teaching-activities-resources/time-of-flight-secondary-ion-mass-spectrometry/*.

141. M. Tatsumisago, S. Hama, A. Hayashi, H. Morimoto, T. Minami, New lithium ion

conducting glass-ceramics prepared from mechanochemical Li_2S-P_2S_5 glasses. *Solid State Ionics*. **154**–**155**, 635–640 (2002).

142. F. Mizuno, A. Hayashi, K. Tadanaga, M. Tatsumisago, High lithium ion conducting glass-ceramics in the system Li_2S-P_2S_5. *Solid State Ionics*. **177**, 2721–2725 (2006).

143. H. Muramatsu, A. Hayashi, T. Ohtomo, S. Hama, M. Tatsumisago, Structural change of Li_2S-P_2S_5 sulfide solid electrolytes in the atmosphere. *Solid State Ionics*. **182**, 116–119 (2011).

144. H. Muramatsu, A. Hayashi, T. Ohtomo, S. Hama, M. Tatsumisago, Structural change of Li_2S-P_2S_5 sulfide solid electrolytes in the atmosphere. *Solid State Ionics*. **182**, 116–119 (2011).

145. C. C. Liang, Conduction characteristics of the lithium iodide-aluminum oxide solid electrolytes. *J. Electrochem. Soc.* **120**, 1289–1292 (1973).

146. K. Takada, M. Osada, N. Ohta, T. Inada, A. Kajiyama, H. Sasaki, S. Kondo, M. Watanabe, T. Sasaki, Lithium ion conductive oxysulfide, Li_3PO_4-Li_3PS_4. *Solid State Ionics*. **176**, 2355–2359 (2005).

147. B. Huang, X. Yao, Z. Huang, Y. Guan, Y. Jin, X. Xu, Li_3PO_4-doped $Li_7P_3S_{11}$ glass-ceramic electrolytes with enhanced lithium ion conductivities and application in all-solid-state batteries. *J. Power Sources*. **284**, 206–211 (2015).

148. N. H. H. Phuc, T. Maeda, T. Yamamoto, H. Muto, A. Matsuda, Preparation of Li_3PS_4–Li_3PO_4 solid electrolytes by liquid-phase shaking for all-solid-state batteries. *Electron. Mater.* **2**, 39–48 (2021).

149. S. Mo, P. Lu, F. Ding, Z. Xu, J. Liu, X. Liu, Q. Xu, High-temperature performance of all-solid-state battery assembled with $95(0.7Li_2S\text{-}0.3P_2S_5)\text{-}5Li_3PO_4$ glass electrolyte. *Solid State Ionics*. **296**, 37–41 (2016).

150. J. E. Trevey, J. R. Gilsdorf, S. W. Miller, S. H. Lee, Li_2S-Li_2O-P_2S_5 solid electrolyte for all-solid-state lithium batteries. *Solid State Ionics*. **214**, 25–30 (2012).

151. Y. Tao, S. Chen, D. Liu, G. Peng, X. Yao, X. Xu, Lithium superionic conducting oxysulfide solid electrolyte with excellent stability against lithium metal for all-solid-state cells. *J. Electrochem. Soc.* **163**, A96–A101 (2016).

152. K. Minami, F. Mizuno, A. Hayashi, M. Tatsumisago, Structure and properties of the $70Li_2S\cdot(30 - x)P_2S_5\cdot xP_2O_5$ oxysulfide glasses and glass – ceramics. *J. Non. Cryst. Solids*. **354**, 370–373 (2008).

153. K. Minami, A. Hayashi, M. Tatsumisago, Electrical and electrochemical properties of the $70Li_2S\cdot(30-x)\ P_2S_5\cdot xP_2O_5$ glass-ceramic electrolytes. *Solid State Ionics*. **179**, 1282–1285 (2008).

154. A. Hayashi, H. Muramatsu, T. Ohtomo, S. Hama, M. Tatsumisago, Improved chemical stability and cyclability in Li_2S-P_2S_5-P_2O_5-ZnO composite electrolytes for all-solid-state rechargeable lithium batteries. *J. Alloys Compd.* **591**, 247–250 (2014).

155. K. L. Parry, A. G. Shard, R. D. Short, R. G. White, J. D. Whittle, A. Wright, ARXPS characterisation of plasma polymerised surface chemical gradients. *Surf. Interface Anal.* **38**, 1479–1504 (2006).

156. J. H. Scofield, Hartree-Slater subshell photoionization cross-sections at 1254 and 1487 eV. *J. Electron Spectros. Relat. Phenomena*. **8**, 129–137 (1976).

157. H. Stöffler, Deutschen Patent- und Markenamt. 10 2019 102 589.3 (2019).

158. C. Yu, L. van Eijck, S. Ganapathy, M. Wagemaker, Synthesis, structure and electrochemical performance of the argyrodite Li_6PS_5Cl solid electrolyte for Li-ion solid state batteries. *Electrochim. Acta*. **215**, 93–99 (2016).

159. F. Kubel, B. Bertheville, H. Bill, Crystal structure of dilithiumsulfide, Li_2S. *Zeitschrift für Krist.* **214**, 302 (1999).

160. A. Grzechnik, A. Vegas, K. Syassen, I. Loa, M. Hanfland, M. Jansen, Reversible antifluorite to anticotunnite phase transition in Li_2S at high pressures. *J. Solid State Chem.* **154**, 603–611 (2000).

161. M. Gardner, Infrared and Raman spectra of some phosphorus sulphides. *J. Chem. Soc. Dalt. Trans.*, 691–696 (1973).

162. J. O. Jensen, D. Zeroka, Theoretical studies of the infrared and Raman spectra of P_4S_7. *J. Mol. Struct. THEOCHEM*. **505**, 31–43 (2000).

163. E. Sarantopoulou, C. Raptis, C. Ecolivet, P. Czarnecki, J. Camacho, I. Loa, Experimental Raman scattering investigation of phonon anharmonicity effects in Li_2S. *J. Phys. Condens. Matter*. **10**, 2155–2169 (1998).

164. T. Scholz, F. Pielnhofer, R. Eger, B. V Lotsch, Lanthanide orthothiophosphates revisited: single-crystal X-ray, Raman, and DFT studies of TmPS4 and YbPS4. *Zeitschrift für Naturforsch. B*. **75**, 225–231 (2020).

165. Y. Wu, W. Bensch, Syntheses, Structures, and Spectroscopic Properties of $K_9Nd[PS_4]_4$, $K_3Nd[PS_4]_2$, $Cs_3Nd[PS_4]_2$, and $K_3Nd_3[PS_4]_4$. *Inorg. Chem.* **39**, 7523–7534 (2008).

166. C. Dietrich, D. A. Weber, S. Culver, A. Senyshyn, S. J. Sedlmaier, S. Indris, J. Janek, W. G. Zeier, Synthesis, structural characterization, and lithium ion conductivity of the lithium thiophosphate $Li_2P_2S_6$. *Inorg. Chem.* **56**, 6681–6687 (2017).

167. T. Yamada, S. Ito, R. Omoda, T. Watanabe, Y. Aihara, M. Agostini, U. Ulissi, J. Hassoun, B. Scrosati, All solid-state lithium–sulfur battery using a glass-type P_2S_5–Li_2S electrolyte: benefits on anode kinetics. *J. Electrochem. Soc.* **162**, A646–A651 (2015).

168. K. S. Andrikopoulos, A. G. Kalampounias, O. Falagara, S. N. Yannopoulos, The glassy and supercooled state of elemental sulfur: Vibrational modes, structure metastability, and polymer content. *J. Chem. Phys.* **139**, 124501 (2013).

169. C. Bischoff, K. Schuller, M. Haynes, S. W. Martin, Structural investigations of $yNa_2S + (1 - Y)PS_{5/2}$ glasses using Raman and infrared spectroscopies. *J. Non. Cryst. Solids*. **358**, 3216–3222 (2012).

170. A. R. West, F. P. Glasser, Preparation and crystal chemistry of some tetrahedral Li_3PO_4-type compounds. *J. Solid State Chem.* **4**, 20–28 (1972).

171. N. I. P. Ayu, E. Kartini, L. D. Prayogi, M. Faisal, Supardi, Crystal structure analysis of Li_3PO_4 powder prepared by wet chemical reaction and solid-state reaction by using X-ray diffraction (XRD). *Ionics.* **22**, 1051–1057 (2016).

172. H. Stöffler, T. Zinkevich, M. Yavuz, A. L. Hansen, M. Knapp, J. Bednarčík, S. Randau, F. H. Richter, J. Janek, H. Ehrenberg, S. Indris, Amorphous versus crystalline Li_3PS_4: local structural changes during synthesis and Li ion mobility. *J. Phys. Chem. C*. **123**, 10280–10290 (2019).

173. H. Eckert, Z. Zhang, J. H. Kennedy, Structural transformation of non-oxide chalcogenide glasses. The short-range order of Li_2S-P_2S_5 glasses studied by quantitative ^{31}P and $^{6,7}Li$ high-resolution solid-state NMR. *Chem. Mater.* **2**, 273–279 (1990).

174. T. M. Alam, R. K. Brow, Local structure and connectivity in lithium phosphate glasses: A solid-state ^{31}P MAS NMR and 2D exchange investigation. *J. Non. Cryst. Solids*. **223**, 1–20 (1998).

175. N. Mascaraque, J. L. G. Fierro, F. Muñoz, A. Durán, Y. Ito, Y. Hibi, R. Harada, A. Kato, A. Hayashi, M. Tatsumisago, Thio-oxynitride phosphate glass electrolytes prepared by mechanical milling. *J. Mater. Res.* **30**, 2940–2948 (2015).

176. A. Hayashi, M. Tatsumisago, T. Minami, Crystallization process of lithium oxysulfide glasses. *J. Non. Cryst. Solids*. **276**, 27–34 (2000).

177. R. K. Brow, Review: the structure of simple phosphate glasses. *J. Non. Cryst. Solids*. **263**, 1–28 (2000).

178. B. Raguž, K. Wittich, R. Glaum, Two new, metastable polymorphs of lithium pyrophosphate $Li_4P_2O_7$. *Eur. J. Inorg. Chem.* **2019**, 1688–1696 (2019).

179. P. Glatz, M. Comte, L. Montagne, B. Doumert, L. Cormier, Quantitative determination of the phosphorus environment in lithium aluminosilicate glasses using solid-state NMR techniques. *Phys. Chem. Chem. Phys.* **21**, 18370–18379 (2019).

180. L. J. Gardner, S. A. Bernal, S. A. Walling, C. L. Corkhill, J. L. Provis, N. C. Hyatt,

Characterisation of magnesium potassium phosphate cements blended with fly ash and ground granulated blast furnace slag. *Cem. Concr. Res.* **74**, 78–87 (2015).

181. A. Viani, G. Mali, P. Mácová, Investigation of amorphous and crystalline phosphates in magnesium phosphate ceramics with solid-state ^{1}H and ^{31}P NMR spectroscopy. *Ceram. Int.* **43**, 6571–6579 (2017).

182. L. Popović, B. Manoun, D. De Waal, M. K. Nieuwoudt, J. D. Comins, Raman spectroscopic study of phase transitions in Li_3PO_4. *J. Raman Spectrosc.* **34**, 77–83 (2003).

183. F. Harbach, F. Fischer, Raman Spectra and Optical Absorption Edge of Li_3PO_4 Single Crystals. *Phys. Status Solidi*. **66**, 237–245 (1974).

184. K. E. LIPINSKA-KALITA, FT infrared and laser Raman spectroscopy of amorphous and crystalline germanates. *J. Non. Cryst. Solids*. **119**, 41–48 (1990).

185. L. S. Taylor, G. Zografi, The quantitative analysis of crystallinity using FT-Raman spectroscopy. *Phamaceutical Res.* **15**, 755–761 (1998).

186. X. Wu, M. El Kazzi, C. Villevieille, Surface and morphological investigation of the electrode/electrolyte properties in an all-solid-state battery using a Li_2S-P_2S_5 solid electrolyte. *J. Electroceramics*. **38**, 207–214 (2017).

187. N. Tanibata, M. Deguchi, A. Hayashi, M. Tatsumisago, All-solid-state Na/S batteries with a Na_3PS_4 electrolyte operating at room temperature. *Chem. Mater.* **29**, 5232–5238 (2017).

188. W. E. Morgan, J. R. Van Wazer, W. J. Stec, Inner-orbital photoelectron spectroscopy of the alkali metal halides, perchlorates, phosphates, and pyrophosphates. *J. Am. Chem. Soc.* **25**, 751–755 (1972).

189. M. Wu, J. Jin, Z. Wen, Influence of a surface modified Li anode on the electrochemical performance of Li-S batteries. *RSC Adv.* **6**, 40270–40276 (2016).

190. E. Umeshbabu, B. Zheng, Y. Yang, Recent progress in all-solid-state lithium−sulfur

batteries using high Li-ion conductive solid electrolytes. *Electrochem. Energy Rev.* **2**, 199–230 (2019).

191. Y. Xiao, Y. Wang, S. H. Bo, J. C. Kim, L. J. Miara, G. Ceder, Understanding interface stability in solid-state batteries. *Nat. Rev. Mater.* **5**, 105–126 (2020).

192. W. D. Richards, L. J. Miara, Y. Wang, J. C. Kim, G. Ceder, Interface stability in solid-state batteries. *Chem. Mater.* **28**, 266–273 (2016).

193. N. D. Lepley, N. A. W. Holzwarth, Y. A. Du, Structures, Li^+ mobilities, and interfacial properties of solid electrolytes Li_3PS_4 and Li_3PO_4 from first principles. *Phys. Rev. B - Condens. Matter Mater. Phys.* **88**, 21–23 (2013).

194. Y. Lu, S. Gu, X. Hong, K. Rui, X. Huang, J. Jin, C. Chen, J. Yang, Z. Wen, Pre-modified Li_3PS_4 based interphase for lithium anode towards high-performance Li-S battery. *Energy Storage Mater.* **11**, 16–23 (2018).

195. S. Wenzel, D. A. Weber, T. Leichtweiss, M. R. Busche, J. Sann, J. Janek, Interphase formation and degradation of charge transfer kinetics between a lithium metal anode and highly crystalline $Li_7P_3S_{11}$ solid electrolyte. *Solid State Ionics*. **286**, 24–33 (2016).

196. Y. Zhu, X. He, Y. Mo, Origin of outstanding stability in the lithium solid electrolyte materials: insights from thermodynamic analyses based on first-principles calculations. *ACS Appl. Mater. Interfaces*. **7**, 23685–23693 (2015).

197. J. Li, W. Liu, X. Zhang, Y. Ma, Y. Wei, Z. Fu, J. Li, Y. Yan, Heat treatment effects in oxygen-doped β-Li_3PS_4 solid electrolyte prepared by wet chemistry method. *J. Solid State Electrochem.* **25**, 1259–1269 (2021).

198. T. Ohtomo, A. Hayashi, M. Tatsumisago, K. Kawamoto, Characteristics of the Li_2O-Li_2S-P_2S_5 glasses synthesized by the two-step mechanical milling. *J. Non. Cryst. Solids*. **364**, 57–61 (2013).

199. K. Minami, A. Hayashi, S. Ujiie, M. Tatsumisago, Electrical and electrochemical properties of glass – ceramic electrolytes in the systems Li_2S–P_2S_5–P_2S_3 and Li_2S–P_2S_5–

P_2O_5. *Solid State Ionics*. **192**, 122–125 (2011).

200. Y. Tao, J. E. Soc, Y. Tao, S. Chen, D. Liu, G. Peng, X. Yao, X. Xu, Lithium superionic conducting oxysulfide solid electrolyte with excellent stability against lithium metal for all-solid-state cells. *J. Electrochem. Soc.* **163**, A96–A101 (2016).

201. I. Sasaki, K. Honda, T. Asano, Y. Ito, T. Komori, J. Hibino, Enhancement of the rate capabilities for all-solid-state batteries through the surface oxidation of sulfide solid electrolytes. *Solid State Ionics*. **347**, 115249 (2020).

202. T. Ohtomo, F. Mizuno, A. Hayashi, K. Tadanaga, M. Tatsumisago, Electrical and electrochemical properties of Li_2S-P_2S_5-P_2O_5 glass-ceramic electrolytes. *J. Power Sources*. **146**, 715–718 (2005).

203. P. Lu, F. Ding, Z. Xu, J. Liu, X. Liu, Q. Xu, Study on (100-x)(70Li_2S-30P_2S_5)-xLi_2ZrO_3 glass-ceramic electrolyte for all-solid-state lithium-ion batteries. *J. Power Sources*. **356**, 163–171 (2017).

204. B. Kumar, S. Nellutla, J. S. Thokchom, C. Chen, Ionic conduction through heterogeneous solids: Delineation of the blocking and space charge effects. *J. Power Sources*. **160**, 1329–1335 (2006).

205. J. S. Thokchom, C. Chen, K. M. Abraham, B. Kumar, High conductivity electrolytes in the PEO_x : $LiN(SO_2CF_2CF_3)_2$ -Al_2O_3 system. *Solid State Ionics*. **176**, 1887–1893 (2005).

206. X. Guo, J. Maier, Grain boundary blocking effect in zirconia: A Schottky barrier analysis. *J. Electrochem. Soc.* **148**, E121–E126 (2001).

207. X. Guo, W. Sigle, J. Maier, Blocking grain boundaries in yttria-doped and undoped ceria ceramics of high purity. *J. Am. Ceram. Soc.* **86**, 77–87 (2003).

208. S. Chen, D. Xie, G. Liu, J. P. Mwizerwa, Q. Zhang, Y. Zhao, X. Xu, X. Yao, Sulfide solid electrolytes for all-solid-state lithium batteries: Structure, conductivity, stability and application. *Energy Storage Mater.* **14**, 58–74 (2018).

209. X. Wang, R. Xiao, H. Li, L. Chen, Oxygen-driven transition from two-dimensional to three-dimensional transport behaviour in β-Li_3PS_4 electrolyte. *Phys. Chem. Chem. Phys.* **18**, 21269–21277 (2016).

210. R. Koerver, I. Aygün, T. Leichtweiß, C. Dietrich, W. Zhang, J. O. Binder, P. Hartmann, W. G. Zeier, J. Janek, Capacity fade in solid-state batteries: Interphase formation and chemomechanical processes in nickel-rich layered oxide cathodes and lithium thiophosphate solid electrolytes. *Chem. Mater.* **29**, 5574–5582 (2017).

211. W. Zhang, D. A. Weber, H. Weigand, T. Arlt, I. Manke, D. Schröder, R. Koerver, T. Leichtweiss, P. Hartmann, W. G. Zeier, J. Janek, Interfacial processes and influence of composite cathode microstructure controlling the performance of all-solid-state lithium batteries. *ACS Appl. Mater. Interfaces*. **9**, 17835–17845 (2017).

212. G. Oh, M. Hirayama, O. Kwon, K. Suzuki, R. Kanno, Bulk-type all aolid-state batteries with 5 V class $LiNi_{0.5}Mn_{1.5}O_4$ cathode and $Li_{10}GeP_2S_{12}$ solid electrolyte. *Chem. Mater.* **28**, 2634–2640 (2016).

213. T. Ohtomo, A. Hayashi, M. Tatsumisago, Y. Tsuchida, S. Hama, K. Kawamoto, All-solid-state lithium secondary batteries using the $75Li_2S{\cdot}25P_2S_5$ glass and the $70Li_2S{\cdot}30P_2S_5$ glass-ceramic as solid electrolytes. *J. Power Sources*. **233**, 231–235 (2013).

214. J. Lau, R. H. DeBlock, D. M. Butts, D. S. Ashby, C. S. Choi, B. S. Dunn, Sulfide solid electrolytes for lithium battery applications. *Adv. Energy Mater.* **8**, 1800933 (2018).

215. A. Sakuda, A. Hayashi, M. Tatsumisago, Interfacial observation between $LiCoO_2$ electrode and Li_2S-P_2S_5 solid electrolytes of all-solid-state lithium secondary batteries using transmission electron microscopy. *Chem. Mater.* **22**, 949–956 (2010).

216. H. Kitaura, A. Hayashi, K. Tadanaga, M. Tatsumisago, Electrochemical performance of all-solid-state lithium secondary batteries with Li-Ni-Co-Mn oxide positive electrodes. *Electrochim. Acta*. **55**, 8821–8828 (2010).

217. N. Ohta, K. Takada, I. Sakaguchi, L. Zhang, R. Ma, K. Fukuda, M. Osada, T. Sasaki, $LiNbO_3$-

coated $LiCoO_2$ as cathode material for all solid-state lithium secondary batteries Narumi. *Electrochem. commun.* **9**, 1486–1490 (2007).

218. N. Ohta, K. Takada, L. Zhang, R. Ma, M. Osada, T. Sasaki, Enhancement of the high-rate capability of solid-state lithium batteries by nanoscale interfacial modification. *Adv. Mater.* **18**, 2226–2229 (2006).

219. K. Takada, N. Ohta, L. Zhang, X. Xu, B. T. Hang, T. Ohnishi, M. Osada, T. Sasaki, Interfacial phenomena in solid-state lithium battery with sulfide solid electrolyte. *Solid State Ionics*. **225**, 594–597 (2012).

220. J. Haruyama, K. Sodeyama, Y. Tateyama, Cation mixing properties toward Co diffusion at the $LiCoO_2$ cathode/ sulfide electrolyte interface in a solid-state battery. *ACS Appl. Mater. Interfaces*. **9**, 286–292 (2017).

221. M. Tatsumisago, F. Mizuno, A. Hayashi, All-solid-state lithium secondary batteries using sulfide-based glass-ceramic electrolytes. *J. Power Sources*. **159**, 193–199 (2006).

222. H. Li, T. Zhang, Z. Yang, Y. Shi, Q. Zhuang, Y. Cui, Electrochemical impedance spectroscopy study on using $Li_{10}GeP_2S_{12}$ electrolyte for all-solid-state lithium batteries. *Int. J. Electrochem. Sci.* **16**, 1–13 (2021).

223. R. C. Xu, X. H. Xia, X. L. Wang, Y. Xia, J. P. Tu, Tailored Li_2S-P_2S_5 glass-ceramic electrolyte by MoS_2 doping, possessing high ionic conductivity for all-solid-state lithium-sulfur batteries. *J. Mater. Chem. A*. **5**, 2829–2834 (2017).

224. M. Roberts, P. Johns, J. Owen, D. Brandell, K. Edstrom, G. El Enany, C. Guery, D. Golodnitsky, M. Lacey, C. Lecoeur, H. Mazor, E. Peled, E. Perre, M. M. Shaijumon, P. Simon, P. L. Taberna, 3D lithium ion batteries - From fundamentals to fabrication. *J. Mater. Chem.* **21**, 9876–9890 (2011).

225. R. W. Johnson, A. Hultqvist, S. F. Bent, A brief review of atomic layer deposition: From fundamentals to applications. *Mater. Today*. **17**, 236–246 (2014).

226. V. Miikkulainen, M. Leskelä, M. Ritala, R. L. Puurunen, Crystallinity of inorganic films

grown by atomic layer deposition: Overview and general trends. *J. Appl. Phys.* **113** (2013), doi:10.1063/1.4757907.

227. X. Meng, X. Q. Yang, X. Sun, Emerging applications of atomic layer deposition for lithium-ion battery studies. *Adv. Mater.* **24**, 3589–3615 (2012).

228. O. Tiurin, Y. Ein-Eli, A critical review: The impact of the battery electrode material substrate on the composition and properties of atomic layer deposition (ALD) coatings. *Adv. Mater. Interfaces*. **6**, 1–23 (2019).

229. M. Putkonen, T. Aaltonen, M. Alnes, T. Sajavaara, O. Nilsen, H. Fjellvåg, Atomic layer deposition of lithium containing thin films. *J. Mater. Chem.* **19**, 8767–8771 (2009).

230. X. Meng, Atomic layer deposition of solid-state electrolytes for next-generation lithium-ion batteries and beyond: Opportunities and challenges. *Energy Storage Mater.* **30**, 296–328 (2020).

231. V. Miikkulainen, O. Nilsen, H. Li, S. W. King, M. Laitinen, T. Sajavaara, H. Fjellvåg, Atomic layer deposited lithium aluminum oxide: (In)dependency of film properties from pulsing sequence. *J. Vac. Sci. Technol. A*. **33**, 01A101 (2015).

232. Y. Hu, A. Ruud, V. Miikkulainen, T. Norby, O. Nilsen, H. Fjellvåg, Electrical characterization of amorphous $LiAlO_2$ thin films deposited by atomic layer deposition. *RSC Adv.* **6**, 60479–60486 (2016).

233. J. S. Park, X. Meng, J. W. Elam, S. Hao, C. Wolverton, C. Kim, J. Cabana, Ultrathin lithium-ion conducting coatings for increased interfacial stability in high voltage lithium-ion batteries. *Chem. Mater.* **26**, 3128–3134 (2014).

234. A. C. Kozen, A. J. Pearse, C. F. Lin, M. A. Schroeder, M. Noked, S. B. Lee, G. W. Rubloff, Atomic layer deposition and in situ characterization of ultraclean lithium oxide and lithium hydroxide. *J. Phys. Chem. C*. **118**, 27749–27753 (2014).

235. N. Sata, K. Eberman, K. Eberl, J. Maier, Mesoscopic fast ion conduction in nanometre-scale planar heterostructures. *Nature*. **408**, 946–949 (2000).

236. N. Sata, N. Y. Jin-Phillipp, K. Eberl, J. Maier, Enhanced ionic conductivity and mesoscopic size effects in heterostructures of BaF_2 and CaF_2. *Solid State Ionics*. **154**–**155**, 497–502 (2002).

237. Y. Su, J. Falgenhauer, A. Polity, T. Leichtweiß, A. Kronenberger, J. Obel, S. Zhou, D. Schlettwein, J. Janek, B. K. Meyer, LiPON thin films with high nitrogen content for application in lithium batteries and electrochromic devices prepared by RF magnetron sputtering. *Solid State Ionics*. **282**, 63–69 (2015).

238. J. D. Lacoste, A. Zakutayev, L. Fei, A review on lithium phosphorus oxynitride. *J. Phys. Chem. C*. **125**, 3651–3667 (2021).

239. B. Fleutot, B. Pecquenard, H. Martinez, M. Letellier, A. Levasseur, Investigation of the local structure of LiPON thin films to better understand the role of nitrogen on their performance. *Solid State Ionics*. **186**, 29–36 (2011).

240. K. Nagata, A. Ogura, I. Hirosawa, T. Suwa, A. Teramoto, T. Hattori, T. Ohmi, Structural analyses of thin SiO_2 films formed by thermal oxidation of atomically flat Si surface by using synchrotron radiation X-ray characterization. *ECS J. Solid State Sci. Technol.* **4**, N96–N98 (2015).

241. D. T. Dekadjevi, C. Wiemer, S. Spiga, S. Ferrari, M. Fanciulli, G. Pavia, A. Gibaud, Monitoring the formation of Sb nanocrystals in SiO_2 by grazing incidence x-ray techniques. *Appl. Phys. Lett.* **83**, 2148–2150 (2003).

242. E. Witt, S. Nakhal, C. V. Chandran, M. Lerch, P. Heitjans, NMR and impedance spectroscopy studies on lithium ion diffusion in microcrystalline γ-$LiAlO_2$. *Zeitschrift fur Phys. Chemie*. **229**, 1327–1339 (2015).

243. M. H. Lee, C. F. Cheng, V. Heine, J. Klinowski, Distribution of tetrahedral and octahedral Al sites in gamma alumina. *Chem. Phys. Lett.* **265**, 673–676 (1997).

244. X. Dou, Y. Li, D. Mohan, C. U. Pittman, M. Hu, A property-performance correlation and mass transfer study of As(v) adsorption on three mesoporous aluminas. *RSC Adv.* **6**,

80630–80639 (2016).

245. V. P. Isupov, O. A. Kharlamova, L. E. Chupakhina, M. R. Sharafutdinov, D. F. Khabibulin, O. B. Lapina, Mechanochemical synthesis of γ-$LiAlO_2$ studied by ^{6}Li and ^{27}Al NMR and synchrotron X-ray diffraction. *Inorg. Mater.* **47**, 763–767 (2011).

246. S. K. Lee, S. Y. Park, Y. S. Yi, J. Moon, Structure and disorder in amorphous alumina thin films: Insights from high-resolution solid-state NMR. *J. Phys. Chem. C*. **114**, 13890–13894 (2010).

247. N. I. Kato, Reducing focused ion beam damage to transmission electron microscopy samples. *J. Electron Microsc. (Tokyo).* **53**, 451–458 (2004).

248. N. D. Bassim, B. T. De Gregorio, a. L. D. Kilcoyne, K. Scott, T. Chou, S. Wirick, G. Cody, R. M. Stroud, Minimizing damage during FIB sample preparation of soft materials. *J. Microsc.* **245**, 288–301 (2012).

249. S. Rubanov, P. R. Munroe, Investigation of the structure of damage layers in TEM samples prepared using a focused ion beam. *J. Mater. Sci. Lett.* **20**, 1181–1183 (2001).

250. J. Mayer, L. a Giannuzzi, T. Kamino, J. Michael, TEM sample preparation and damage. *MRS Bull.* **32**, 400–407 (2007).

251. A. Lugstein, B. Basnar, E. Bertagnolli, Study of focused ion beam response of GaAs in the nanoscale regime. *J. Vac. Sci. Technol. B*. **20**, 2238–2242 (2002).

252. D. Mao, C. Lu, N. Winograd, A. Wucher, Molecular depth profiling by wedged crater beveling. *Anal. Chem.* **83**, 6410–6417 (2011).

253. D. Mao, A. Wucher, N. Winograd, Molecular depth profiling with cluster secondary ion mass spectrometry and wedges. *Anal. Chem.* **82**, 57–60 (2010).

254. M. Kim, K. M. Kang, Y. Wang, H. H. Park, N-doped Al_2O_3 thin films deposited by atomic layer deposition. *Thin Solid Films*. **660**, 657–662 (2018).

255. L. G. Wang, X. Qian, Y. Q. Cao, Z. Y. Cao, G. Y. Fang, A. D. Li, D. Wu, Excellent resistive switching properties of atomic layer-deposited $Al_2O_3/HfO_2/Al_2O_3$ trilayer structures for non-volatile memory applications. *Nanoscale Res. Lett.* **10**, 135 (2015).

256. K. P. C. Yao, D. G. Kwabi, R. A. Quinlan, A. N. Mansour, A. Grimaud, Y.-L. Lee, Y.-C. Lu, Y. Shao-Horn, Thermal stability of Li_2O_2 and Li_2O for Li-air batteries: In situ XRD and XPS studies. *J. Electrochem. Soc.* **160**, A824–A831 (2013).

257. Y. J. Zhang, W. Wang, H. Tang, W. Q. Bai, X. Ge, X. L. Wang, C. D. Gu, J. P. Tu, An ex-situ nitridation route to synthesize Li_3N-modified Li anodes for lithium secondary batteries. *J. Power Sources*. **277**, 304–311 (2015).

258. D. A. Zatsepin, P. MacK, A. E. Wright, B. Schmidt, H. J. Fitting, XPS analysis and valence band structure of a low-dimensional SiO_2/Si system after Si^+ ion implantation. *Phys. Status Solidi Appl. Mater. Sci.* **208**, 1658–1661 (2011).

259. M. Wang, J. Han, Y. Hu, R. Guo, Mesoporous C, N-codoped TiO_2 hybrid shells with enhanced visible light photocatalytic performance. *RSC Adv.* **7**, 15513–15520 (2017).

260. Y. Zou, J. W. Shi, D. Ma, Z. Fan, C. He, L. Cheng, D. Sun, J. Li, Z. Wang, C. Niu, Efficient spatial charge separation and transfer in ultrathin g-C_3N_4 nanosheets modified with Cu_2MoS_4 as a noble metal-free co-catalyst for superior visible light-driven photocatalytic water splitting. *Catal. Sci. Technol.* **8**, 3883–3893 (2018).

261. P. K. Nayak, J. A. Caraveo-Frescas, Z. Wang, M. N. Hedhili, Q. X. Wang, H. N. Alshareef, Thin film complementary metal oxide semiconductor (CMOS) device using a single-step deposition of the channel layer. *Sci. Rep.* **4**, 1–7 (2014).

262. L. Sygellou, V. Gianneta, N. Xanthopoulos, D. Skarlatos, S. Georga, C. Krontiras, S. Ladas, S. Kennou, ZrO_2 and Al_2O_3 thin films on Ge(100) grown by ALD: An XPS investigation. *Surf. Sci. Spectra*. **18**, 58–67 (2011).

263. J. Garcia-Barriocanal, A. Rivera-Calzada, M. Varela, Z. Sefrioui, E. Iborra, C. Leon, S. J. Pennycook, J. Santamaria, Colossal ionic conductivity at interfaces of epitaxial

ZrO_2:Y_2O_3/$SrTiO_3$ heterostructures. *Science.* **321**, 676–680 (2008).

264. F. Shin-Ichi, S. Satoshi, S. Kaduhiro, T. Hitoshi, Preparation and ionic conductivity of β-$LiAlSiO_4$ thin film. *Solid State Ionics*. **167**, 325–329 (2004).

265. S. ichi Furusawa, T. Kasahara, A. Kamiyama, Fabrication and ionic conductivity of Li_2SiO_3 thin film. *Solid State Ionics*. **180**, 649–653 (2009).

266. S. ichi Furusawa, A. Kamiyama, T. Tsurui, Fabrication and ionic conductivity of amorphous lithium meta-silicate thin film. *Solid State Ionics*. **179**, 536–542 (2008).

267. I. Kosacki, C. M. Rouleau, P. F. Becher, J. Bentley, D. H. Lowndes, Nanoscale effects on the ionic conductivity in highly textured YSZ thin films. *Solid State Ionics*. **176**, 1319–1326 (2005).

268. S. Azad, O. A. Marina, C. M. Wang, L. Saraf, V. Shutthanandan, D. E. McCready, A. El-Azab, J. E. Jaffe, M. H. Engelhard, C. H. F. Peden, S. Thevuthasan, Nanoscale effects on ion conductance of layer-by-layer structures of gadolinia-doped ceria and zirconia. *Appl. Phys. Lett.* **86**, 1–3 (2005).

269. E. Fabbri, D. Pergolesi, E. Traversa, Ionic conductivity in oxide heterostructures: The role of interfaces. *Sci. Technol. Adv. Mater.* **11**, 054503 (2010).

270. D. Pergolesi, E. Gilardi, E. Fabbri, V. Roddatis, G. F. Harrington, T. Lippert, J. A. Kilner, E. Traversa, Interface effects on the ionic conductivity of doped ceria-yttria-stabilized zirconia heterostructures. *ACS Appl. Mater. Interfaces*. **10**, 14160–14169 (2018).

271. I. Kosacki, C. M. Rouleau, P. F. Becher, J. Bentley, D. H. Lowndes, Surface/interface-related conductivity in nanometer thick YSZ films. *Electrochem. Solid-State Lett.* **7**, 459–462 (2004).

Appendix

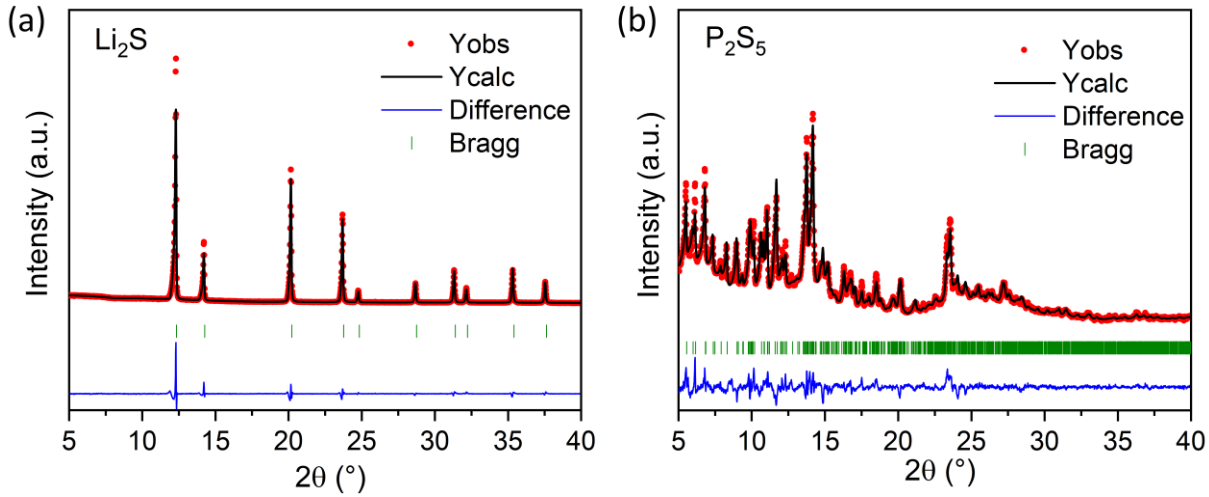

Figure A 1: Rietveld refinement from X-ray powder diffraction data of starting materials of Li_2S (a) and P_2S_5 (b).

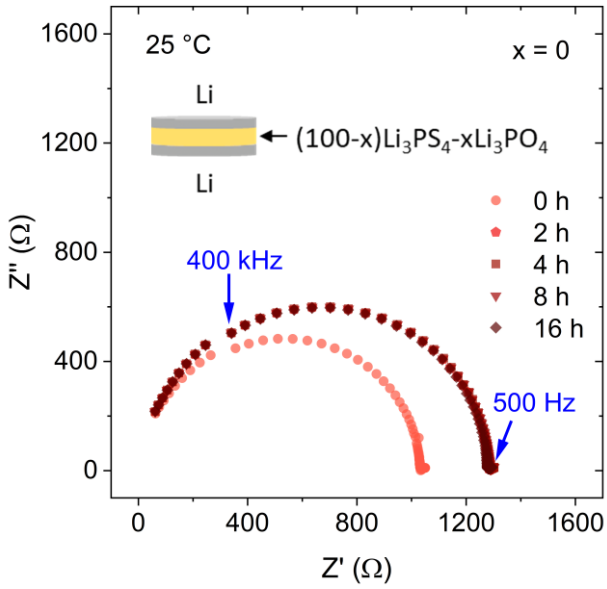

Figure A 2: Evolution of the impedance response of symmetric Li/(100 -x)Li_3PS_4-xLi_3PO_4 /Li cells (x = 0) at 25 °C as a function of time.

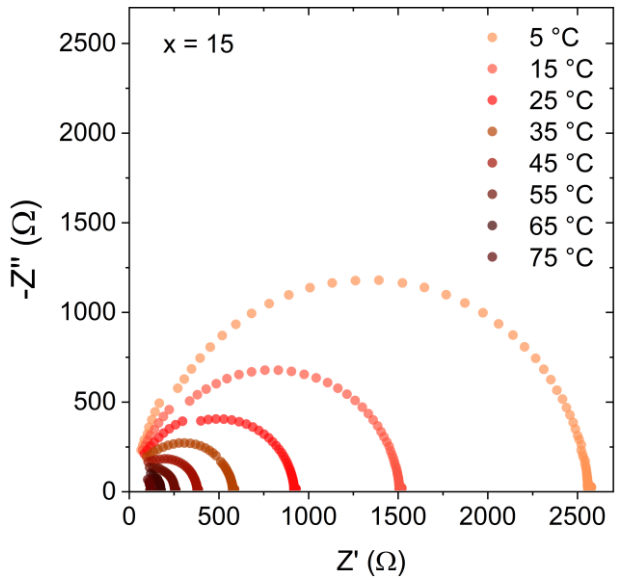

Figure A 3: Nyquist plots of symmetric Li/80Li_3PS_4-20Li_3PO_4/Li cell from 5 °C to 75 °C.

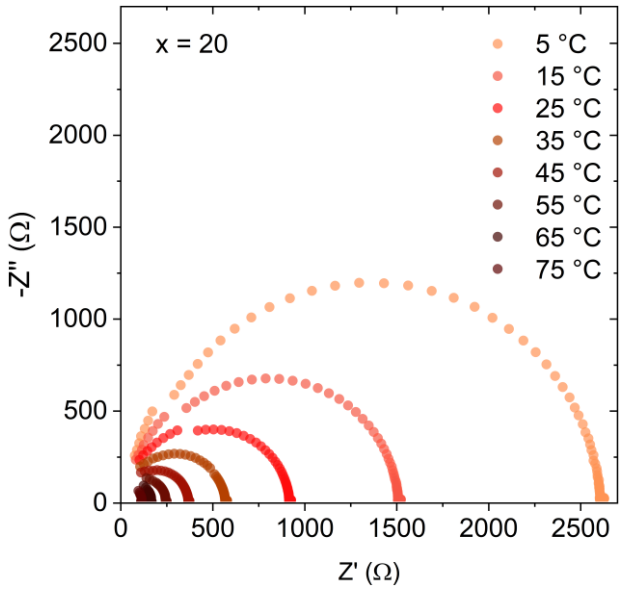

Figure A 4: Nyquist plots of symmetric Li/85Li_3PS_4-15Li_3PO_4/Li cell from 5 °C to 75 °C.

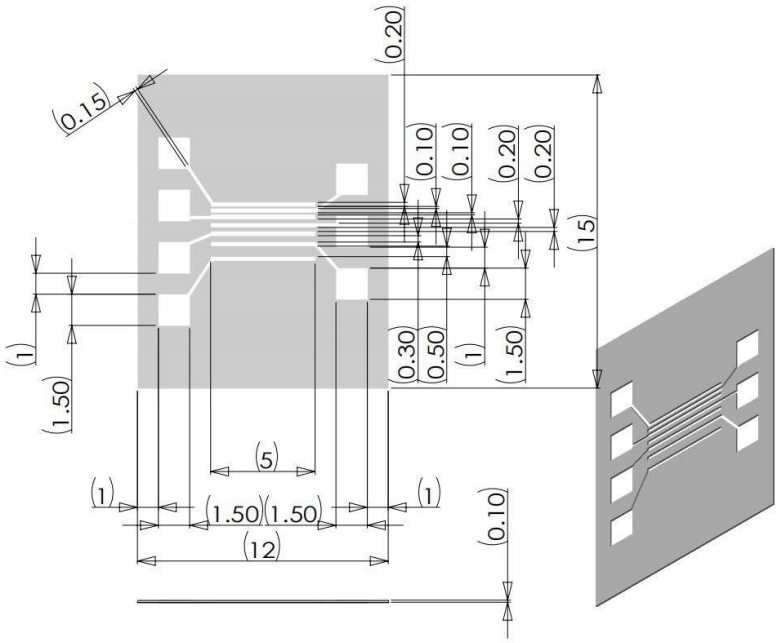

Figure A 5: Mask for gold electrode evaporation (dimension in µm).

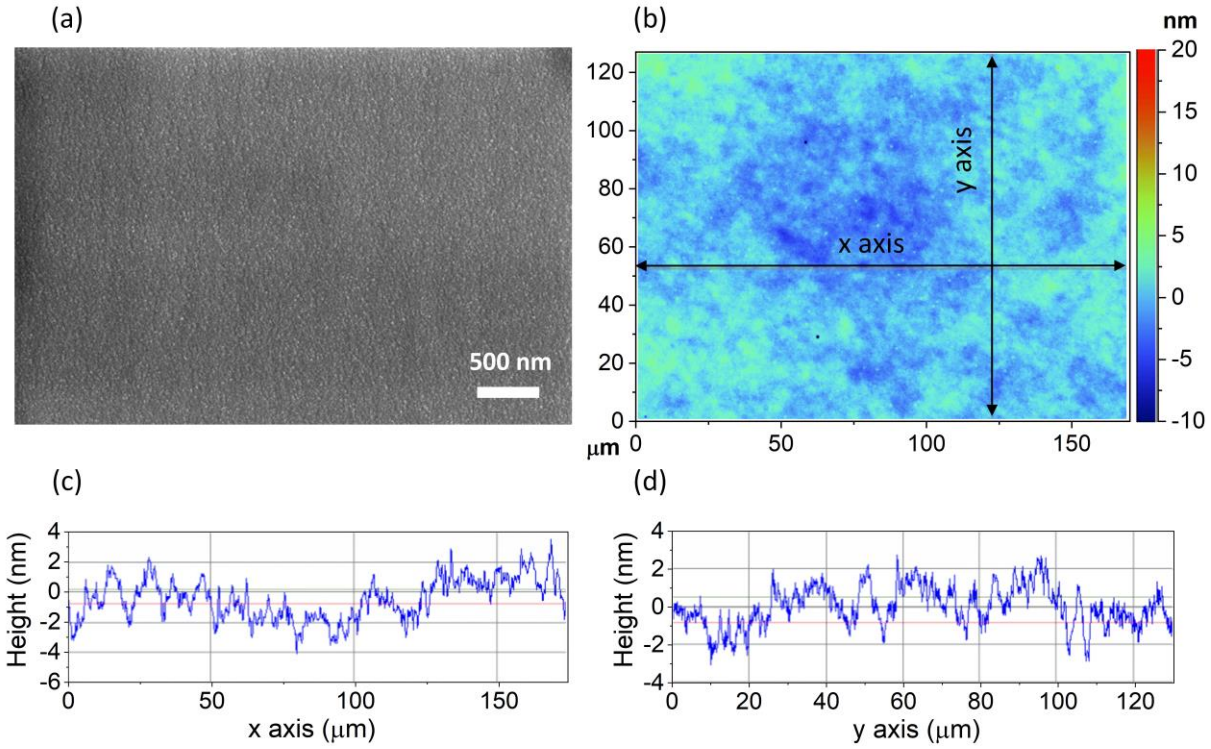

Figure A 6: (a) SEM image of the (75LiON-10Al_2O_3)x08 film; (b) surface map of the (75LiON-10Al_2O_3)x08 film obtained by WLI; cross-sectional profiles of the x-axis (c) and y-axis (d), as marked in (b).

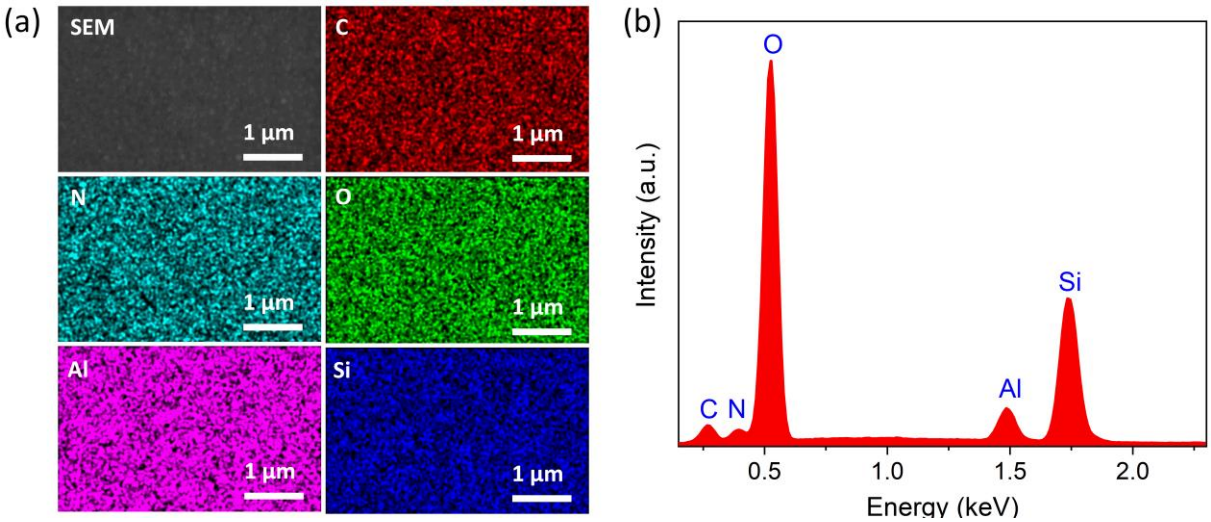

Figure A 7: (a) SEM image and corresponding EDX mappings (C, N, O, Al, Si) of the (75LiON-10Al_2O_3)x08 film; (b) EDX spectrum of the (75LiON-10Al_2O_3)x08 film.

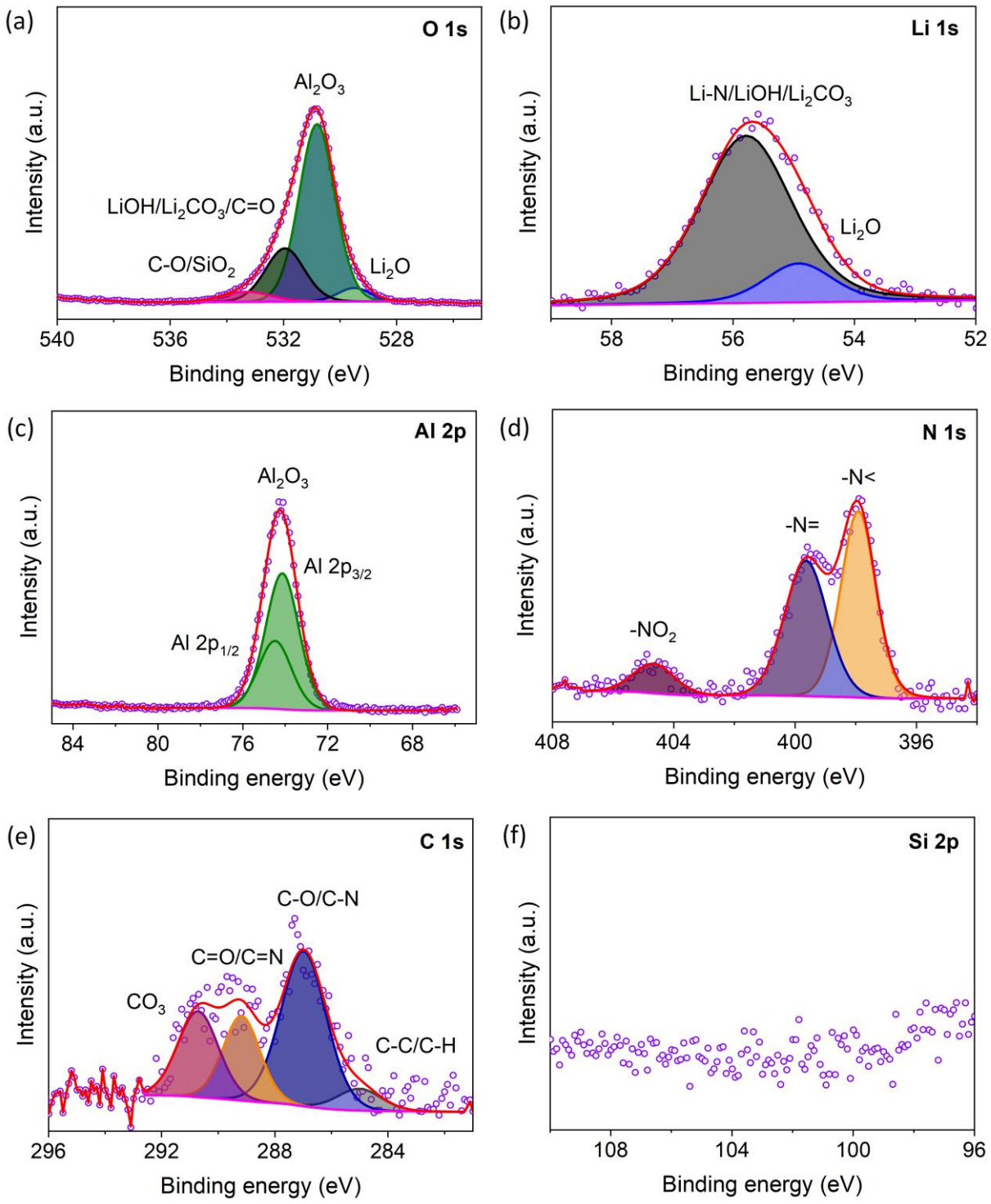

Figure A 8: Fitted XPS spectra of the (75LiON-10Al_2O_3)x08 film after 150s etching: (a) O 1s, (b) Al 2p, (c) Li 1s, (d) C 1s, (e) N 1s, (f) Si 2p.

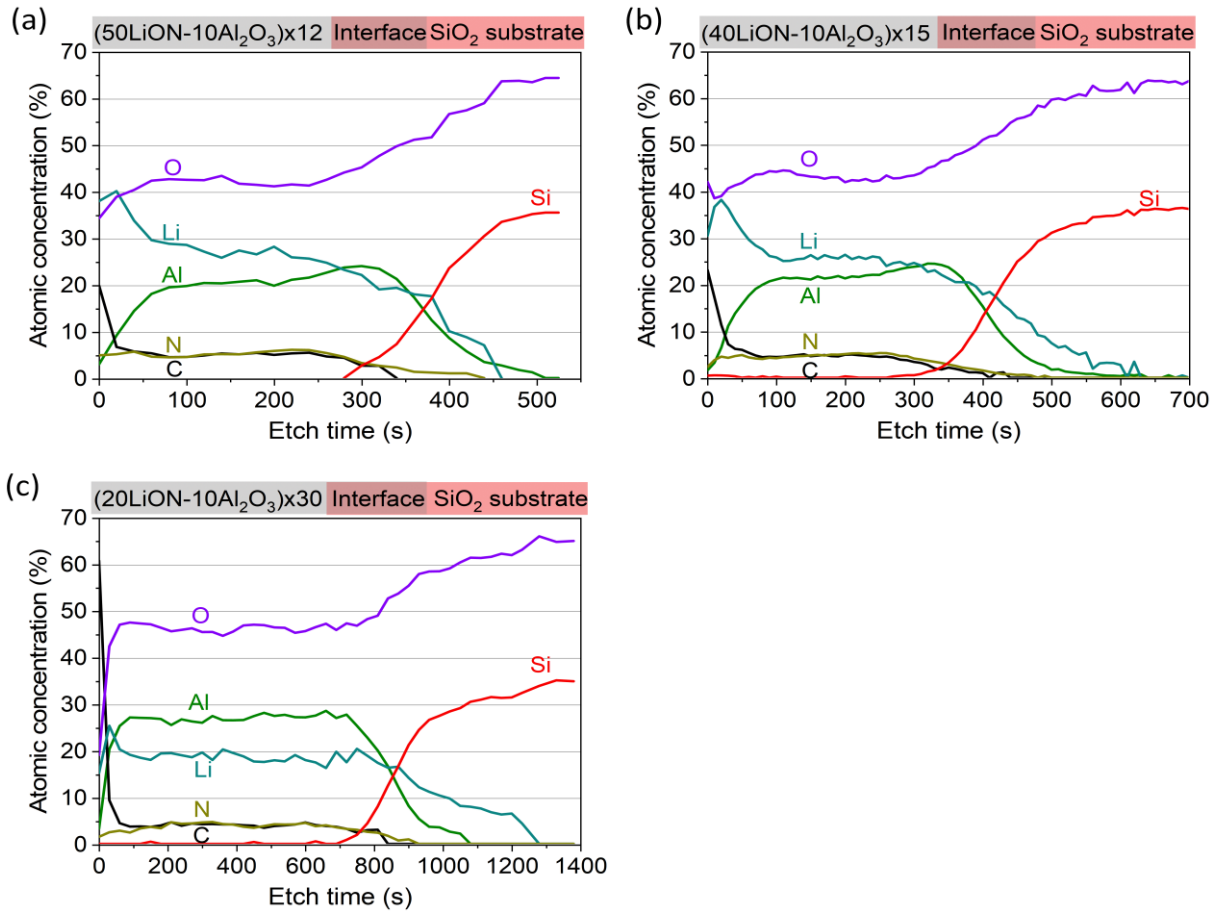

Figure A 9: XPS sputter depth profiles of (50LiON-10Al_2O_3)x12 film (a), (40LiON-10Al_2O_3)x15 film (b), and the (20LiON-10Al_2O_3)x30 film (c).

Table S 1: EIS fitting results of 600LiON, (20LiON-20Al_2O_3)x20, and (75LiON-10Al_2O_3)x08 at 160 °C:

Sample	R (Ω)	Q_1	α_1	Q_2	α_2
600LiON	3.8×10^{7}	5.5×10^{-10}	0.93	3.4×10^{-8}	0.24
(20LiON-20Al_2O_3)x20	1.7×10^{7}	2.3×10^{-10}	0.97	4.5×10^{-8}	0.22
(75LiON-10Al_2O_3)x08	1.5×10^{7}	6.5×10^{-10}	0.89	6.7×10^{-8}	0.29

List of Abbreviations

2D	Two-dimensional
3D	Three-dimensional
AC/DC	Alternating current/direct current
ALD	Atomic layer deposition
(AR)XPS	(Angle-resolved) X-ray photoelectron spectroscopy
ASSBs	All-solid-state batteries
CPE	Constant phase element
CV	Cyclic voltammetry
EDX	Energy-dispersive x-ray spectroscopy
EIS	Electrochemical impedance spectroscopy
FWHM	Full width half maximum
(GI)XRD	(Grazing incidence) X-ray diffraction
LIBs	Lithium-ion batteries
LiO^tBu	Lithium tert-butoxide
MAS NMR	Magic-angle spinning nuclear magnetic resonance spectroscopy
ppm	Parts per million
RF	Radiofrequency
RT	Room temperature
SEM	Scanning electron microscopy
SEs	Solid electrolytes
TEM	Transmission electron microscopy
TFBs	Thin-film batteries
TMA	Trimethylaluminum
ToF-SIMS	Time-of-flight secondary ion mass spectrometry
WLI	White light interferometry

List of Figures

List of Tables

Publications

1. **Xianlin Luo**, Andy Fiedler, Raheleh Azmi, Wangqiong Xu, Rong Huang, Holger Geßwein, Julia Maibach, Michael Bruns, Sylvio Indris, Helmut Ehrenberg, Xiangyang Kong, Enhancement of ionic conductivity in novel LiON-AlO_x multilayer heterostructures prepared by atomic layer deposition, Solid State Ionics, 373 (2021) 115796.

2. Guiying Tian, Yuanyuan Song, **Xianlin Luo**, Zijian Zhao, Fanfan Han, Jiali Chen, Huaming Huang, Na Tang, Sonia Dsoke, ZnS nanoparticles embedded in N-doped porous carbon xerogel as electrode materials for sodium-ion batteries, Journal of Alloys and Compounds, 877 (2021) 160299.

3. Guiying Tian, Yuanyuan Song, **Xianlin Luo**, Zijian Zhao, Fanfan Han, Jiali Chen, Huaming Huang, Na Tang, Sonia Dsoke, Lithium storage mechanism study of N-doped carbon modified Cu_2S electrodes for lithium-ion batteries, Chemistry-A European Journal, 27 (2021) 13774-13782.

4. Qiang Fu, Xiaoyu Wu, **Xianlin Luo**, Sylvio Indris, Angelina Sarapulova, Marina Bauer, Zhengqi Wang, Michael Knapp, Helmut Ehrenberg, Yingjin Wei, Sonia Dsoke, High-voltage aqueous Mg-ion batteries enabled by solvation structure reorganization, Advanced Functional Materials, (2022) 2110674

5. Marina Bauer, Kristina Pfeifer, **Xianlin Luo**, Hannes Radinger, Helmut Ehrenberg, Frieder Scheiba, Functionalisation of graphite electrodes with aryl diazonium salts for lithium-ion batteries, ChemElectroChem, (2022) e202101434.

6. Kristina Pfeifer, Stefanie Arnold, Öznil Budak, **Xianlin Luo**, Volker Presser, Helmut Ehrenberg and, Sonia Dsoke, Choosing the right carbon additive is of vital importance for high-performance Sb-based Na-ion batteries, Journal of Materials Chemistry A, 8 (2020) 6092-6104.

7. Kristina Pfeifer, Miryam Fayena Greenstein, Doron Aurbach, **Xianlin Luo**, Helmut Ehrenberg, and Sonia Dsoke, Interaction between electrolytes and Sb_2O_3-based electrodes in sodium

batteries: uncovering the detrimental effects of diglyme, ChemElectroChem 7 (2020) 3487–3495.

8. Chengping Li, Angelina Sarapulova, Kristina Pfeifer, **Xianlin Luo**, Nicola Pietro Maria Casati, Edmund Welter, Georgian Melinte, Qiang Fu, and Sonia Dsoke, Elucidating the mechanism of Li insertion into $Fe_{1-x}S$/Carbon via in operando synchrotron studies, ACS Applied Materials & Interfaces, 12 (2020) 52691-52700.

9. Qiang Fu, Jiaqi Wang, Angelina Sarapulova, Lihua Zhu, Alexander Missyul, Edmund Welter, **Xianlin Luo**, Ziming Ding, Michael Knapp, Helmut Ehrenberg, Sonia Dsoke, Electrochemical performance and reaction mechanism investigation of orthorhombic V_2O_5 as positive electrode material for aqueous rechargeable zinc batteries, Journal of Materials Chemistry A, 9 (2021) 16776-16786

10. Qiang Fu, Angelina Sarapulova, Lihua Zhu, Georgian Melinte, Alexander Missyul, Edmund Welter, **Xianlin Luo**, Michael Knapp, Helmut Ehrenberg, Sonia Dsoke, In *operando* study of orthorhombic V_2O_5 as positive electrode materials for K-ion batteries, Journal of Energy Chemistry, 62 (2021) 627-636.

Acknowledgments

Firstly, I would like to thank Prof. Dr. Helmut Ehrenberg for having accepted me as a PhD candidate in the Institute of Applied Materials-Energy Storage Systems (IAM-ESS). Many thanks for his valuable advice, encouragement, support during my PhD, especially during the Corona period. I would like to acknowledge Prof. Dr. Michael J. Hoffmann for agreeing to be the first referee of this work. I would like also to thank Deutsche Forschungsgemeinschaft (DFG) for funding the project (EH183/19-1).

I would like to express my sincere thanks to my co-supervisor Dr. Sylvio Indris, who always supported me and gave me thoughtful suggestions. You encouraged me to do any scientific attempt and you were always enthusiastic to discuss anything with me. I would also like to thank my project collaborator, Dr. Andy Fiedler, for his support in Shanghai and helpful ideas.

My deep gratitude also goes to my office roommate Dr. Raheleh Azmi, who helped me practice XPS and performed ToF-SIMS measurements. I greatly appreciate the support from Dr. Michael Bruns, Vanessa Trouillet, Dr. Christian Njel, Dr. Julia Maibach for XPS discussions. I would also like to thank Udo Geckle for carrying out SEM measurements and technical support.

I would like to acknowledge Dr. Qiang Fu for the analysis of XRD results and correction of this PhD thesis. I would also like to thank Dr. Christina Pfeifer for carefully correcting this PhD thesis. Many thanks also go to Dr. Theato-Liu Xinyang and Tianzhu Liu for SEM measurements, to Dr. Anna-Lena Hansen for PDF measurements, to Dr. Holger Geßwein for GIXRD measurements, to Richard Thelen for WLI measurements, to Dr. Darma Mariyam Susana Dewi Darma for HTXRD, and to Tatiana Zinkevich for NMR measurements. I would also express my gratitude to Liuda Mereacre for her help in the lab, to my research assistant Mingze Yan for sample preparation, to Heinz-Robert Goebel and Luis Martin Sanchez Neudeck for equipment support, and to Dr. Heike Stöffler and Dr. Ruth Schlenker for teaching me cell assembly.

I am also grateful to Dr. Chengling Li, Marina Bauer, Dr. Jiangong Zhu, Dr. Weibo Hua, Dr. Guiying Tian, Dr. Lihua Zhu, Dr. Heike Stöffler, Dr. Charlotte Alina Fritsch, Ahmad Ghamlouche, Jessica Pfisterer, Georg-Maximilian Bosch, Hang Li for their support and kind help.

I would like to give a special thank you to my girlfriend Qinghe Hao, and my friends Dr. Jie Cao, Kan Li for their unfailing encouragement and tireless support.

Finally, I want to express my deep gratitude to my parents, my brothers, and my sister for the love and substantial support in my life.

Karlsruhe, 28.05.2021 *Xianlin Luo*